Università degli Studi di Palermo

AREA QUALITÀ, PROGRAMMAZIONE E SUPPORTO STRATEGICO
SETTORE STRATEGIA PER LA RICERCA
U. O. DOTTORATI

Civil, Environmental, and Materials Engineering
Department of Engineering
ING-IND/04 Costruzioni e Strutture Aerospaziali

A COMPUTATIONAL FRAMEWORK FOR AEROELASTIC TAILORING BASED ON THE USE OF CUF AND HIGH-FIDELITY CFD

IL DOTTORE
MARCO GRIFÒ

IL COORDINATORE
PROF.SSA ANTONINA PIRROTTA

IL TUTOR
PROF. IVANO BENEDETTI

CO TUTOR
PROF. ALBERTO MILAZZO

CICLO XXXV
ANNO CONSEGUIMENTO TITOLO 2023

Contents

List of Symbols and Abbreviations

$\hat{}$ ..... structural domain
$\check{}$ ..... aerodynamic domain
$\mathbf{bold}$ ..... vector
∞ ..... referring to freestream
$\intercal$ ..... transpose
∂ ..... partial derivative
$\sin$ ..... sine
$\cos$ ..... cosine
$\tan$ ..... tangent
div ..... divergent operator
grad ..... gradient operator
Tr ..... trace
α, β ..... indexes for 1,2,3
γ ..... $x_1 - x_2$ plane's Euler angle
$\gamma_{\hat{x}_\alpha, \hat{x}_\beta}$ ..... shear deformation
Γ ..... vortex circulation
Γ_d ..... dissipation coefficient
$\hat{\Gamma}$ ..... boundary of reference plate in Discontinuous Galerkin dissertation
δ ..... infinitesimal/virtual
Δs ..... first spatial 3D mesh extension
Δ_{DG} ..... flux variable in Discontinuous Galerkin dissertation
$\Delta\bar{\varepsilon}$ ..... tip twist angle
ϵ ..... generic order for $\mathbb{R}$
$\varepsilon_{\mathbf{t}}$ ..... tolerance for staggered iterative process
ε ..... strain
ζ ..... $x_1 - x_3$ plane's Euler angle
η ..... FE local coordinate
θ_c ..... tangent to camber line
λ ..... construction angle for Vortex Lattice Method

λ_v . . . . . second viscous proportionality constant
Λ . . . . . sweep angle
μ_v . . . . . dynamic viscosity
ν_v . . . . . kinematic viscosity
ξ . . . . . FE local coordinate
Ξ . . . . . tensor transformation matrix
ρ . . . . . density
σ . . . . . stress
Σ . . . . . equivalent surface
$\bar{\Sigma}$ . . . . . trace for interface conservativeness
τ . . . . . tangential stress
$\tau_{b,t}^{(\ell)}$ . . . . . bottom or top bound for a single ℓ lamina in a composite laminate
Υ . . . . . support in Moving Least Square technique interpolation
ϕ . . . . . potential variable
ϕ' . . . . . time-average of potential's fluctuation component
ϕ_{MLS} . . . . . weight functions for Moving Least Squares patch technique
Φ . . . . . time-average of potential
Φ_d . . . . . dihedral angle
ψ . . . . . $x_2 - x_3$ plane's Euler angle
ω . . . . . rate of dissipation
Ω . . . . . volume or space
A_d . . . . . section area considered for 1D diffusion problem
$\mathbf{A}_{m,n}$ . . . . . Aerodynamic Influence Coefficient
$\mathbf{AIC}$ . . . . . Aerodynamic Influence Coefficient matrix
AOA . . . . . angle-of-attack
AOA_a . . . . . absolute angle-of-attack
AOA_g . . . . . geometrical angle-of-attack
AOA_{ZL} . . . . . zero-lift angle-of-attack
a . . . . . side of a plate
aft . . . . . after
app . . . . . application
a_{FVM} . . . . . Finite Volume Method coefficient
b . . . . . span
$\boldsymbol{b}_v$ . . . . . volume force
B . . . . . strain-displacement function
c . . . . . chord
$\mathbf{C}$ . . . . . material stiffness matrix

C^d . . . . . generic subspace for Moving Least Squares technique dissertation
C_f . . . . . friction coefficient
CFD . . . . . Computational Fluid Dynamics
CPT . . . . . Classical Plate Theory
$crit$ . . . . . critical
CSCL . . . . . Constant Stifness Composite Laminate
CUF . . . . . Carrera Unified Formulation
D . . . . . derivative operator
DG . . . . . Discontinuous Galerkin
d_f . . . . . farfield diameter
e . . . . . elemental
E . . . . . energy
EPM . . . . . Equivalent Plate Modelling
eq . . . . . equivalent
ESL . . . . . Equivalent Single Layer
f_α . . . . . CUF function of the α order
f_{MLS} . . . . . generic function for Moving Least Square technique dissertation
$\bar{f}_{MLS}$ . . . . . local approximation for f_{MLS}
f . . . . . vector of elemental external forces
F . . . . . CUF function matrix
$\tilde{\mathbf{F}}$ . . . . . $\hat{x}_3$-direction stiffness integral
$\check{\mathbf{F}}$ . . . . . fluid pressure and stiffness loadings
$\mathbb{F}$ . . . . . function to minimize in Moving Least Square technique dissertation
FEM . . . . . Finite Element Method
$forw$ . . . . . forward
FGMRES . . . . . Flexible Generalized Minimal Residual
FVM . . . . . Finite Volume Method
g . . . . . generic function
$\tilde{\mathbf{G}}$ . . . . . $\hat{x}_3$-direction mass integral
GUF . . . . . Generalized Unified Formulation
HSDT . . . . . Higher Order Shear Deformation Theory
i . . . . . index for discretisation nodes (structural or aerodynamic)
i^*_X . . . . . index for set X in Moving Least Square technique dissertation
i^*_Y . . . . . index for set Y in Moving Least Square technique dissertation
i_{BF} . . . . . index for basis functions for f_{MLS} approximation
i_e . . . . . internal energy
I . . . . . used for various zeros and ones position matrixes

U . . . . . mean value of $\check{x}_1$ velocity
U_∞ . . . . . freestream velocity
$\mathbf{U}$ . . . . . generalized displacement vector
u_τ . . . . . friction velocity
$\bar{u}_{\hat{x}_3}$ . . . . . tip average displacement
V . . . . . mean value of $\check{x}_2$ velocity
$\mathbb{V}$ . . . . . control volume
VAT . . . . . Variable Angle Tow
VLM . . . . . Vortex Lattice Method
W . . . . . mean value of $\check{x}_3$ velocity
w_M . . . . . velocity's normal component
w_n . . . . . Gauss weight
X . . . . . set of staggered points for MLS dissertation
XX . . . . . percentage of chord for maximum thickness
$\mathbf{x}_{i_X^*}$ . . . . . coordinates from set X in MLS dissertation
y . . . . . distance from wall
Y . . . . . alternative set of staggered points for MLS dissertation
$\mathbf{y}_{i_Y^*}$ . . . . . coordinates from set Y in MLS dissertation
y^+ . . . . . boundary layer factor
Z . . . . . shape function in aerodynamic discretisation

List of Figures

List of Tables

Chapter 1

Introduction and state of art

In this Chapter the motivation and general considerations about the importance of aeroelastic analysis for aeronautical and aerospace applications are discussed. Subsequently, a short review of the state of art on the most popular methods for aeroelastic analysis is given.

1.1 Aeroelasticity: definitions

Aeroelasticity is one of the most crucial disciplines in the design of an airship or of single aircraft components. As the name suggests, it consists of the combination of structural elastic analysis, aerodynamic analysis and fluid-solid interaction. Wing, tails, fuselage and other components, subject to the action of a fluid in motion, need to be analyzed and sized according to the kind of mission the aircraft must perform; thus previsional flexible computational tools to detect displacements, strains and stresses of the structure are required. In Fig.1.1 the "aeroelastic triangle" groups the three aspects of aeroelasticity together.

Aeroelasticity is composed by two main typologies of analysis: static analysis, which studies the static deformation of a component because of the application of a steady-state freestream; and dynamic analysis, that involves inertial forces. For example, dynamic analysis could observe the mutual influence between the forced vibrations of a structure and the time-dependant changing loads coming from the non-stationary stream of a fluid.

In the static analysis the critical condition for the design is the *aeroelastic divergence*. It is a catastrophic phenomenon that takes place when the deformed structure is not able to balance the fluid-generated loads, and the displacement becomes ideally infinite (with a consequent failure of the structure). In the dynamic regime, one of the typical critical condition is *flutter*. It consists of the increase of forced vibra-

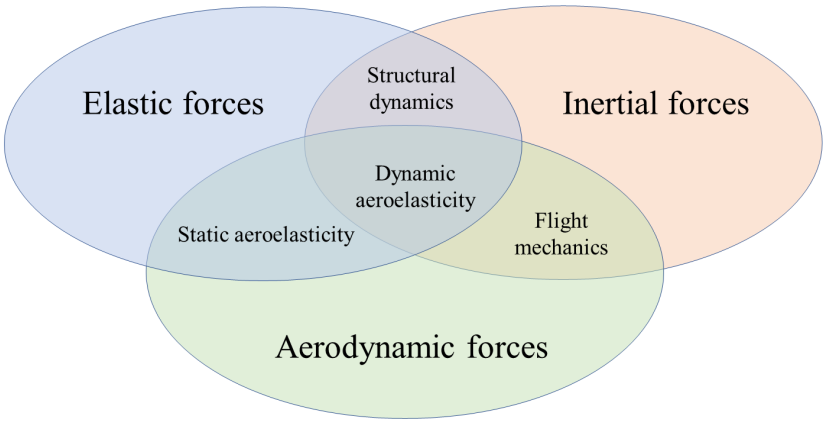

Figure 1.1: Aeroelastic triangle (see Ref.[1]).

tions in the structure because of the interaction among fluid loads, elastic loads and inertial loads. Static and dynamic phenomena could take place in different kinds of engineering applications, such as bridges, chimneys and urban slender furniture, based on the presence of a freestream.

1.2 Static aeroelasticity: general approaches

Although divergence, flutter and other critical conditions need to be identified for design, it is relevant as well an outlook of the possible deformed configuration (for example, of a wing) [2], to keep the air vehicle within the designed flight envelope. This work is devoted to the static aeroelastic analysis of aerospace structures to determine the new deformed fluid-structurally balanced configurations, even though the presented computational tool could be adapted to other different applications too, thanks to the versatility of the interface strategy.

Classical aeroelastic analysis, as shown for example in Refs. [3]-[4], and as it will be explained later, starts from basic notions of structural theory (equilibrium equations, energy equations) to obtain a compact formulation that derives loads from the aerodynamic outputs. Static aeroelastic analysis provides the deformation of a structure caused by a steady flow, without taking into account inertial terms or acceleration as well. The examples of static aeroelastic analysis presented in Hodges [3] consider simplified one-dimensional wings to obtain the governing aeroelastic equations (with ”strip theory” managing the influence of the deforming lifting surface) and, thus, the *divergence* condition that brings the structure to fail-

ure. This approach is still relevant for various different application, and it is adopted in preliminary design for the calculation of aerodynamic forces in an aeroelastic framework: in Ref.[5] aerodynamic influence coefficients are obtained through strip theory for supersonic wings; "modified strip theory" is employed for flapping wings [6] as well as for the analysis of wind turbine blades in Ref.[7]. This is a basic strategy to connect span-dependant aerodynamic variables with span-dependant structural outcomes, developing a single partial differential equation to manage coupling of bending and torsion in a beam model subject to an aerodynamic load.

Many other structural and aerodynamic strategies have been employed to face the complexity of this issue, mainly with low-fidelity aerodynamics. Ritz-based [8] structural equations for nonlinear configurations with plate models have been taken into account [9]; in Ref.[10] a meshless method has been used to manage simulations of aircraft with large control structural deflections; both Vortex Lattice Method (VLM) and Doublet lattice Method (DLM) have been coupled with Finite Element Method ([11], [12]); Rayleigh-Ritz structural method has been adapted to the coupling with piston theory [13]; VLM and FEM are again coupled in Ref.[14] to perform a review of the most influent factors in an aeroelastic optimization process.
However, a more detailed aeroelastic analysis requires to step into the domain of computational aeroelasticity, to recover more information from the fluid-structure interaction phenomena.

In fact, computational aeroelasticity [15] extends these concepts to multiple degrees of freedom problems, rewriting classical structural solution techniques (Ritz Method, Finite Element Method) to consider the fluid-dynamic nature of the loads. A fundamental evolution in aeroelastic strategies is the adoption of Computational Fluid Dynamics [16], that employs various bi- or tri-dimensional method to solve the fluid governing equations (for example the Finite Volume Method as in Ref.[17] for Navier-Stokes equations). Some concise reviews about computational aeroelasticity and coupling methods for CFD aeroelasticity are shown in Refs.[18]-[19]: in these references some possible future developments of the present research are noteworthy, such as Reduced Order Modeling approach (employed for aeroelastic analysis purposes in Ref.[20]) to allievate the computational burden.

1.3 Fluid-structure interactions strategies

The need for a full coupling of structural analysis and fluid analysis can be easily understood observing for example the nature of lift generation in a wing structure.

The circulation of the airstream generates a different level of pressure between upside and lowside of the wing, with a strength that changes with the geometry of the chosen airfoil. The structure deforms accordingly, but this provides a change in the geometry met by the airstream; thus, aerodynamic loadings change, and the deformation of the structure with them, until a balance is met. The nature of this balance could be considered stable between certain boundaries: a change from the regime condition in the geometric or aerodynamic configuration (deflection of high-lift devices or variation in angle of attack or freestream velocity) provides a variation of the trim in a new stable distribution of elements. This phenomenon takes place in any static aeroelastic analysis, and it will be essential for the understanding of the computational tool developped in this work. Thus, it is intuitive to understand that the loads required for the classical *divergence* failure are not the ones identifiable from a simple static structural analysis. The interaction of the fluid with the structure induces a decrease in the structural stiffness, so that the aforementioned failure happens at notably lower loads.

The interaction between two heterogeneous domains such as the structural one (i.e. a structural mesh, compatible with the chosen structural hypothesis; or a meshless region studied through polynomial interpolation) and the aerodynamic one (i.e. the aerodynamic mesh or panelization or vortices/doublets distribution) is regulated by many different techniques. Two important families of interpolation strategies are Spline Methods (i.e. Infinite Spline Method [21]) and Moving-Least Square technique [22], even though different numerical methods are applied in different conditions according to the dimensions and the kinds of discretization that are involved (see a review in Ref.[23]). The Infinite Spline Method employs partial differential equation of an infinite plate, so to find a surface which crosses the new solutions and contains the new points on which the solutions want to be found. A discussion of this technique can be found in Ref.[24]. Moving Least-Square technique has a similar objective, but it appeals to the manipulation of weight functions and minimization of errors to obtain a final matrix. A treatment of this method can be found in Ref.[25]. It needs to be stressed that the Moving-Least Square (MLS) patches technique [22] allows a flexible coupling taking off from the definition of conservation of momentum and energy, according to the Principle of Virtual Work.

Fluid-structure interaction analysis deals with the aeroelastic problem according to the chosen structural/aerodynamic methods: Infinite Spline has been used in Ref.[26] to couple finite element method (and it has been revisited with the Carrera Unified Formulation [27]) and Vortex Lattice Method, so to embody the aerodynamic loadings to the FEM discretised static equation. This compact representation

allows an eigenvalue approach for the resolution of the divergence problem, and it will be addressed in this work as the ”monolithic” approach. Nevertheless, the use of CFD coupled with a structural analysis requires another kind of coupling, combining two distinct computational environments, one for the structural analysis and one for the aerodynamic analysis. In static regime, this heterogeneous approach implies a staggered iterative approach, thus in this work this alternative will be addressed as ”staggered iterative” to avoid any misunderstanding. Sometimes this alternative in literature is called ”partitioned” [22], so this definition will be used as a synonim to ”staggered iterative”. In a dynamic aeroelasticity framework, three possible different definitions can be given, according to the ones exposed in Ref.[28]: fully-coupled approach, loosely-coupled approach and closely-coupled approach. This last differentiation mainly deals with the order of computation of the two domains with respect to a time step. However, dynamic aeroelasticity is not the investigated object for this research and for further information the reader is referred to Refs.[29]-[30], even though it can be said that the static staggered method chosen here and presented in this work can be extended to dynamic analysis in future development as a loosely-coupled aeroelastic approach, as in Ref.[31]. The choice of a staggered iterative approach for static aeroelasticity is due to the perspective to extend this approach to different kinds of multi-field problems, such as hydro-dynamics problems [32], in future developments. That would be mainly possible because of the inherently heterogeneous nature of the presented framework.

1.4 The Finite Element Method: composite materials and structural models

Composite materials are mostly used in this field. They offer great performances in terms of strength and stiffness with respect to relatively low weights. Modelization of their discrete properties allows to perform an optimization of their configuration according to the application. This process is named Aeroelastic Tailoring and a preliminary example of this will be provided in this work.

The structural methods adopted in this work intend to model composite materials in a flexible and accurate way. Composite materials are extensively employed in aeronautical engineering [33], and their principal properties such as high strength-to-weight ratios and stiffness-to-weight ratios are the main attractions for structural design of aerostructures. In Ref.[34] the ways of modelling these kinds of materials are clearly exposed, in particular Classic Lamination Theory and micro and macro mechanical behaviors of laminas. Low costs of installation and modifiable specifics

for increasing performances in critical weather and chemical conditions [35] are fundamental too in aeronautics, but they will not be object of this work.

An important distinction in modelling composite structures is about Equivalent Single Layer (ESL) [36] and Layer-Wise (LW) [37] approaches. They differ for the consideration of the single layers of the lamina: in this work the ESL approach is adopted, mainly because of the kinds of mechanical phenomena involved in static aeroelastic applications and because of the adoption of thin plates and shells. It consists of modelling the corresponding structural terms adding up the contribution of every layer. For example, in computing the stiffness matrix for Finite Element Method, the element stiffness matrix is calculated summing up all the different stiffness properties coming from each layer [38]. In aeroelastic analyses from Ref.[27] Equivalent Single Layers are adopted - and Layer-Wise approaches are taken into account just to detect composite local effects which are not analysed in this work.

In the aeroelastic studies of wings presented in literature, beam models [39] and plate models [40] are the most employed for composite structures, and mainly the beam models are used because of the relatively easier computation of a monodimensional structural model. However in several application the beam model requires the refinement of the interpolation functions in the structural method and to discretize the section to operate a Gauss quadrature for the integration. This aspect makes the plate model at least competitive in terms of degrees of freedom. Both in beams and plates, in fact, the discretization of the structure through Finite Element Method [41] leads to the choice of a kinematic assumption, an interpolation order and a distribution of elements. The last two terms respectively take the name of p-refinement and h-refinement, and have a main role in the final numbers of degrees of freedom (DOFs). The functional matrices of FEM (stiffness, mass, damping) have a size strictly connected to the number of DOFs.

1.5 The Carrera Unified Formulation and Equivalent Plate Modelling

Finite Element Method (FEM) [41] is still nowadays one of the most competitive methods for several kinds of analysis. Its use in this work is mainly due to the inner simplicity of the combination process of FEM with the other two important subjects of this structural dissertation: the Carrera Unified Formulation and the Equivalent Plate Modelling [42]. The Carrera Unified Formulation (CUF) [43] is a compact strategy to establish the type of kinematic assumption to be employed in the analysis. From a computational point of view, it allows to define the order

of the structural model and the equation type (Taylor-like expansions or Lagrange polynomials) as input parameters to consequently modify the kinematic hypothesis. If a system $(\hat{x}_1, \hat{x}_2, \hat{x}_3)$ is defined, in 1D models the CUF-functions are the cross-section-functions $F(\hat{x}_1, \hat{x}_3)$, considering $\hat{x}_1$ in the direction of the span and defining the section plane along with $\hat{x}_3$; instead, the through-thickness functions $F(\hat{x}_3)$ are the one adopted for 2D models. An increase in the CUF order corresponds to an increase in the desired accuracy (that can be due, for example, to a complex geometry).

CUF provides generality for the selection of the order of the analysis, and EPM simply determines the integration intervals to which FEM is subject: they are then coupled with the FEM method, from the variational statement of the application of the Principle of Virtual Displacements to the employment of shape functions. Various examples in the use of CUF+FEM can be found in literature, both in 2D [44] and 1D [45] hypothesis. The model employed in this work is fully three-dimensional, involving integrals in the three directions; however, the governing equations are 2D plate equations, and the integration over the thickness is performed in an exact form with the accuracy required for the chosen CUF2D order.

The most simple law for CUF formulation is given by Taylor-like expansion, but many other expansions can be used. It is nowadays employed in many different contexts, from Structural Health Monitoring [46] to piezoelectric materials modelling [47].

Equivalent Plate Modelling (EPM) [48] consists of analyzing any three-dimensional structure as a projected plane, in which every mechanical property is concentrated. Even if the contribution of the distributed material along the thickness of the equivalent plate is obtained through a simple summation, EPM is able to recover three-dimensional behaviors such as bending-torsion coupling if addressed with an opportune structural model. An exhaustive review of EPM is presented in Ref.[49], from the combinations with Ritz techniques [50] to the wider aeroelastic applications such as Ref.[51]. More rarely, EPM has been coupled with Finite Element Method [52].

Both CUF 1D and 2D models reconstruct a complete three-dimensional behavior through the resolution of 1D and 2D governing equations respectively. However, 1D approach often requires the enrichment of the CUF cross-section functions $F(\hat{x}_1, \hat{x}_3)$ with advanced formulations such as Lagrange polynomials or hierarchical Legendre functions [53], along with a discretization and a subdivision of the cross section in subdomains. This step is overcome in 2D methods, which only require a simple straightforward *p*-refinement or *h*-refinement of the planar 2D mesh,

with the integration of the through-the-thickness function $F(\hat{x}_3)$ being managed just through Equivalent Plate Modelling.

Two-dimensional models are the main focus of this work. Through Equivalent Plate Modelling any kind of section can be considered, for example in the integration required by the building up of the FEM stiffness matrix.

1.6 Aerodynamic methods: from low-fidelity to high-fidelity strategies

In most of aeroelastic treatments in the literature, the Vortex Lattice Method (VLM) and Double Lattice Method (DLM) [54] are the chosen strategies for the resolution of the aerodynamic problem. These low fidelity aerodynamic approaches provide aerodynamic loads on a bidimensional scheme (panels or doublets, according to the method), and appropriate matrices to build a compact formulation with the classic FEM equation. Infinite Spline Method [21] is one of the possible adoptable approaches to create a compact formulation. The creation of a compact formulation is a fundamental step to be able to recover aeroelastic divergence conditions through resolution of the eigenvalue problem.

In this work, Computational Fluid Dynamics (CFD) is adopted to flexibly solve different kinds of static aeroelastic problems, involving subsonic, transonic and supersonic regimes. In fact, the greatest limitation of linearized approaches like VLM and DLM is the inability to recover accurate results for higher regimes: they neglect drag effects, unless they are kept into account through opportune corrections in their formulation. In particular, it will be seen that in VLM very low subsonic regimes that show an increase in the importance of the role of viscosity could also be a drawback in the theory. CFD, here employed through the open-source software `SU2` [55], represents a robust substitute to these low fidelity approaches to overcome the abovementioned limitations. However, an heterogeneous approach which combines a CUF+FEM+EPM code and `SU2` performances makes the creation of a compact strongly-coupled solving equation very difficult, because it would require the calculation of an "aerodynamic influent cofficient matrix" (AIC, typical of low-fidelity approaches), not very feasible in a three-dimensional CFD framework. Moreover, the CFD simulation could be very time-consuming, so it is necessary to consider that the use of this tool could be justified by complex applications.

`SU2` is the chosen program to address CFD problems. It is an open-source tool composed by `C++` routines, able to solve Reynolds-Averaged-Navier Stokes (RANS) equations in a discretized domain through Finite Volume Method (FVM).

With SU2 turbulence models equation can be solved too along with RANS, if the aerodynamic complexity of the problem requires it. Spalart-Allmaras [56] as well as $k-\varepsilon$ [57] or $k-\omega$ [58] models are available in the code.

Several different employments of SU2 can be found in the literature: applications with Reduced Order Modelling [59], coupling with structural software NASTRAN [60] and its use with wind turbines applications [61]. Of course, high CPU-time associated with high-fidelity aerodynamics represents a considerable drawback, considering that this kind of process is often applied within preliminary stages of aircraft design. However, in this work both low and high flow regimes with simple or complex structural configurations show the need for this high-fidelity approach, as it will be seen in subsequent chapters.

1.7 Preliminary Aeroelastic Tailoring

One of the applications of the methods developed here is a preliminary framework for the resolution of *Aeroelastic Tailoring* problems. Aeroelastic Tailoring [62] is one of the most attractive features offered by composite materials, from traditional Constant Stiffness Composite Laminates (CSCLs) to more recent Variable Angle Tow (VAT) materials. Their aim is to concentrate strength and specific properties in predetermined directions where they are required (such as bending strength in bending dominant regions or traction strength in traction dominant ones). A state of art of aeroelastic tailoring strategies is shown in [63]. In this work a preliminary form of Aeroelastic Tailoring will be performed on complex realistic wing configurations, showing the flexibility of the presented framework CUF2D+FEM+EPM+SU2 which is not present in updated literature apart from the Author contributions.

1.8 Objectives and novelties of the work and organization of the work

The aim of this work is the development of a new high-fidelity and flexible computational framework able to handle general aeroelastic problems arising from the consideration of either complex aerodynamic conditions or structural configurations or both. The complexity of the aerodynamic problem can be related to the need of considering compressibility or viscosity effects, which generally call for the employment of higher-order aerodynamic theories or even Computational Fluids Dynamics. On the other hand, typical structures employed in aeronautics and

aerospace applications generally entail the presence of thin shells, made of either aluminum or of multilayered fiber reinforced composites, stiffened by other structural elements whose presence must be accounted for reliable analysis and design; under the action of the aerodynamic loads, such complex structures generally experience coupled bending-torsion deformation modes that in turns induce, due to the fluid-structure interaction, aerodynamic loads redistribution. The generality of possible structural configurations and aerodynamic regimes of interest would considerably benefit from the availability of tunable variable order computational tools, whose development is precisely the goal of the work presented here.

As mentioned, aeroelastic analyses are a fundamental step in the design of aerospace components since the preliminary stages and sketches. Together with flight mechanics, controls and aerodynamic optimization, structural sizing is of course central, because it influences all the other design sectors. The choice of material is a peculiar aspect of the preliminary design stages, and a schematic modelization of the component in these stages is useful to foresee the overall behavior of the component in terms of elastic characterization. Thus, the further wing aeroelastic analysis needs to be considered as part of these initial considerations regarding an aerospace design.

In this work an advanced coupling approach CUF2D+FEM+EPM+CFD is proposed for static aeroelastic analysis. The structure can be subject to any different aerodynamic regime, according to the ability of `SU2` to solve Euler or Navier-Stokes equations enriched by turbulence models such as Spalart-Allmaras and $k-\omega$. Any different aerodynamic regime does not change the organization of the structural code or the one of the interface functions, thanks to the heterogeneity of the coupling.

The work is divided in 6 chapters, including this Introduction: in Chapter 2 (Structural Modelling) the mechanical strategies applied in this work are explored; in Chapter 3 (Aerodynamic Modelling) the main aerodynamic issues are addressed, considering different formulations of low-fidelity and high-fidelity aerodynamics and computational strategies; in Chapter 4 (Fluid-Structure Interaction and Coupling) the theory about the interaction between fluid and structure is addressed; in Chapter 5 (Validation and Experiments) a series of test cases are described to show the flexibility and robustness of the proposed model (some of these results have already been published in Ref.[64]); in Chapter 6 (Conclusions and Futher Developments) general conclusions and future developments are addressed.

Chapter 2

Structural Modelling

The aim of this Chapter is the presentation of the combination CUF2D+FEM+EPM as a structural strategy for wing aeroelastic analysis, as a substitute to the beam method employed in Ref.[65]. In the reference aeroelastic beam model, FEM is solved through the discretization of the beam axis and the details of the section are reconstructed through further discretization of that plane and Gauss quadrature. In the present proposed strategy, FEM is solved on the 2D finite elements on the projected (equivalent) plate and the integrals over the thickness are exact and defined according to the distribution of the material.

In this Section, an overview on the present structural strategy is reported. The explanation of the combination of CUF+EPM+FEM is carefully described.

Specific attention will be given to the modelization of composite materials, which are crucial for the Aeroelastic Tailoring purposes. The theoretical background of this Chapter keeps into account the know-how in the use of composite laminates in aeroelastic analysis ([66],[67]), and will be explored altogether with the principal efforts needed for its translation to code. For this research, the theoretical aspects here exposed have been implemented through a Python code.

2.1 CUF formulation of the constitutive relation

Let us consider a generic three-dimensional (3D) structure described by the volume $\hat{\mathbf{\Omega}} \in \mathbb{R}^3$, and its boundary surface $\hat{\mathbf{\Sigma}} \in \mathbb{R}^2$, where the hat $\hat{}$ denotes the structural domain. It is defined with respect to a $O\left(\hat{x}_1, \hat{x}_2, \hat{x}_3\right)$ reference system and it can present any complexity within this boundary.

Following the Equivalent Plate Model methodology [48], a reference surface $\hat{\Sigma}_{eq} \in \mathbb{R}^2$ must be specified, and in this case it is the projection of the 3D structure over a $\hat{x}_1 - \hat{x}_2$ plane. Through a suitable projection the 1D boundary of this surface,

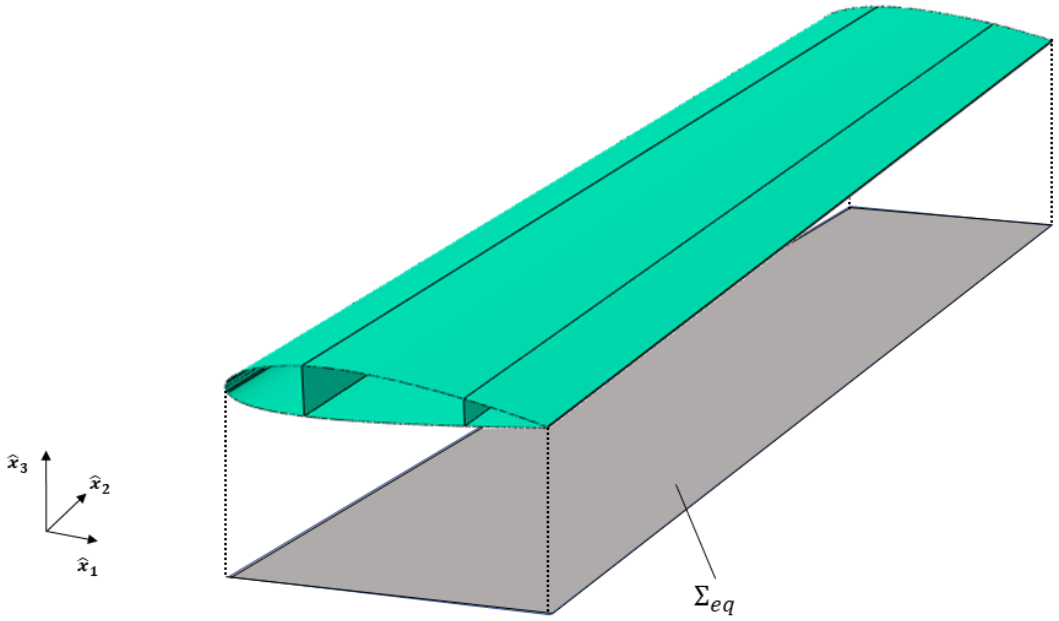

Figure 2.1: General scheme for Equivalent Plate Modelling.

$\hat{\Gamma}_{eq} \equiv \partial\hat{\Sigma}_{eq}$, can be obtained. $\hat{x}_3$ coordinate with respect to this plane is crucial for the kinematic assumption that will be elaborated by CUF, to define the geometrical distribution of the material along the thickness and thus the integration intervals for EPM. From now on, the EPM reference plane will be always considered as coincident with a plane containing the root chord of the wing and the wing span direction. Nevertheless, as shown in Fig.2.1, the plane could be located outside the volume of the structure: in this case, the reference system for the definition of the integral intervals will need an opportune translation.

Let us define u_i as the i-th displacement component at the generic point $\hat{\mathbf{x}} \equiv (\hat{x}_1, \hat{x}_2, \hat{x}_3) \in \hat{\Omega}$ expressed as

$$u_i\left(\hat{x}_1, \hat{x}_2, \hat{x}_3\right) = \sum_{\alpha=0}^{N_u} u_{i\alpha}\left(\hat{x}_1, \hat{x}_2\right) f_\alpha\left(\hat{x}_3\right) \qquad i = 1, 2, 3 \tag{2.1}$$

where $f_\alpha\left(\hat{x}_3\right)$ are *known* through-the-thickness function and $u_{i\alpha}\left(\hat{x}_1, \hat{x}_2\right)$ are *unknown* generalized displacement functions. $N_u + 1$ is the order of expansion preliminarily assumed for the kinematic hypothesis of the structural model, and it is the essential parameter to be taken into account in any computational consideration: in fact, the formulation can accomodate different kinematic assumptions for the mechanical analysis without any changing in the implementation. The order of the kinematic model constitutes one of the very first input of the implementation.

Higher order structural model can be obtained by suitably selecting the order of expansion.

In Eq.(2.1) a CUF2D is proposed; CUF1D would have presented through-the-section functions f_α dependant from both $\hat{x}_1, \hat{x}_3$ and generalized displacements dependant only from $\hat{x}_2$. For readibility purpose, the hat $\hat{}$ from displacements $\boldsymbol{u}$, generalized displacements $\boldsymbol{U}$, strains $\boldsymbol{\varepsilon}$, stresses $\boldsymbol{\sigma}$ and surface tractions $\boldsymbol{t}$ will be neglected unless necessary for disambiguation.

Eq.(2.1) may be rewritten in compact form as

$$\boldsymbol{u}\left(\hat{\mathbf{x}}\right) = \mathbf{F}\left(\hat{x}_3\right)\boldsymbol{U}\left(\hat{x}_1, \hat{x}_2\right) \tag{2.2}$$

which is useful for computer implementation. $\mathbf{F}\left(\hat{x}_3\right)$ is a $3 \times \left(3N_u + 3\right)$ matrix, and it contains the through-the-thickness functions $f_{i\alpha}\left(\hat{x}_3\right)$ distributed as

$$\mathbf{F}\left(\hat{\mathbf{x}}_\mathbf{3}\right) = \begin{bmatrix} f_{\hat{x}_1 0} & 0 & 0 & f_{\hat{x}_1 1} & 0 & 0 & f_{\hat{x}_1 2} & 0 & 0 & \dots \\ 0 & f_{\hat{x}_2 0} & 0 & 0 & f_{\hat{x}_2 1} & 0 & 0 & f_{\hat{x}_2 2} & 0 & \dots \\ 0 & 0 & f_{\hat{x}_3 0} & 0 & 0 & f_{\hat{x}_3 1} & 0 & 0 & f_{\hat{x}_3 2} & \dots \end{bmatrix}$$
$$\begin{bmatrix} f_{\hat{x}_1 N_u} & 0 & 0 \\ 0 & f_{\hat{x}_2 N_u} & 0 \\ 0 & 0 & f_{\hat{x}_3 N_u} \end{bmatrix} \tag{2.3}$$

in which every $f_{i,\alpha}$ is dependant from $\hat{x}_3$. The collection disposition of the generalized displacements in the vector $\mathbf{U}\left(\hat{x}_1, \hat{x}_2\right)$ follows the structure of $\mathbf{F}$.

The strains and stresses are straightforwardly derived from Eq.(2.2), considering the small-strain assumption, the Voigt notation and keeping into account that the derivative operator $\mathcal{D}$ involves all the three directions, so requires the derivation of the terms inside $F\left(\hat{x}_3\right)$ as well:

$$\boldsymbol{\varepsilon} = \mathcal{D}\mathbf{F}\left(\hat{x}_3\right)\mathbf{U}\left(\hat{x}_3\right) = \mathbf{I}_\alpha \mathbf{F}\frac{\partial \boldsymbol{U}}{\partial \hat{x}_\alpha} + \mathbf{I}_3\frac{\mathrm{d}\,\mathbf{F}}{\mathrm{d}\hat{x}_3}\boldsymbol{U} \tag{2.4}$$

with $\alpha = 1, 2$ and $\mathbf{I}_\alpha$ defined as in [68] as:

$$\mathbf{I}_1 = \begin{bmatrix} 1 & 0 & 0 \\ 0 & 0 & 0 \\ 0 & 0 & 0 \\ 0 & 0 & 0 \\ 0 & 0 & 1 \\ 0 & 1 & 0 \end{bmatrix}, \mathbf{I}_2 = \begin{bmatrix} 0 & 0 & 0 \\ 0 & 1 & 0 \\ 0 & 0 & 0 \\ 0 & 0 & 1 \\ 0 & 0 & 0 \\ 1 & 0 & 0 \end{bmatrix}, \mathbf{I}_3 \begin{bmatrix} 0 & 0 & 0 \\ 0 & 0 & 0 \\ 0 & 0 & 1 \\ 0 & 1 & 0 \\ 1 & 0 & 0 \\ 0 & 0 & 0 \end{bmatrix} \tag{2.5}$$

Linear elastic material behavior is assumed:

$$\boldsymbol{\sigma} = \mathbf{C}\boldsymbol{\varepsilon} = \mathbf{C}\,\mathbf{I}_\alpha\mathbf{F}\frac{\partial \boldsymbol{U}}{\partial \hat{x}_\alpha} + \mathbf{C}\,\mathbf{I}_3\frac{\mathrm{d}\,\mathbf{F}}{\mathrm{d}\hat{x}_3}\boldsymbol{U}, \tag{2.6}$$

being $\mathbf{C}$ the 6×6 material stiffness matrix. In Eq.(2.6) the constitutive equation of any material is rewritten according to the CUF generalized concept of kinematic model.

2.2 Principle of Virtual Displacements

The Finite Element Method is formulated from the Principle of Virtual Displacements (PVD):

$$\int_{\hat{\Omega}} \delta\boldsymbol{\varepsilon}^\intercal\boldsymbol{\sigma}\,\mathrm{d}\Omega = \int_{\hat{\Sigma}} \delta\boldsymbol{u}^\intercal\boldsymbol{t}\,\mathrm{d}\Sigma \tag{2.7}$$

where the apex $^\intercal$ indicates the transpose of the vector and t is the vector containing the surface tractions. Volume forces are here neglected. Substituting Eqs.(2.1),(2.4) and (2.6) in Eq.(2.7), it is obtained:

$$\int_{\hat{\Omega}} \left(\frac{\partial \delta\boldsymbol{U}^\intercal}{\partial \hat{x}_\alpha}\mathbf{F}^\intercal\mathbf{C}_{\alpha\beta}\mathbf{F}\frac{\partial \boldsymbol{U}}{\partial \hat{x}_\beta} + \frac{\partial \delta\boldsymbol{U}^\intercal}{\partial \hat{x}_\alpha}\mathbf{F}^\intercal\mathbf{C}_{\alpha 3}\frac{\mathrm{d}\mathbf{F}}{\mathrm{d}\hat{x}_3}\boldsymbol{U} + \delta\boldsymbol{U}^\intercal\frac{\mathrm{d}\mathbf{F}^\intercal}{\mathrm{d}\hat{x}_3}\mathbf{C}_{3\alpha}\mathbf{F}\frac{\partial \boldsymbol{U}}{\partial \hat{x}_\alpha} + \delta\boldsymbol{U}^\intercal\frac{\mathrm{d}\mathbf{F}^\intercal}{\mathrm{d}\hat{x}_3}\mathbf{C}_{33}\frac{\mathrm{d}\mathbf{F}}{\mathrm{d}\hat{x}_3}\boldsymbol{U} \right) \mathrm{d}\Omega = \int_{\hat{\Sigma}} \delta\boldsymbol{U}^\intercal\mathbf{F}^\intercal\boldsymbol{t}\,\mathrm{d}\Sigma \tag{2.8}$$

PVD is rewritten in CUF form. α and β are defined between 1 and 2 and $C_{ij} = \mathbf{I}_i^\intercal\mathbf{C}\,\mathbf{I}_j$ with i,$j = 1, 2, 3$ implies summation over α and β. Not being $\mathbf{U}$ dependant from $\hat{x}_3$, Eq.(2.8) is rewritten as

$$\int_{\hat{\Omega}_{eq}} \left(\frac{\partial \delta\boldsymbol{U}^\intercal}{\partial \hat{x}_\alpha}\tilde{\mathbf{F}}_{\alpha\beta}\frac{\partial \boldsymbol{U}}{\partial \hat{x}_\beta} + \frac{\partial \delta\boldsymbol{U}^\intercal}{\partial \hat{x}_\alpha}\tilde{\mathbf{F}}'^\intercal_{3\alpha}\boldsymbol{U} + \delta\boldsymbol{U}^\intercal\tilde{\mathbf{F}}'_{3\alpha}\frac{\partial \boldsymbol{U}}{\partial \hat{x}_\alpha} + \delta\boldsymbol{U}^\intercal\tilde{\mathbf{F}}''_{33}\boldsymbol{U} \right) \mathrm{d}\Omega = \int_{\hat{\Sigma}} \delta\boldsymbol{U}^\intercal\mathbf{F}^\intercal\boldsymbol{t}\,\mathrm{d}\Sigma, \tag{2.9}$$

where

$$\tilde{\mathbf{F}}_{\alpha\beta} \equiv \int_{th} \mathbf{F}^{\intercal}\mathbf{C}_{ij}\mathbf{F}\,\mathrm{d}\hat{x}_3 \tag{2.10}$$

$$\tilde{\mathbf{F}}'_{3\alpha} \equiv \int_{th} \frac{\mathrm{d}\,\mathbf{F}^{\intercal}}{\mathrm{d}\hat{x}_3}\mathbf{C}_{3\alpha}\mathbf{F}\,\mathrm{d}\hat{x}_3 \tag{2.11}$$

$$\tilde{\mathbf{F}}''_{33} \equiv \int_{th} \frac{\mathrm{d}\,\mathbf{F}^{\intercal}}{\mathrm{d}\hat{x}_3}\mathbf{C}_{33}\frac{\mathrm{d}\,\mathbf{F}}{\mathrm{d}\hat{x}_3}\,\mathrm{d}\hat{x}_3 \tag{2.12}$$

It is worth noting that the integration domain has been changed from $\hat{\Omega}$ (3D) to $\hat{\Omega}_{eq}$ (2D) in Eq.(2.9), as the integrals in the $\hat{x}_3$ direction have been performed with respect to the equivalent plate. Through the application of the Gauss theorem the set of governing physical differential equations (PDEs) can be obtained directly on the same reference plate, as it has been performed in Ref.[69]. The terms defined in Eqs.(2.10)-(2.12) are integrals over the thickness and their value depends on the distribution of the material along the thickness. Thus, every element of the wing (skin, spars, ribs) is described on the $\hat{x}_3$ integral direction and determines the integral intervals. Following the EPM strategies, at the right-hand side of Eq.(2.9), $\hat{\Sigma}$ is the correct integration domain because surface forces are applied on the real 3D location of the surface, and not on the reference plate. In fact the $\mathbf{F}$ term on the right hand side is calculated keeping into account the real distribution of the material along the thickness, considering voids or any complex element within the volume.

2.3 Equivalent Plate Modelling

The integration along the thickness, which forms the core of EPM, deserves further clarification. Let us first consider a simple rectangle as a section of a volume studied with CUF2D+FEM+EPM and composed by an homogeneous material (as in Fig.2.2).

This section, defined on the plane $\hat{x}_1 - \hat{x}_3$, presents an overall thickness named th_{rect} and can be considered within Eqs.(2.10)-(2.11) as:

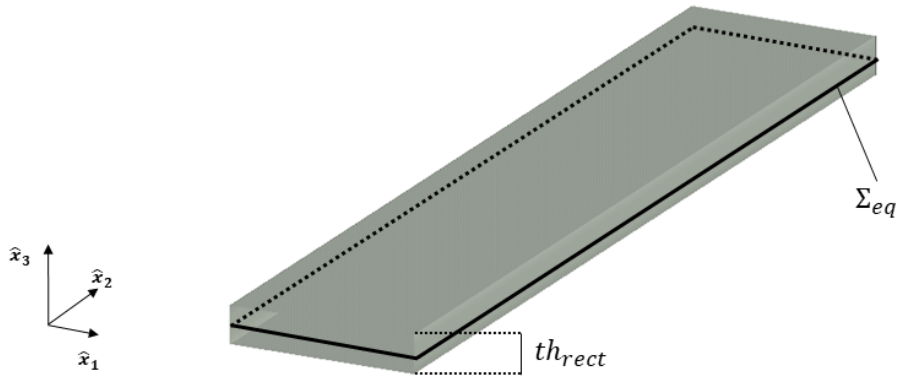

Figure 2.2: Rectangular wing for EPM scheme. The line underlines the reference plane.

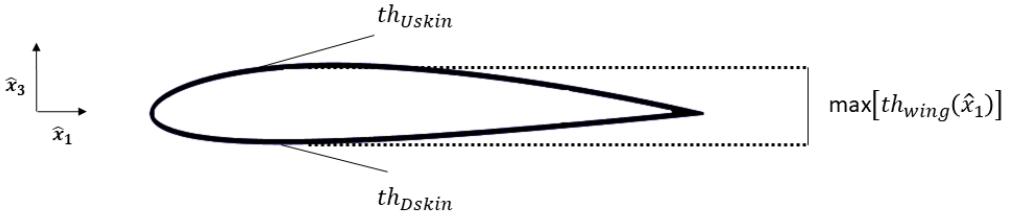

Figure 2.3: Airfoil NACA2415 for EPM scheme.

$$\tilde{\mathbf{F}}_{\alpha\beta} \equiv \int_{\hat{\tilde{x}}_3 - \frac{th_{rect}}{2}}^{\hat{\tilde{x}}_3 + \frac{th_{rect}}{2}} \mathbf{F}^{\intercal}\mathbf{C}_{ij}\mathbf{F}\,\mathrm{d}\hat{x}_3 \tag{2.13}$$

$$\tilde{\mathbf{F}}'_{3\alpha} \equiv \int_{\hat{\tilde{x}}_3 - \frac{th_{rect}}{2}}^{\hat{\tilde{x}}_3 + \frac{th_{rect}}{2}} \frac{\mathrm{d}\,\mathbf{F}^{\intercal}}{\mathrm{d}\hat{x}_3}\mathbf{C}_{3\alpha}\mathbf{F}\,\mathrm{d}\hat{x}_3 \tag{2.14}$$

$$\tilde{\mathbf{F}}''_{33} \equiv \int_{\hat{\tilde{x}}_3 - \frac{th_{rect}}{2}}^{\hat{\tilde{x}}_3 + \frac{th_{rect}}{2}} \frac{\mathrm{d}\,\mathbf{F}^{\intercal}}{\mathrm{d}\hat{x}_3}\mathbf{C}_{33}\frac{\mathrm{d}\,\mathbf{F}}{\mathrm{d}\hat{x}_3}\,\mathrm{d}\hat{x}_3 \tag{2.15}$$

if its symmetry plane $\hat{\tilde{x}}_3$ is the equivalent plane reference. If the thickness changes along the chord ($\hat{x}_1$), for example linearly, it is sufficient to keep it into account in th_{rect}, which becomes $th_{rect}\,(\hat{x}_1)$. This obvious passage is of crucial relevance in the construction of the structural code employed for the method, and must be kept into account during the cycling implementation loop over finite elements.

With the support of these example, let us consider the section of an isotropic wing without spars, with an airfoil NACA2415.

In this case the material is distributed over the two skins in the upper and lower side of the airfoil. The thickness law $th_{wing}\,(\hat{x}_1)$ is provided by the laws coming

from aerodynamic conventions, so in the 4-digits NACA number MPXX M stands for the percentage of chord determining the maximum camber; P for the percentage of chord defining the position of the maximum camber divided by 10; XX the percentage of chord defining the maximum thickness of the airfoil (see [70]). So in the NACA2415 case, 2% c is the maximum chamber, 40% c is the position of the maximum camber along the chord and 15% c is the maximum thickness of the airfoil. To represent such a behavior a $th_{wing}\left(\hat{x}_1\right)$ law needs to be opportunely derived.

A general law can be obtained from the camber relation $\hat{x}_{3c}\left(\hat{x}_1\right)$ and the thickness relation $\hat{x}_{3t}\left(\hat{x}_1\right)$. $\hat{x}_{3c}$ is split in $\hat{x}_{3c,forw}$ and $\hat{x}_{3c,aft}$ accordingly with the location of $\hat{x}_1$, forward or after the maximum ordinate of the camber line:

$$\hat{x}_{3c,forw} = \frac{\mathrm{M}}{\mathrm{P}^2}\left(2\mathrm{P}\hat{x}_1 - \hat{x}_1^2\right) \tag{2.16}$$

$$\hat{x}_{3c,aft} = \frac{\mathrm{M}}{(1-\mathrm{P})^2}\left((1-2\mathrm{P}) + 2\mathrm{P}\hat{x}_1 - \hat{x}_1^2\right) \tag{2.17}$$

The thickness law $\hat{x}_{3t}\left(\hat{x}_1\right)$ is instead

$$\hat{x}_{3th} = \frac{\mathrm{XX}}{0.2}\left(a_0\sqrt{\hat{x}_1} - a_1\hat{x}_1 - a_2\hat{x}_1^2 + a_3\hat{x}_1^3 - a_4\hat{x}_1^4\right) \tag{2.18}$$

with

$$a_0 = 0.2969, a_1 = 0.126, a_2 = 0.3516, a_3 = 0.2843, a_4 = -0.1036 \tag{2.19}$$

a_4 is relevant to distinguish sharp trailing edges or closed trailing edges. -0.1036 is referred to closed trailing edges and it is employed for all the cases studied in this Thesis. For sharp trailing edges a_4 would be equal to -0.1015.

Upside (U) and downside (D) $\hat{x}_{1,3}$ coordinates can be calculated through

$$\hat{x}_{1U} = \hat{x}_1 - \hat{x}_{3t}\sin\theta \tag{2.20}$$

$$\hat{x}_{3U} = \hat{x}_{3c} + \hat{x}_{3t}\cos\theta_c \tag{2.21}$$

$$\hat{x}_{1D} = \hat{x}_1 + \hat{x}_{3t}\sin\theta_c \tag{2.22}$$

$$\hat{x}_{3D} = \hat{x}_{3c} - \hat{x}_{3t}\cos\theta_c \tag{2.23}$$

where θ_c expresses the angle between $\hat{x}_1$ and $\hat{x}_3$ and is obtained:

$$\theta_c = \arctan\left(\frac{d\hat{x}_{3c}}{d\hat{x}_1}\right) \tag{2.24}$$

Similar processes are performed for different airfoils, such as NACA65A004 which is employed in Section 5.3.3. The basic airfoil theory for the construction of such geometries is analysed in Ref.[71].

Once the geometry distribution is defined, the exact integral intervals are selected accordingly. It must be stressed that the integrals are performed along $\hat{x}_3$ direction, so a projection of the skin thickness th_{skin} in that direction is needed. For the majority of $\left(\tilde{\hat{x}}_1, \tilde{\hat{x}}_2\right)$ discrete "stations" identified by the locations of the Gauss points in the finite element 2D mesh is sufficient to identify, as discussed in Ref.[42]:

$$th_{UD,skin} = th_{skin}\sqrt{1+\tan^2\theta_{UD}} \tag{2.25}$$

where θ_{UD} is the tangent angle to the airfoil skin in the up and down side, differently from θ_c because it corresponds to the derivative of Eqs.(2.21)-(2.23) and not only to the ones of the camber law $\hat{x}_{3c}\left(\hat{x}_1\right)$.

However, at some critical location, e.g. close to the leading edge or trailing edge elements, a more precise calculation of the integration bounds is required because discretized elements can also fall within the thickness. Eqs.(2.20)-(2.23) hold valid, and a simple switch in the coding is sufficient. This particular case can be seen for example in Fig.2.4 , where a zoom on the leading edge shows the situation of a thickness which involves a different selection for the integral bounds: not two thickness to be projected on the $\hat{x}_3$ direction, but one from the upper surface to the lower.

In Ref.[42] the right definitions of the integrals for the skin contribution are reported. Defining $th_{U,skin}$ and $th_{D,skin}$ as skin thicknesses in the up and down side of the airfoil respectively, Eqs.(2.13)-(2.15) can be re-elaborated as:

$$\tilde{\mathbf{F}}_{\alpha\beta} \equiv \int_{\hat{\tilde{x}}_3+\hat{\tilde{x}}_{3U}-\frac{th_{U,skin}}{2}}^{\hat{\tilde{x}}_3+\hat{\tilde{x}}_{3U}+\frac{th_{U,skin}}{2}} \mathbf{F}^\intercal\mathbf{C}_{ij}\mathbf{F}\,\mathrm{d}\hat{x}_3 + \int_{\hat{\tilde{x}}_3+\hat{\tilde{x}}_{3L}-\frac{th_{D,skin}}{2}}^{\hat{\tilde{x}}_3+\hat{\tilde{x}}_{3D}+\frac{th_{D,skin}}{2}} \mathbf{F}^\intercal\mathbf{C}_{ij}\mathbf{F}\,\mathrm{d}\hat{x}_3 \tag{2.26}$$

$$\tilde{\mathbf{F}}'_{3\alpha} \equiv \int_{\hat{\tilde{x}}_3+\hat{\tilde{x}}_{3U}-\frac{th_{U,skin}}{2}}^{\hat{\tilde{x}}_3+\hat{\tilde{x}}_{3U}+\frac{th_{U,skin}}{2}} \frac{\mathrm{d}\,\mathbf{F}^\intercal}{\mathrm{d}\hat{x}_3}\mathbf{C}_{3\alpha}\mathbf{F}\,\mathrm{d}\hat{x}_3 + \int_{\hat{\tilde{x}}_3+\hat{\tilde{x}}_{3D}-\frac{th_{D,skin}}{2}}^{\hat{\tilde{x}}_3+\hat{\tilde{x}}_{3D}+\frac{th_{D,skin}}{2}} \frac{\mathrm{d}\,\mathbf{F}^\intercal}{\mathrm{d}\hat{x}_3}\mathbf{C}_{3\alpha}\mathbf{F}\,\mathrm{d}\hat{x}_3 \tag{2.27}$$

$$\tilde{\mathbf{F}}''_{33} \equiv \int_{\hat{\tilde{x}}_3+\hat{\tilde{x}}_{3U}-\frac{th_{U,skin}}{2}}^{\hat{\tilde{x}}_3+\hat{\tilde{x}}_{3U}+\frac{th_{U,skin}}{2}} \frac{\mathrm{d}\,\mathbf{F}^\intercal}{\mathrm{d}\hat{x}_3}\mathbf{C}_{33}\frac{\mathrm{d}\,\mathbf{F}}{\mathrm{d}\hat{x}_3}\,\mathrm{d}\hat{x}_3 + \int_{\hat{\tilde{x}}_3+\hat{\tilde{x}}_{3D}-\frac{th_{D,skin}}{2}}^{\hat{\tilde{x}}_3+\hat{\tilde{x}}_{3D}+\frac{th_{D,skin}}{2}} \frac{\mathrm{d}\,\mathbf{F}^\intercal}{\mathrm{d}\hat{x}_3}\mathbf{C}_{33}\frac{\mathrm{d}\,\mathbf{F}}{\mathrm{d}\hat{x}_3}\,\mathrm{d}\hat{x}_3 \tag{2.28}$$

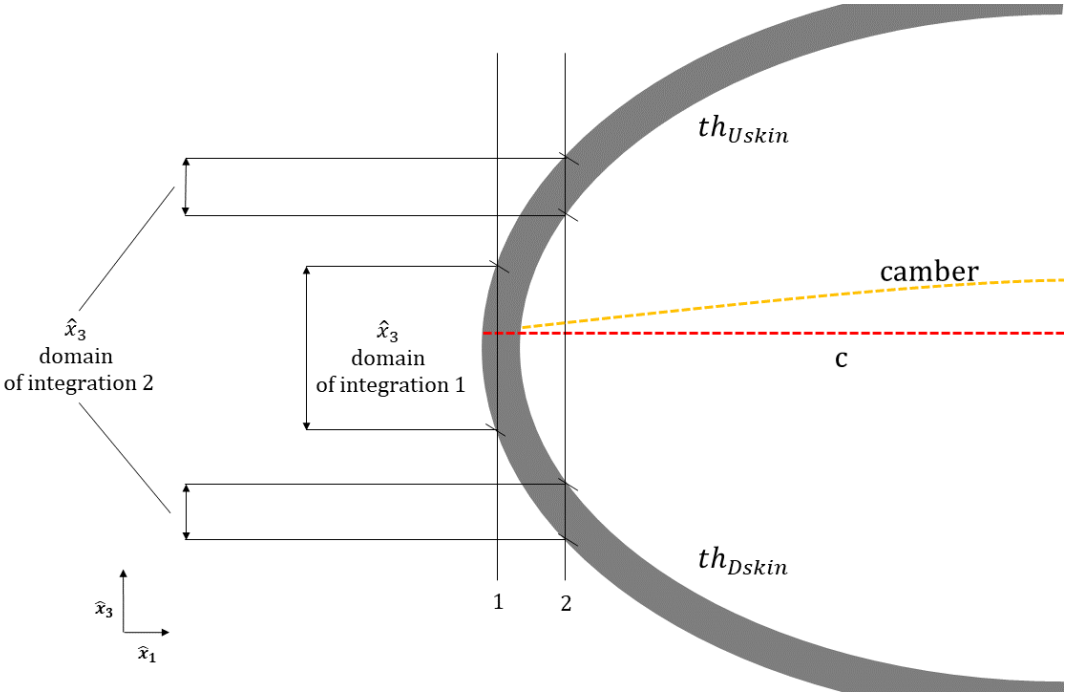

Figure 2.4: Detail of leading edge: 2 different integral intervals (one integral for case 1, two integrals for case 2).

In Eqs.(2.26)-(2.28) $\hat{\tilde{x}}_3$ is the reference coordinate for the equivalent plate, and $\hat{\tilde{x}}_{3U}$ and $\hat{\tilde{x}}_{3D}$ are considered with their own signs: in fact, according to the kind of airfoil $\hat{\tilde{x}}_{3U}$ can become negative going under the equivalent plate reference, and viceversa with $\hat{\tilde{x}}_{3D}$.

The presence of spars is addressed according to the following consideration. Let us consider Fig.2.5: the same airfoil as before (NACA2415) but with two spars and a rib.

Both of them present a web without cap. The contribution of internal element needs to be taken into account with the simple summation of another integral. For spars and ribs these integrals are:

$$\tilde{\mathbf{F}}_{\alpha\beta} \equiv \int_{\hat{\tilde{x}}_3+\hat{\tilde{x}}_{3D}+\frac{th_{D,skin}}{2}}^{\hat{\tilde{x}}_3+\hat{\tilde{x}}_{3U}-\frac{th_{U,skin}}{2}} \mathbf{F}^\intercal \mathbf{C}_{ij} \mathbf{F} \, \mathrm{d}\hat{x}_3 \tag{2.29}$$

$$\tilde{\mathbf{F}}'_{3\alpha} \equiv \int_{\hat{\tilde{x}}_3+\hat{\tilde{x}}_{3D}+\frac{th_{D,skin}}{2}}^{\hat{\tilde{x}}_3+\hat{\tilde{x}}_{3U}-\frac{th_{U,skin}}{2}} \frac{\mathrm{d}\,\mathbf{F}^\intercal}{\mathrm{d}\hat{x}_3} \mathbf{C}_{3\alpha} \mathbf{F} \, \mathrm{d}\hat{x}_3 \tag{2.30}$$

$$\tilde{\mathbf{F}}''_{33} \equiv \int_{\hat{\tilde{x}}_3+\hat{\tilde{x}}_{3D}+\frac{th_{D,skin}}{2}}^{\hat{\tilde{x}}_3+\hat{\tilde{x}}_{3U}-\frac{th_{U,skin}}{2}} \frac{\mathrm{d}\,\mathbf{F}^\intercal}{\mathrm{d}\hat{x}_3} \mathbf{C}_{33} \frac{\mathrm{d}\,\mathbf{F}}{\mathrm{d}\hat{x}_3} \, \mathrm{d}\hat{x}_3 \tag{2.31}$$

The unique difference between spars and ribs stays within the dependence of

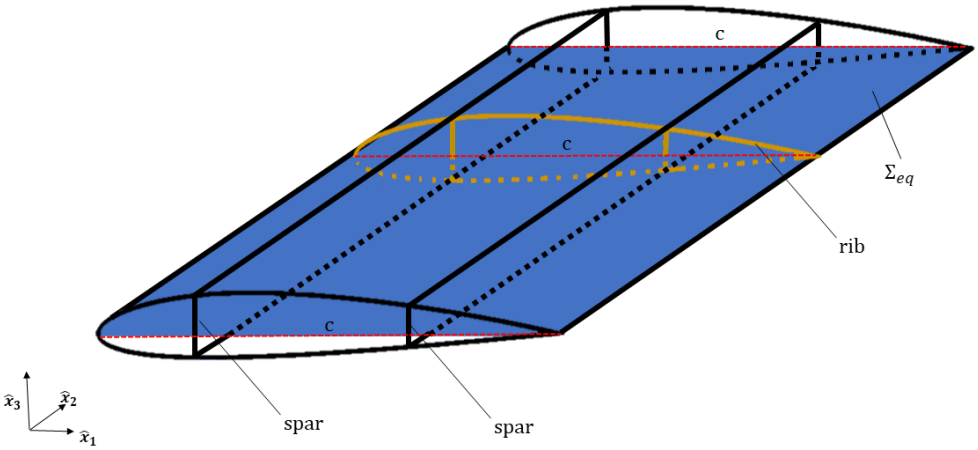

Figure 2.5: NACA2415 straight sparred-ribbed wing for EPM scheme. In gold rib section is underlined.

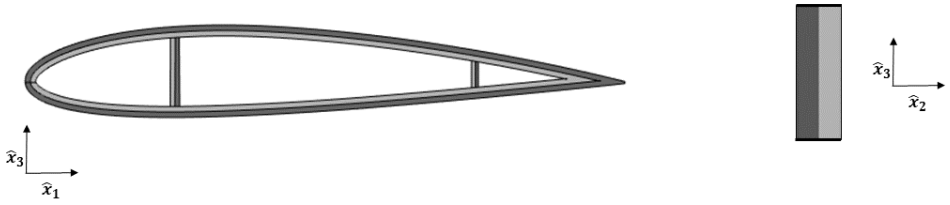

Figure 2.6: Airfoil and rib section in a composite laminate NACA2415 wing for EPM scheme.

$\hat{\hat{x}}_3$ by $\hat{x}_1$ for ribs, since straight spar's height is fixed, while rib's height changes accordingly.

In all these integral relations, if homogeneous structures are considered the constitutive relation is independent from $\hat{x}_3$ and can be taken out from the integrals. For the sake of completion, let us consider the same wing but with an heterogeneous material as in Fig.2.6.

Two layers are considered, but the next conclusions are valid for any number of layers: in fact, every layer in the skin gives a contribution which can be simply added to the previous integrals, by suitably changing C_{ij} with three-dimensional tensor transformation matrices, according to the ESL theory. For spars and ribs, the switch is instead made according to the point of integration, whether it falls in a layer or in another layer.

Renaming $\cos\gamma = C_\gamma$, $\sin\gamma = S_\gamma$ and defining similarly C_ζ, S_ζ, C_ψ and S_ψ, the three 3D tensor transformation matrices $\Xi_{\hat{x}_1,\hat{x}_2}$, $\Xi_{\hat{x}_1,\hat{x}_3}$ and $\Xi_{\hat{x}_2,\hat{x}_3}$ are

$$\Xi_{\hat{x}_1,\hat{x}_2} = \begin{bmatrix} C_\gamma^2 & S_\gamma^2 & 0 & 0 & 0 & 2S_\gamma C_\gamma \\ S_\gamma^2 & C_\gamma^2 & 0 & 0 & 0 & -2S_\gamma C_\gamma \\ 0 & 0 & 1 & 0 & 0 & 0 \\ 0 & 0 & 0 & C_\gamma & 0 & 0 \\ 0 & 0 & 0 & 0 & C_\gamma & 0 \\ -S_\gamma C_\gamma & S_\gamma C_\gamma & 0 & 0 & 0 & C_\gamma^2 - S_\gamma^2 \end{bmatrix} \tag{2.32}$$

$$\Xi_{\hat{x}_1,\hat{x}_3} = \begin{bmatrix} C_\zeta^2 & 0 & S_\zeta^2 & 0 & 2C_\zeta S_\zeta & 0 & 0 \\ 0 & 1 & 0 & 0 & 0 & 0 & \\ S_\zeta^2 & 0 & C_\zeta^2 & 0 & -2C_\zeta \S_\zeta & 0 & \\ 0 & 0 & 0 & C_\zeta & 0 & 0 & \\ -C_\zeta S_\zeta & 0 & C_\zeta S_\zeta & 0 & C_\zeta^2 - S_\zeta^2 & 0 & \\ 0 & 0 & 0 & S_\zeta & 0 & C_\zeta & \end{bmatrix} \tag{2.33}$$

$$\Xi_{\hat{x}_2,\hat{x}_3} = \begin{bmatrix} 1 & 0 & 0 & 0 & 0 & 0 \\ 0 & C_\psi^2 & S_\psi^2 & 2C_\psi S_\psi & 0 & 0 \\ 0 & S_\psi^2 & C_\psi^2 & -2C_\psi S_\psi & 0 & 0 \\ 0 & -2C_\psi S_\psi & C_\psi S_\psi & C_\psi^2 - S_\psi^2 & 0 & 0 \\ 0 & 0 & 0 & 0 & C_\psi & -S_\psi \\ 0 & 0 & 0 & 0 & S_\psi & C_\psi \end{bmatrix} \tag{2.34}$$

where γ, ζ and ψ are the three Euler angles, γ defining the orientation of the fiber, and ζ and ψ orienting the material in the other two directions of space according to the geometry. In particular ζ is coplanar with θ, that is the tangent of the airfoil upper and lower surface and thus it orients the material accordingly; on the other hand, ψ is involved in the transformation required for the rib fiber-oriented material.

2.4 Combination of CUF and FEM

The discretization of Eq.(2.9) passes through the division of the equivalent plate $\hat{\Sigma}_{eq}$ in a collection of N_e non-overlapping linear elements, which respectively define single domains $\hat{\Sigma}_{eq,e}$, so that $\hat{\Sigma_{eq}} = \bigcup_{e=1}^{N_e} \hat{\Sigma}_{eq,e}$. As a preliminary process of the integration through Gauss quadrature, in every $\hat{\Sigma}_{eq,e}$ element a set of local coordinates (ξ, η) is introduced; the shape functions $\mathbf{N}(\xi, \eta)$ are instead defined to correlate the vector of generalized displacements $\mathbf{U}$ with the nodal displacements

$\mathbf{U}_e$. Thus Eq.(2.9) becomes

$$\sum_{e=1}^{N_e} \delta \mathbf{U}_e^{\intercal} \, \mathbf{K}_e \, \mathbf{U}_e = \sum_{e=1}^{N_e} \delta \mathbf{U}_e^{\intercal} \boldsymbol{f}_e \tag{2.35}$$

where

$$\mathbf{K}_e \equiv \int_{\hat{\Omega}_{eq,e}} \left(\frac{\partial \mathbf{N}^{\intercal}}{\partial \hat{x}_\alpha} \tilde{\mathbf{F}}_{\alpha\beta} \frac{\partial \mathbf{N}}{\partial \hat{x}_\beta} + \frac{\partial \delta \mathbf{N}^{\intercal}}{\partial \hat{x}_\alpha} \tilde{\mathbf{F}}'^{\intercal}_{\alpha 3} \mathbf{N} + \mathbf{N}^{\intercal} \tilde{\mathbf{F}}''_{33} \mathbf{N} \right) \mathrm{d}\Omega \tag{2.36}$$

and

$$\boldsymbol{f}_e \equiv \int_{\Sigma_{eq,e}} \mathbf{N}^{\intercal} \mathbf{F}^{\intercal} \boldsymbol{t} \, \mathrm{d}\Sigma \tag{2.37}$$

In this work linear shape functions have been employed for the FEM elements: for validation, convergence studies have thus been conducted through h-refinement. The shape functions, organized within shape matrices, for quadrangular elements are

$$N_1 = \frac{1}{4} (1 - \xi) (1 - \eta) \tag{2.38}$$

$$N_2 = \frac{1}{4} (1 + \xi) (1 - \eta) \tag{2.39}$$

$$N_3 = \frac{1}{4} (1 + \xi) (1 + \eta) \tag{2.40}$$

$$N_4 = \frac{1}{4} (1 - \xi) (1 + \eta) \tag{2.41}$$

Consequently to Eq.(2.35), the fundamental matricial relation of FEM can be defined

$$\mathbf{K}\mathbf{U} = \mathbf{P}, \tag{2.42}$$

where $\mathbf{K}$ is the global stiffness matrix, composed by single $\mathbf{K}_e$ opportunely distributed within the global numeration, and $\mathbf{P}$ is the loading vector.

The integration over the 2D FE is processed through Gauss quadrature (see Ref.[41] and Ref.[72]), that establishes a weighted summation of the value of the function $g(x_1, x_2)$ within a local coordinate system (defined by the already mentioned (ξ, η)). For quadrilateral elements it states that:

$$\int_{\hat{\Omega}_{eq,e}} g(\hat{x}_1, \hat{x}_2) \, \mathrm{d}\Omega = \int_{-1}^{1} \int_{-1}^{1} \bar{g}(\xi, \eta) \, \bar{J}(\xi, \eta) \, \mathrm{d}\xi \mathrm{d}\eta \tag{2.43}$$

where $\bar{g}(\xi,\eta)$ is the function referred to the local coordinate system. The switch of the domain is implicitly demanded to $\bar{J}(\xi,\eta)$, which is the determinant of the Jacobian 2D matrix that connects the two different coordinate systems:

$$\mathbf{J} = \begin{bmatrix} \frac{\partial \hat{x}_1}{\partial \xi} & \frac{\partial \hat{x}_2}{\partial \xi} \\ \frac{\partial \hat{x}_1}{\partial \eta} & \frac{\partial \hat{x}_2}{\partial \eta} \end{bmatrix} \tag{2.44}$$

which can be adequately inverted according to the needs: for example, in 2D FE integration process, the inverse of the Jacobian matrix allows to calculate the derivatives of the shape functions $\mathbf{N}(\xi,\eta)$ with respect to the global coordinate system:

$$\begin{Bmatrix} \frac{\partial N_k}{\partial \hat{x}_1} \\ \frac{\partial N_k}{\partial \hat{x}_2} \end{Bmatrix} = \mathbf{J}^{-1} \begin{Bmatrix} \frac{\partial N_k}{\partial \xi} \\ \frac{\partial N_k}{\partial \eta} \end{Bmatrix} \tag{2.45}$$

Thus, the determinant $\bar{J}(\xi,\eta)$ is defined as

$$\bar{J}(\xi,\eta) = \frac{\partial \hat{x}_1}{\partial \xi}\frac{\partial \hat{x}_2}{\partial \eta} - \frac{\partial \hat{x}_1}{\partial \eta}\frac{\partial \hat{x}_2}{d\xi} \tag{2.46}$$

According to the Gauss quadrature, the integral in Eq.(2.43) becomes a double weighted summation over the number of quadrature points $\bar{N}_q$ and $\bar{M}_q$:

$$\int_{\hat{\Omega}_{eq,e}} g(\hat{x}_1,\hat{x}_2)\,\mathrm{d}\Omega = \sum_{n_q=1}^{\bar{N}_q}\sum_{m_q=1}^{\bar{M}_q} \bar{g}\left(\xi_{m_q},\eta_{n_q}\right)\bar{J}\left(\xi_{m_q},\eta_{n_q}\right) w_{m_q} w_{n_q} \tag{2.47}$$

where w_{n_q} and w_{m_q} are the weights.

In Ref.[73] and Ref.[43] the process of construction of the global stiffness matrix is accurately described. Being CUF a flexible strategy to deal with different structural theories, the mentioned process is deeply relevant for the implementation of the method, and it perfectly clarifies the hierarchical nature of the stiffness matrix, as well as of the loading vector and of the other typical FEM ingredients. In fact hierarchical submatrices of the global stiffness matrix respect the Principle of Virtual Displacements. CUF allows the identification of a *fundamental nucleus* $\mathbf{k}_{rsij}$ which is expressed according to the r,s orders in the order of expansion N_u and the numeration i,j of the finite element (see Fig.2.7). This nucleus, extractable from Eq.(2.36), represents a first step of an alternative approach of construction of the stiffness matrix, allowing to avoid the building up of strain-displacement matrices $\mathbf{B}(\xi,\eta)$ and shape matrices $\mathbf{N}(\xi,\eta)$ and solving the integrals needed by $\mathbf{k}_{rsij}$.

Nevertheless, in the code implemented for the framework presented in this The-

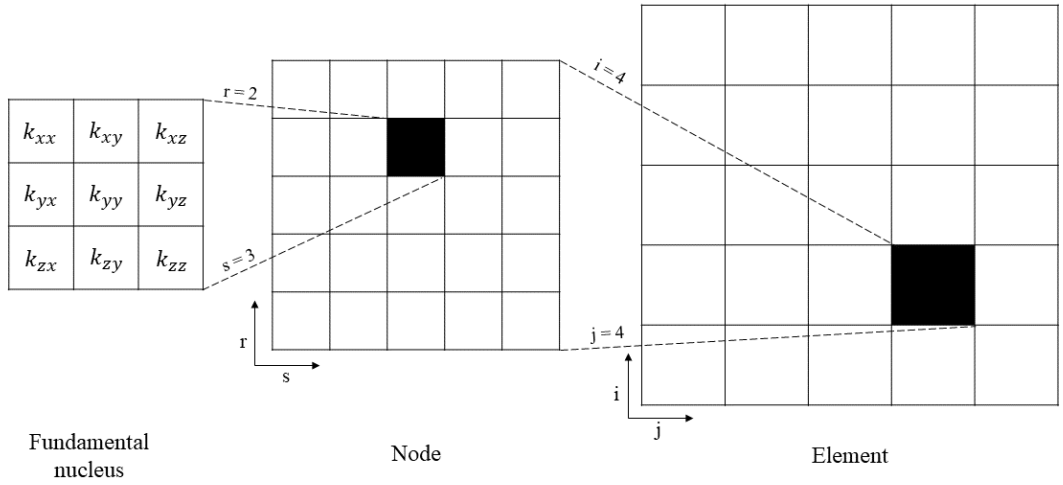

Figure 2.7: Hierarchical construction of CUF-FEM stiffness matrix (see Ref.[43]): r and s are the order of expansions, i and j refer to the numeration of the nodes within an element. Note that the numbers of order of expansion (5) and of node elements (5) are set for the sake of generality and visualization.

sis, $\mathbf{K}_e$ is directly calculated from the element matrices, to avoid an excessive number of nested for-loops and thus to make easier the application of *Selective reduced integration*, which will be explored later.

A similar "construction" process is required by the loading vector, already shown in Eq.(2.37) and that is defined according to the real 3D location of the load application on the $\hat{x}_3$ direction. In fact in Eq.(2.37) $\mathbf{F}$ is taken out from the integral and is specified for the specific application point $\hat{x}_{3app}$. Of course during the simulation $\hat{x}_{3app}$ changes according to the geometrical laws of th_{skin} as shown in Section 2.3. A summary of the method can be found in Fig. 2.8.

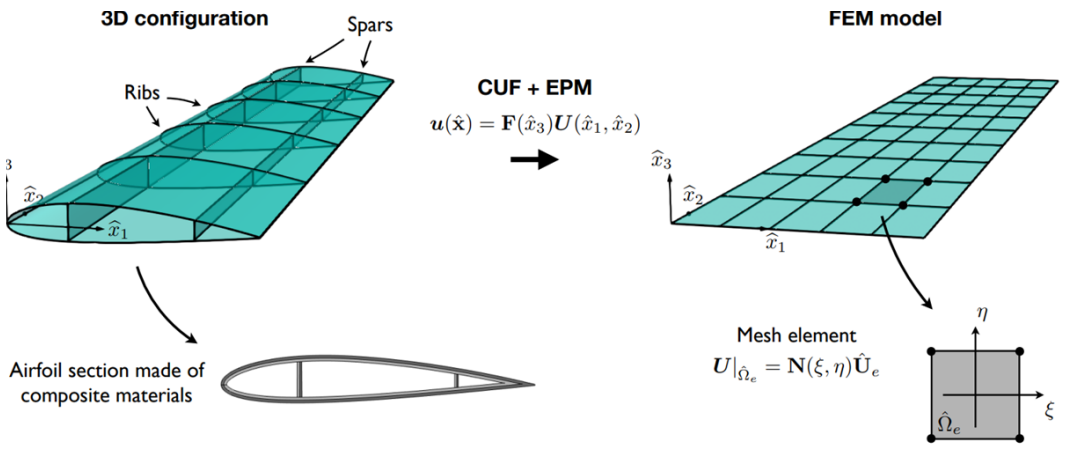

Figure 2.8: Structural CUF+FEM+EPM Solver Scheme.

For the sake of completion, also the mass matrix has been dealt with in this work, although its use in aeroelastic analyses is left for future investigation, as shown in Chapter 6. The mass matrix is obtained from the virtual variation of the inertial loads. If the material is homogeneous:

$$\delta\mathbb{L}_{ine} = \rho \int_{\hat{V}} \ddot{\mathbf{u}}\delta\mathbf{u}^{\intercal}\mathrm{d}V \tag{2.48}$$

where ρ is the density, equal in every point of the structure. Eq.(2.48) is then rewritten under the CUF+FEM specification as

$$\delta\mathbb{L}_{ine} = \int_{\hat{\Omega}_{eq}} \left(\frac{\partial\delta\boldsymbol{U}^{\intercal}}{\partial\hat{x}_{\alpha}}\tilde{\mathbf{G}}_{\alpha\beta}\frac{\partial\boldsymbol{U}}{\partial\hat{x}_{\beta}} + \delta\boldsymbol{U}^{\intercal}\tilde{\mathbf{G}}'_{3\alpha}\frac{\partial\boldsymbol{U}}{\partial\hat{x}_{\alpha}} + \delta\boldsymbol{U}^{\intercal}\tilde{\mathbf{G}}''_{33}\boldsymbol{U} \right) \mathrm{d}\Omega \tag{2.49}$$

where

$$\tilde{\mathbf{G}}_{\alpha\beta} \equiv \int_{t} \mathbf{F}^{\intercal}\rho\mathbf{I}_{d,1}\mathbf{F}\,\mathrm{d}\hat{x}_3 \tag{2.50}$$

$$\tilde{\mathbf{G}}'_{3\alpha} \equiv \int_{th} \frac{\mathrm{d}\,\mathbf{F}^{\intercal}}{\mathrm{d}\hat{x}_3}\rho\mathbf{I}_{d,2}\mathbf{F}\,\mathrm{d}\hat{x}_3 \tag{2.51}$$

$$\tilde{\mathbf{G}}''_{33} \equiv \int_{th} \frac{\mathrm{d}\,\mathbf{F}^{\intercal}}{\mathrm{d}\hat{x}_3}\rho\mathbf{I}_{d,3}\frac{\mathrm{d}\,\mathbf{F}}{\mathrm{d}\hat{x}_3}\,\mathrm{d}\hat{x}_3 \tag{2.52}$$

$I_{d,1}$, $I_{d,2}$, $I_{d,3}$ and $I_{d,3}$ are submatrices of a 6×6 identity matrix, opportunely extracted according to the dimensions defined for every $\tilde{\mathbf{G}}$ term. All the conclusions obtained in Section 2.3 can be replicated here for the definition of mass properties with complex thicknesses and complex geometries.

As it is intuitive, Eq.(2.42) can be enriched of the discretized inertial properties:

$$\mathbf{M}\ddot{\mathbf{U}} + \mathbf{K}\mathbf{U} = \mathbf{P} \tag{2.53}$$

where $\mathbf{M}$ is the global mass matrix. Analogously to the stiffness matrix, for computational purpose, also $\mathbf{M}$ can be studied since a *fundamental nucleus* format $\mathbf{m}_{rsij}$. Eq.(2.53) makes a dynamic aeroelastic analysis possible; however, it is not the subject of this Thesis, being the dynamic aeroelasticity matter of the future developments.

2.5 Shear locking and further considerations about CUF

CUF is able to reconstruct theories such as Classical Plate Theory (CPT) [74] or First Shear Deformation Theory (FSDT) [75]-[76] through penalization factors, as well explored in [43] where CPT and FSDT are defined as "particular cases of $N_u = 1$". Considering that for FSDT the kinematic hypothesis is

$$u_{\hat{x}_1} = u_{\hat{x}_{1_0}} + \hat{x}_3 u_{\hat{x}_{1_1}} \tag{2.54}$$

$$u_{\hat{x}_2} = u_{\hat{x}_{2_0}} + \hat{x}_3 u_{\hat{x}_{2_1}} \tag{2.55}$$

$$u_{\hat{x}_3} = u_{\hat{x}_{3_0}} \tag{2.56}$$

two methods are possible to obtain it from a $N_u = 1$ Higher Order Theory: a re-arrangement of rows and columns of the FEM matrices and vectors, or a penalization of the stiffness terms related to $u_{\hat{x}_{3_0}}$. Analogously, Higher Order Shear Deformation Theories (HSDT) [77], employed to refine the analysis of in-plane displacements, are obtainable.

Straightforwardly, through the penalization of the transverse shear deformation terms $\gamma_{\hat{x}_1,\hat{x}_3}$ and $\gamma_{\hat{x}_2,\hat{x}_3}$ (thus, of the constitutive relation), CPT is recreated. The employment of penalization derives from the definition of CUF, which uses the same order of expansion N_u for all the three spatial directions $\hat{x}_1, \hat{x}_2, \hat{x}_3$. Otherwise, Generalized Unified Formulation (GUF) [78] extracts from the Reissner's variational statement [79] a generalized theory that states the independence of the single orders of expansion for the three spatial directions. GUF is not employed in this Thesis but, according to new possible structural cases, it can be explored in future developments as an instrument of further refinement in the structural method.
According to [43], the thickness (Poisson) locking phenomenon [80] is solvable using a $N_u > 1$ order, because it derives from the low-order kinematic assumption over the $\hat{x}_3$ direction. Differently, shear locking [81], which can determine an overestimation of the transverse shear stiffness of thin plate, needs alternative methods to be overcome. The method performed in this research is the *Selective reduce integration* (SRI) for FEM [82]-[83], which distinguishes the integration processes for in-plane stiffness terms ($\mathbf{K}_{ip}$) and the ones for shear transverse ones ($\mathbf{K}_{sh}$). The principal consequences are with the Gauss quadrature procedure (Section 2.4, because according to this method a 4×4 quadrature is performed for $\mathbf{K}_{ip}$ and a single Gauss point procedure is performed for $\mathbf{K}_{sh}$)

$$\mathbf{K} = \mathbf{K}_{ip} + \mathbf{K}_{sh} \tag{2.57}$$

This method, successfully applied in all the test cases reported in this Thesis, nevertheless can introduce some spurious or hour-glassing [84] effects in some specific situations, such as presence of distorted mesh elements. Thus, as it can be observed in Ref.[85], a robust technique called Mixed Interpolation of Tensorial Components (MITC) can be applied. It is based on the discriminate calculation of the transverse shear components ($\gamma_{\hat{x}_1,\hat{x}_3}$,$\gamma_{\hat{x}_2,\hat{x}_3}$), and in Ref.[86] has shown its accuracy with respect to SRI in presence of distorted elements. However, employing an equivalent plate reference for every geometry, the structural meshes presented in this Thesis are most unlikely affected by the presence of this kind of elements. Thus, SRI is sufficient, and MITC is not explored in this context.

2.6 Conclusions

In this Chapter structural strategies that are employed in this work have been presented, addressing all the difficulties and the advantages of such a formulation. Both theoretical and computational aspects of the combination of FEM+CUF+EPM have been introduced, along with the description of some useful example.

Chapter 3

Aerodynamic Modelling

In this Chapter the aerodynamic models used, either as Reference or directly employed in the Thesis, are presented. Low-fidelity aerodynamics (Prandtl lifting-line theory [87], Vortex Lattice Method and Doublet Lattice Method [54] etc.) are aerodynamic strategies characterised by low computational burden [88] and simplified mathematics, very useful for conceptual stages of aircraft design and modelling. On the other hand, low-fidelity aerodynamics considers linearized aerodynamics [89] without keeping into account viscosity effects and non-linear behaviors such as separation of the flow [90] and turbulence [91]. Nevertheless, in many other circumstances low-fidelity aerodynamics have shown to be in good agreement with higher fidelity methods [92] and well-suited to be modified and corrected to keep into account non-linear phenomena [93]-[94].
In this Thesis some low-fidelity results are considered for initial validation purposes, which motivates their treatment. High-fidelity aerodynamics (Computational Fluid Dynamics [95]) are often the best strategy to observe non-linear and irregular behavior of fluids solving complex governing equations like Navier-Stokes equations [96], Reynolds-Averaged Navier Stokes equations [97] and additional turbulence modelling equations [56]-[98]. They show the relevant drawback to be extremely time-consuming [99], even though they have been implemented within commercial or open-source softwares that allow a smart automatization of the simulation even in very complex applications.
The software employed for CFD analysis in this Thesis is the open-source software `SU2` [55], successfully applied in literature for many different objectives [100]-[101]. The simplicity of configuration for CFD and the easy readability of output information of the flows have made `SU2` the most attractive possibility to automatize an high-fidelity staggered aeroelastic process as the one reported in this Thesis. Even though the use of CFD has made a compact aerostructural formulation too

complex to be explored in this context (it has been enlisted in the future developments), it has shown good and reliable results, very promising for future more compact adjoint-based coupling of the two domains [102].
First of all a theoretical review of Vortex Lattice Method and its non-linear ring version is exposed; after that, RANS equations, turbulent models and `SU2` are briefly recalled as they provide the theoretical basis for the CFD analysis performed in the test cases in the subsequent chapters; in the end, a brief summary of the main computational effort (3D meshing, output analysis, etc.) is presented. In this Chapter, the hat ˇ will denote the aerodynamic domain.

3.1 Vortex Lattice Method

Let us consider the volume $\check{\mathbb{V}}$ of the fluid in which aerodynamic bodies are submerged, and let us define the coordinate system $O\left(\check{x}_1, \check{x}_2, \check{x}_3\right)$. The continuity equation for an irrotational and incompressible fluid defined in $\check{\mathbb{V}}$ is

$$\nabla^2 \phi = 0 \tag{3.1}$$

where ϕ is the potential equation. Considering a submerged body, the fluid must not penetrate its boundary surface $\check{\Sigma}$, responding to the subsequent boundary condition

$$\nabla^2 \phi \cdot \mathbf{n} = 0 \tag{3.2}$$

where $\mathbf{n}\left(\check{x}_1, \check{x}_2, \check{x}_3\right)$ is the vector containing all the normal versor to $\check{\Sigma}$. Using the Green's second identity [103] and considering a series of possible solutions to the potential problem (i.e. source or doublet), it can be found that one solution is the vortex (see Fig.3.1).

The vortex determines the tangential velocity field around its singular central point through circulation Γ (defined as the closed integral of the vector field $\mathbf{q}_w$ along a certain line l) and radial distance r_d

$$q_{w\lambda} = -\frac{\Gamma}{2\pi r_d} \tag{3.3}$$

where $q_{w\lambda}$ stands for the tangential component of velocity q_w. Note the singularity of $q_{w\lambda}$ when $r_d = 0$.
When vortices are distributed along a line, and the circulation strength Γ_n can be defined, the Biot-Savart law can be used to compute the three-dimensional velocity field induced by the vortex itself

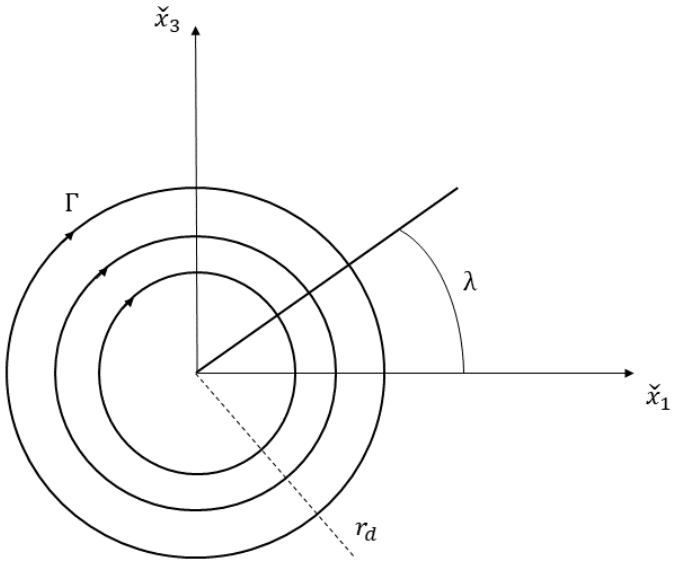

Figure 3.1: Concentric streamlines in the vicinity of a vortex singularity.

$$\mathrm{d}\mathbf{q}_w = \frac{\Gamma_n \left(\mathrm{d}\,\mathbf{l} \times \mathbf{r_d}\right)}{4\pi r_d^3} \tag{3.4}$$

In the typical horseshoe configuration employed for Vortex Lattice Method (shown in Fig.3.2), finite lines and semi-infinite lines must be distinguished.

In the case of a finite line segment AB, the integral becomes

$$q_w = \frac{\Gamma_n}{4\pi r_{d,p}} \int_{\lambda_1}^{\lambda_2} \sin\lambda \mathrm{d}\lambda = \frac{\Gamma_n}{4\pi r_{d,p}} \left(\cos\lambda_1 - \cos\lambda_2\right) \tag{3.5}$$

In the case of a semi-infinite segment

$$q_w = \frac{\Gamma_n}{4\pi r_{d,p}} \int_{\lambda_1}^{\lambda_2} \sin\lambda \mathrm{d}\,\lambda = \frac{\Gamma_n}{4\pi r_{d,p}} \left(\cos\lambda_1 + 1\right) \tag{3.6}$$

It can be demonstrated that, specifying the vectorial nature of distance $r_{d,1}$, $r_{d,2}$ and $r_{d,0}$, a velocity field vector $\mathbf{q}_w$ is calculated through

$$\mathbf{q}_w = \frac{\Gamma_n}{4\pi} \frac{\mathbf{r_{d,1}} \times \mathbf{r_{d,2}}}{\left|\mathbf{r_{d,1}} \times \mathbf{r_{d,2}}\right|^2} \left[\mathbf{r_{d,0}} \cdot \left(\frac{\mathbf{r_{d,1}}}{r_{d,1}} - \frac{\mathbf{r_{d,2}}}{r_{d,2}}\right)\right] \tag{3.7}$$

Eq.(3.7) is the fundamental equation for the construction of VLM method; thus, it is now important to highlight the nature of panelization required by VLM.
A finite wing is split up into a series of N_p panels and on every panel an horseshoe vortex is attached, so that the finite segment of the horseshoe is put at $\frac{c_p}{4}$ (being c_p

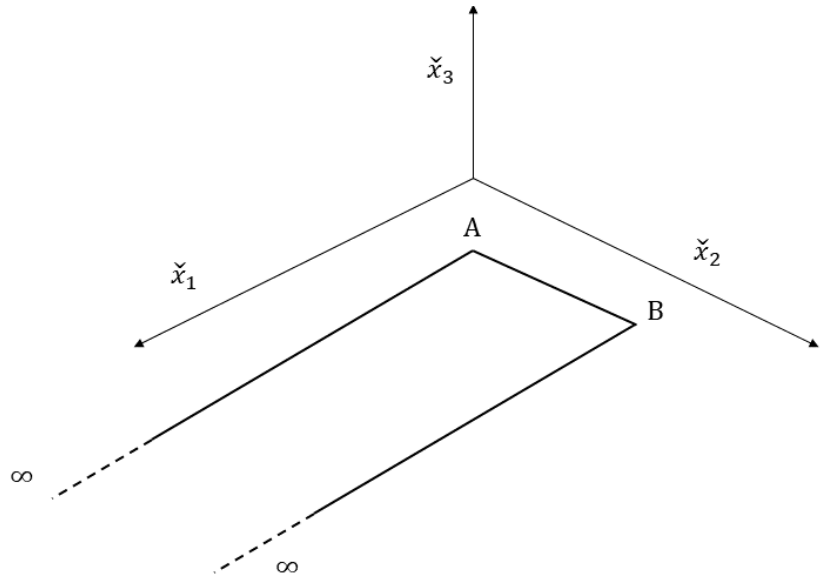

Figure 3.2: Horseshoe vortex. AB is the bound vortex; A∞ and B∞ are the trailing vortices.

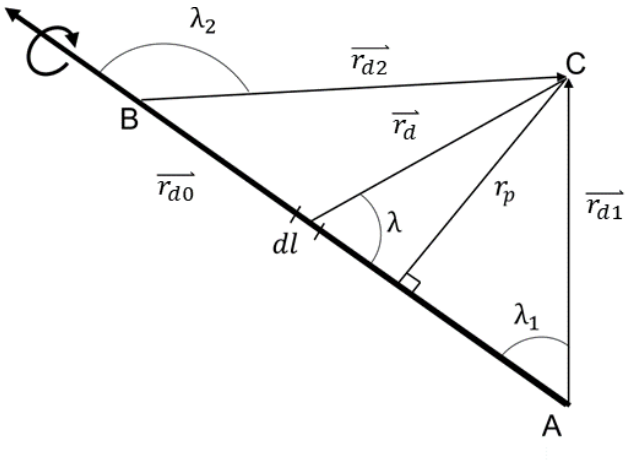

Figure 3.3: Finite vortex segment.

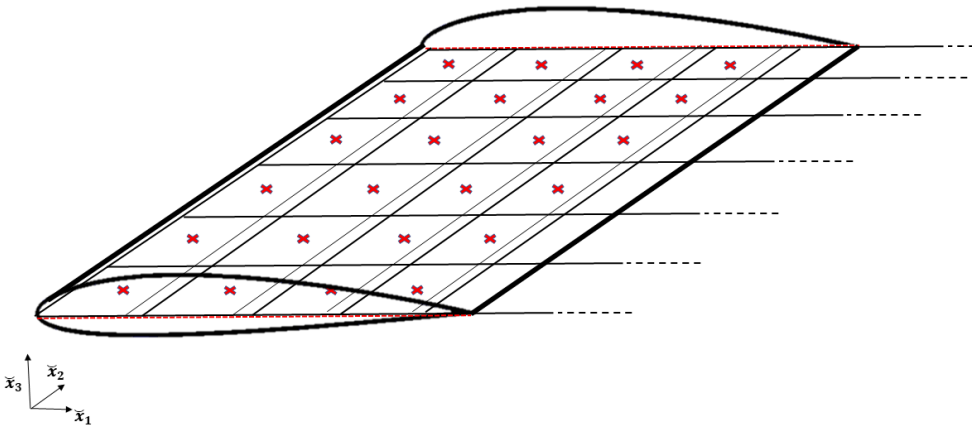

Figure 3.4: Planar distribution of vortexes on the mean aerodynamic chord plane for VLM. The thinner lines are referred to the panelization; the x symbol represents the collocation points.

the chord length of the single panel) and the "control point" is put at $\frac{3c_p}{4}$. Control points are where the flow tangency boundary condition (Eq.(3.2)) is imposed, and it is VLM practice to design them as the points where velocity is calculated. From now on in this dissertation they are indicated by the index m, while the panels are numbered with the index n. The finite segments of the panels are aligned with the local sweep angle Λ if it is present, and the panels are distributed on the reference plane defined by the mean camber line, so that the semi-infinite segments (trailing vortexes) follow a curved path until the trailing edge of the wing, where they straighten up in the direction of freestream velocity of wing parallel axis. It may happen that, for simple applications, the theory can be linearized putting the panels all over a reference plane defined by the mean aerodynamic chord and the span, thus simplifying the results from Eq.(3.7). This kind of panelization is reported in Fig.3.4

Superimposing the effects of every segment of the horseshoe vortex, the matrix $\mathbf{q}$ becomes

$$\mathbf{q}_{w_{m,n}} = \mathbf{A}_{m,n}\Gamma_n \tag{3.8}$$

where $\mathbf{A}_{m,n}$ is the *Aerodynamic Influence Coefficient*, containing all the vector information about mutual distances between control points and panel segments. Through the summation here reported

$$\mathbf{q}_{w_n} = \sum_{n=1}^{N_p} \mathbf{A}_{m,n}\Gamma_n \tag{3.9}$$

$\mathbf{q}_w$ can be expressed as a single-column matrix, which is more compatible to what follows in the formulation.

For the resolution of Eq.(3.8), the strength of vortexes Γ_n needs to be calculated. To this aim, the boundary conditions are defined to reformulate the vector $\mathbf{q}_{w_m}$. In particular, if the vortex-induced downwash of every panel at the m-th control point balances the normal component of the freestream velocity U_∞, it can be stated that

$$w_m = -U_\infty \sin(AOA) \tag{3.10}$$

where AOA is the angle of attack. Eq.(3.10) is correct for a planar wing, since any effect due to a dihedral angle Φ_d have been neglected. If small angles of attack are considered, Eq.(3.10) becomes

$$w_M = -U_\infty AOA \tag{3.11}$$

The values of w_M fill the rows of $\mathbf{q}_{w_m}$ vector, so that Eq.(3.8) can be rewritten as

$$\underbrace{\begin{bmatrix} A_{11} & A_{12} & \dots & A_{1N} \\ A_{21} & A_{22} & \dots & A_{2N} \\ \vdots & \vdots & \ddots & \vdots \\ A_{N1} & A_{N2} & \dots & A_{NN} \end{bmatrix}}_{\boldsymbol{AIC}} \underbrace{\begin{bmatrix} \Gamma_1 \\ \Gamma_2 \\ \vdots \\ \Gamma_N \end{bmatrix}}_{\boldsymbol{\Gamma_n}} = \underbrace{\begin{bmatrix} w_1 \\ w_2 \\ \vdots \\ w_N \end{bmatrix}}_{\mathbf{q_{w_m}}} \tag{3.12}$$

Thus the compact form

$$\mathbf{AIC} \cdot \mathbf{\Gamma} = \mathbf{q}_w \tag{3.13}$$

which allows the calculation of $\mathbf{\Gamma}$ through matrix inversion. The known $\mathbf{\Gamma}$ strengths, that satisfy the flow tangency boundary condition and that need no further specification being the wing planar, are included in the Kutta-Žukovskij theorem [16] for the calculation of the lift vector $\mathbf{L}$, containing force vectors distributed according to the control points location.

$$l_n = \rho_\infty U_\infty \Gamma_n \tag{3.14}$$

where l_n is the lift per unit-span and ρ_∞ is the density of the airflow impacting on the body. The derivation of this theorem can be found in Refs.[104]-[105].

Integrating l_n over the semi-span $\frac{b}{2}$ and considering a symmetrical configuration, it is obtained

$$L = 2 \int_0^{\frac{b}{2}} \rho_\infty U_\infty \Gamma \left(\check{x}_2 \right) \mathrm{d}\, \check{x}_2 \tag{3.15}$$

that can be expressed in terms of finite panels too:

$$L = \rho_\infty U_\infty \sum_{n=1}^{N_p} \Gamma_n \Delta \check{x}_{2_n} \tag{3.16}$$

where $\Delta \check{x}_{2_n}$ is the span of the single panel. These span terms can be compacted in a diagonal matrix $\mathbf{I_D}$ so to reach the definitive compact form of VLM calculation of lift for a planar wing

$$\mathbf{L} = \rho_\infty U_\infty \mathbf{I_D} \mathbf{A} \mathbf{I} \mathbf{C}^{-1} \mathbf{q}_m \tag{3.17}$$

3.2 Non-Planar Vortex Lattice Method

An extension to a non-planar framework for Vortex Lattice Method [106] is strongly suggested for some application, including staggered iterative aeroelastic strategies that employ low-fidelity aerodynamics [107]. In fact, different steps of staggered analysis of very flexible wings involve complex deformed geometries, and thus VLM needs to keep into account every new configuration of the mean camber line. It has been coupled with unsteady application in some circumstances [108], as well as in non-linear strategies for aerodynamic optimization [109]. Ref.[107] in particular represents the main reference for the aeroelastic process as presented in Chapter 4, and thus it justifies a brief treatment of NVLM in this section.

Similarly to what happens with planar VLM, the panelization is performed considering that, for each vortex, the load is computed on the mid-point of the leading edge segment (that is placed at the quarter-chord line station of the panel), and the collocation point (where flow tangency is imposed) is located at the center of the three-quarter chord line (as in Fig.3.5).

Usually a division in six segments of the vortex ring is processed, so to split the segments that are parallel to flow in two parts, with the cut corresponding to the end of a panel and the start of the rear one. At the trailing edge of the finite wing, the last ring vortex is followed by the wake vortex, whose circulation is the same of the ring finite vortexes to satisfy the Kutta condition. The wake vortex is oriented according to the freestream (thus, to the angle of attack).

The Neumann boundary condition, already presented in Eq.(3.2), is specified for this new three-dimensional configuration; thus, normal versors develop components

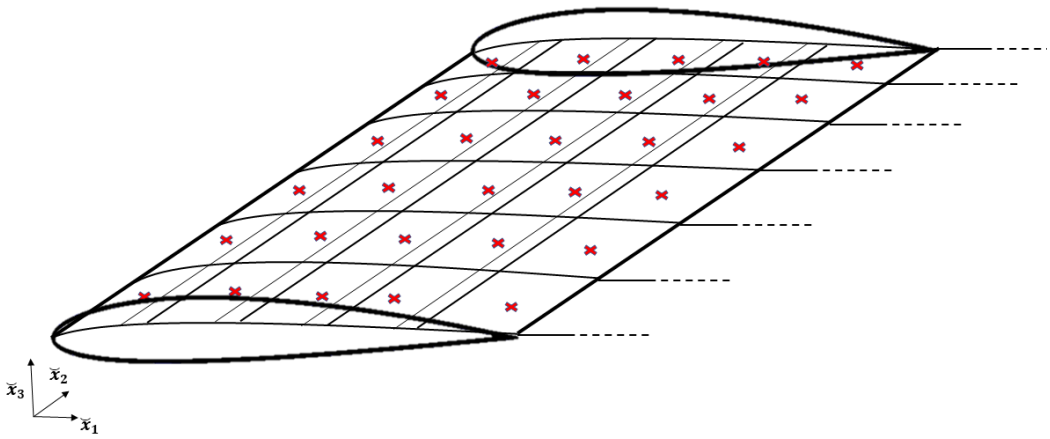

Figure 3.5: Distribution of ring vortexes for NVLM. The thinner lines are referred to the non planar panelization on the camber line surface; the x symbol represents the collocation points.

on all the three spatial directions

$$(\mathbf{U}_\infty + \mathbf{q}_{w,n})\,\mathbf{n}_n = 0 \tag{3.18}$$

where $\mathbf{U}_\infty$ is the freestream speed defined as a vector because of the three-dimensionality of the geometry; $\mathbf{q}_{coll}$ is the velocity at the collocation point of the single ring-vortex induced by all the other vortexes. The Kutta-Žukovskij theorem as already shown in Eq.(3.14) allows to solve the aerodynamic problem.

The presence of ring elements and the introduction of non planar characterization rise up some issue about the definition of circulations Γ_n. First of all, the Kutta-Žukovskij theorem needs to be clarified with respect to the orientation of the panel in the 3D space. Let us rewrite Eq.(3.14) in vectorial form so to obtain NVLM 3D-oriented loads $\mathbf{P}_{NVLM}$

$$\mathbf{P}_{NVLM} = \rho_\infty \mathbf{U}_\infty \times \mathbf{\Gamma}_{Pn} \tag{3.19}$$

where, $\mathbf{\Gamma}_{Pn}$ is the total vortex strength of the n-th panel. $\mathbf{\Gamma}_{Pn}$ is equal to $\mathbf{l}_n \Gamma'_{Pn}$ where $\mathbf{l}_n$ is a vector describing direction and magnitude of the panel's quarter-chord line segment and Γ'_{Pn} is the single vortex strength. The latter needs to become a vector for the three-dimensionality of the geometry, so it is pre-multiplied for $\mathbf{l}_n$. Moreover, Γ'_{Pn} changes according to the single ring vortex: if it is a leading edge ring vortex, $\Gamma'_{Pn} = \Gamma'_n$; if it is another ring vortex, $\Gamma'_{Pn} = \Gamma'_n - \Gamma'_{n-1}$ because of the superimposition of ring segments.

For the sake of completion, it is worth noticing that also non planar horseshoe

vortexes configuration have been employed in literature (see Ref.[110]). In this case in every panel, every vortex presents a leading edge placed at the quarter line chord, and the trailing vortexes follow the curvature of the camber through a certain number of straight segments. As in the ring case, the final semi-infinite segments is oriented according to the angle of attack. Of course, the trailing vortexes are split in a certain number of segments according to the resolution of the panelization. This represents a valid alternative for the employment of a generalized vortex lattice method; however in this research ring vortex singularities have been addressed.

3.3 Computational Fluid Dynamics (CFD)

Computational Fluid Dynamics (CFD) spans many different areas of application, from aerodynamics to hydraulics [111], from methereology [112] to biomedical engineering [113] and so on. For what concerns aerodynamics, which is studied and analysed in this research, CFD is based on the resolution of a certain number of governing equations in a discretised domain and under specified boundary conditions. The discretization allows to transform partial differential equations in a system of algebraic equations, and it is based of following discretization purposes: the domain is split in non-overlapping cells, and a certain number of nodes inside a cell is established. The accuracy and the computational analysis are related to the level of refinement of the discretization. The strategy to manage the integration over the discretised domain is, in this Thesis, the Finite Volume Method [17]; thus, every single cell can be named ”finite volume”.

The main processes observed in Finite Volume Method are the conservation of a generic variable ϕ, that can be velocity, enthalpy, etc. The governing equations monitor the time-changing entity of the studied variable splitting it into a convection term, a diffusive term and a source term. The first two terms are associated to transport phenomena, and they can be regulated by different laws. Most of times, an iterative procedure for the solving of these equation is needed. The calculation process is monitored through the residuals, which are calculated for every involved variable. When convergence is met, residuals must be small.

The discretization grid and its refinement is of primary importance for the good quality of CFD simulation results. They need to be adapted to the physical circumstances, and subject to grid independence validation. One fundamental aspect, which will be explored further on in this Thesis, is the change of mesh refinement according to the location within the domain: in an aerodynamic wing analysis, it is good use to keep into account the boundary layer effects, so a more refined mesh

in the proximity of boundary walls is recommended with respect to further finite volumes. In general it needs to be stressed that there are no other rules to obtain good quality results but experience and understatement of the coding.

3.4 The Navier-Stokes equations

To introduce Navier-Stokes equations, which are the basic partial differential equations needed to solve a CFD aerodynamic problem, some basic laws of fluid-dynamics and thermodynamics have to be considered, so to derive then the governing relations that are here of main interest. The presentation here follows Ref.[17]. Euler equations, which are employed in some of the test cases in Chapter 5, are Navier-Stokes equations specified for compressible inviscid configuration with no thermal conductivity (see e.g. Ref.[16]).

Let us consider an infinitesimal cubic volume of fluid $\delta\check{x}_1\delta\check{x}_2\delta\check{x}_3$, little enough to suppose the fluid properties of interest within it can be expressed through a Taylor series arrested at the second term. For example, considering that the origin of the Cartesian system of reference $O\left(\check{x}_1, \check{x}_2, \check{x}_3\right)$ is placed in the centroid of the cube, as it can be seen in Fig.3.6, the value of pressure $p\left(\check{x}_1, \check{x}_2, \check{x}_3\right)$ on two opposite faces (for example western and eastern faces) of the cube are respectively

$$p_W = p - \frac{1}{2}\frac{\partial p}{\partial \check{x}_1}\mathrm{d}\,\check{x}_1 \tag{3.20}$$

$$p_E = p + \frac{1}{2}\frac{\partial p}{\partial \check{x}_1}\mathrm{d}\,\check{x}_1 \tag{3.21}$$

Modelling the mass flow rate $(\rho u)\left(\check{x}_1, \check{x}_2, \check{x}_3\right)$ as it has been done with the pressure, the variation of the mass flow rate in three spatial directions can be calculated and then compacted in

$$\frac{\partial \rho}{\partial t} + \mathrm{div}\left(\rho \mathbf{u}\right) = 0 \tag{3.22}$$

which is unsteady and keeps into account the compressibility of the fluid. The divergence term is called convective term. The incompressible form of Eq.(3.22) is intuitive: suffice it to erase the unsteady derivative in t.

Through Lagrangian approach [114] the relation for a single particle allows the enunciation of conservation laws. Defining the substantial derivative $\frac{D}{Dt}$ of a generic variable ϕ as

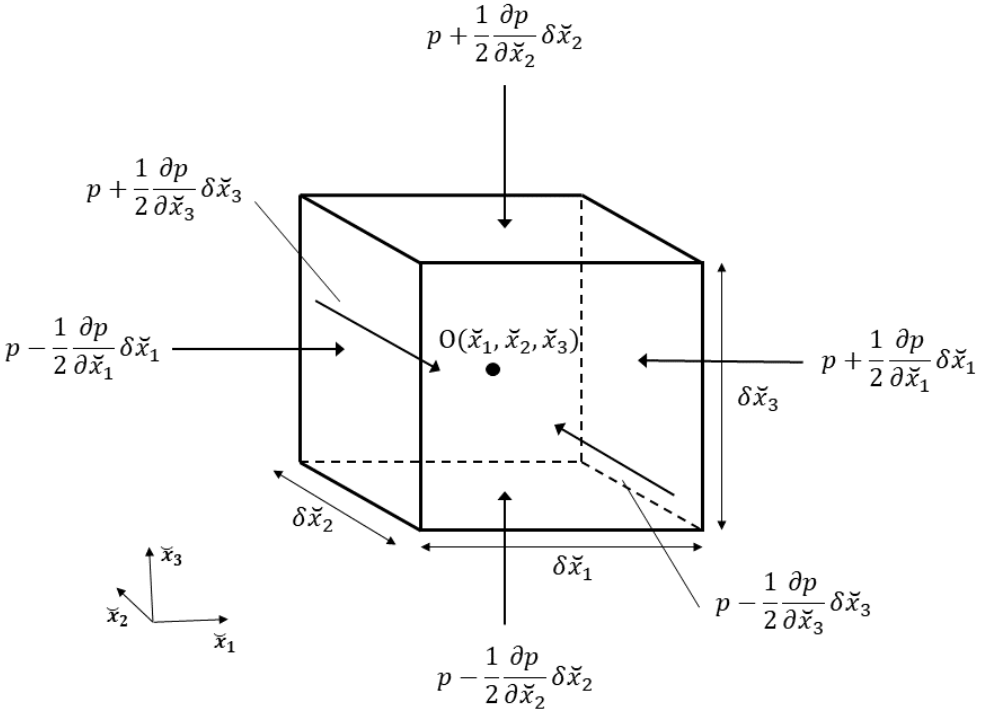

Figure 3.6: Infinitesimal fluid cubic volume.

$$\frac{D\phi}{Dt} = \frac{\partial \phi}{\partial t} + u\frac{\partial \phi}{\partial \breve{x}_1} + v\frac{\partial \phi}{\partial \breve{x}_2} + w\frac{\partial \phi}{\partial \breve{x}_3} = \frac{\partial \phi}{\partial t} + \mathbf{u} \cdot \mathrm{grad}\phi \tag{3.23}$$

the rate of change of ϕ per unit mass is found. Similarly for unit volume, with the simple addition of ρ

$$\rho\frac{D\phi}{Dt} = \rho\left(\frac{\partial \phi}{\partial t} + \mathbf{u} \cdot \mathrm{grad}\phi\right) \tag{3.24}$$

With a series of position it can be stated that the substantial derivative is equal to the sum of rate of change of a fluid property ϕ and the corresponding convective term

$$\frac{\partial(\rho\phi)}{\partial t} + \mathrm{div}(\rho\phi\mathbf{u}) =$$
$$= \rho\frac{\partial\phi}{\partial t} + \phi\frac{\partial\rho}{\partial t} + \rho\mathbf{u}\,\mathrm{grad}\phi + \phi\,\mathrm{div}(\rho\mathbf{u}) =$$
$$= \rho\left[\frac{\partial\phi}{\partial t} + \mathbf{u}\,\mathrm{grad}\phi\right] + \phi\left[\frac{\partial\phi}{\partial t} + \mathrm{div}(\rho\mathbf{u})\right] =$$
$$= \rho\frac{D\phi}{Dt} \tag{3.25}$$

because, due to mass conservation, $\phi\left[\frac{\partial\phi}{\partial t} + \mathrm{div}(\rho\mathbf{u})\right] = 0$.

The definition of substantal derivative leads to the definition of the rates of increase of $\check{x}_1$-,$\check{x}_2$-,$\check{x}_3$-momentums (through Newton's second law) and the rate of increase of energy E (through the first thermodynamic law) per unit volume (respectively $\rho\frac{Du}{Dt}$, $\rho\frac{Dv}{Dt}$, $\rho\frac{Dw}{Dt}$, $\rho\frac{DE}{Dt}$), and these are very useful for the construction of Navier-Stokes equations.

Let us consider again the infinitesimal cube of Fig.3.6, and let us consider stresses τ_{ij} within it. The sum of the contribution of stresses, combined with pressures, gives the three rates of increase of momentum

$$\rho\frac{Du}{Dt} = \frac{\partial(-p+\tau_{\check{x}_1\check{x}_1})}{\partial\check{x}_1} + \frac{\partial\tau_{\check{x}_2\check{x}_1}}{\partial\check{x}_2} + \frac{\partial\tau_{\check{x}_3\check{x}_1}}{\partial\check{x}_3} + S_{M\check{x}_1} \tag{3.26}$$
$$\rho\frac{Dv}{Dt} = \frac{\partial\tau_{\check{x}_1\check{x}_2}}{\partial\check{x}_1} + \frac{\partial(-p+\tau_{\check{x}_2\check{x}_2})}{\partial\check{x}_2} + \frac{\partial\tau_{\check{x}_3\check{x}_2}}{\partial\check{x}_3} + S_{M\check{x}_2} \tag{3.27}$$
$$\rho\frac{Dw}{Dt} = \frac{\partial\tau_{\check{x}_1\check{x}_3}}{\partial\check{x}_1} + \frac{\partial\tau_{\check{x}_2\check{x}_3}}{\partial\check{x}_2} + \frac{\partial(-p+\tau_{\check{x}_3\check{x}_3})}{\partial\check{x}_3} + S_{M\check{x}_3} \tag{3.28}$$

where $S_{M\check{x}_1}$, $S_{M\check{x}_2}$ and $S_{M\check{x}_3}$ are the $\check{x}_1$, $\check{x}_2$ and $\check{x}_3$ body forces contributions in the three spatial directions, treated as "source terms".

Let us assume then that the fluid is isotropic and that it is Newtonian (i.e. the viscous stresses are proportional to the rates of deformation). Being the deformation divisible into linear, shearing and volumetric components, two different viscous proportionality constants are required (μ_v and λ_v), and thus from Eq.(3.26) Navier-Stokes equations can be extracted

$$\rho\frac{Du}{Dt} = -\frac{\partial p}{\partial\check{x}_1} + \frac{\partial}{\partial\check{x}_1}\left[2\mu_v\frac{\partial u}{\partial\check{x}_1} + \lambda_v\mathrm{div}\,\mathbf{u}\right] + \frac{\partial}{\partial\check{x}_2}\left[\mu_v\left(\frac{\partial u}{\partial\check{x}_2} + \frac{\partial v}{\partial\check{x}_1}\right)\right]$$
$$+ \frac{\partial}{\partial\check{x}_3}\left[\mu_v\left(\frac{\partial u}{\partial\check{x}_3} + \frac{\partial w}{\partial\check{x}_3}\right)\right] + S_{M\check{x}_1} \tag{3.29}$$

$$\rho\frac{Dv}{Dt} = -\frac{\partial p}{\partial \check{x}_2} + \frac{\partial}{\partial \check{x}_1}\left[\mu_v\left(\frac{\partial u}{\partial \check{x}_2} + \frac{\partial v}{\partial \check{x}_1}\right)\right] + \frac{\partial}{\partial \check{x}_2}\left[2\mu_v\frac{\partial v}{\partial \check{x}_2} + \lambda_v \mathrm{div}\,\mathbf{u}\right] + \frac{\partial}{\partial \check{x}_3}\left[\mu_v\left(\frac{\partial v}{\partial \check{x}_3} + \frac{\partial w}{\partial \check{x}_2}\right)\right] + S_{M\check{x}_2} \quad (3.30)$$

$$\rho\frac{Dw}{Dt} = -\frac{\partial p}{\partial \check{x}_3} + \frac{\partial}{\partial \check{x}_1}\left[\mu_v\left(\frac{\partial u}{\partial \check{x}_3} + \frac{\partial w}{\partial \check{x}_1}\right)\right] + \frac{\partial}{\partial \check{x}_2}\left[\mu_v\left(\frac{\partial v}{\partial \check{x}_3} + \frac{\partial w}{\partial \check{x}_2}\right)\right] + \frac{\partial}{\partial \check{x}_3}\left[2\mu_v\frac{\partial w}{\partial \check{x}_3} + \lambda_v \mathrm{div}\,\mathbf{u}\right] + S_{M\check{x}_3} \quad (3.31)$$

Recalling $\frac{\partial}{\partial \check{x}_1}(\lambda_v \mathrm{div}\mathbf{u}) = s_{M\check{x}_1}$, $\frac{\partial}{\partial \check{x}_2}(\lambda_v \mathrm{div}\mathbf{u}) = s_{M\check{x}_2}$ and $\frac{\partial}{\partial \check{x}_3}(\lambda_v \mathrm{div}\mathbf{u}) = s_{M\check{x}_3}$, absorbing these terms into S_{Mi} and rearranging Eqs.(3.29)-(3.31), Navier-Stokes equations are written in the most useful form for the finite volume method

$$\rho\frac{Du}{Dt} = -\frac{\partial p}{\partial \check{x}_1} + \mathrm{div}\,(\mu_v \mathrm{grad}\,u) + S_{M\check{x}_1} \quad (3.32)$$

$$\rho\frac{Dv}{Dt} = -\frac{\partial p}{\partial \check{x}_2} + \mathrm{div}\,(\mu_v \mathrm{grad}\,v) + S_{M\check{x}_2} \quad (3.33)$$

$$\rho\frac{Dw}{Dt} = -\frac{\partial p}{\partial \check{x}_3} + \mathrm{div}\,(\mu_v \mathrm{grad}\,w) + S_{M\check{x}_3} \quad (3.34)$$

μ_v is a property of the fluid; λ_v is a more complex term, but for gases it can be set equal to $-\frac{2}{3}\mu_v$ [115].

It can be derived that internal energy i_e equation employing the Newtonian viscous hypothesis has a form that is similar to Eqs.(3.32)-(3.34)

$$\rho\frac{Di_e}{Dt} = -p\mathrm{div}\,\mathbf{u} + \mathrm{div}\,(k_F\,\mathrm{grad}\,T) + \Phi_d + S_i \quad (3.35)$$

where k_F is the Fourier coefficient in the heat conduction law [116] and Φ_d is a dissipation function that is proportional to the squared linear, shearing and volumetric terms through μ_v. In Eq.(3.35) both the effects of works of surface stresses and the heat effects are of course kept into account.

The similarities among these five equations (mass, momentum and energy) lead to the definition of a more general *transport* equation of the ϕ property, which is the starting point for the finite volume method.

$$\frac{\partial \rho\phi}{\partial t} + \mathrm{div}\,(\rho\phi\mathbf{u}) = \mathrm{div}\,(\Gamma_d\,\mathrm{grad}\,\phi) + S_\phi \quad (3.36)$$

where Γ_d is the diffusion coefficient. This relation allows a more general distinction among the rate of change term $\frac{\partial \rho\phi}{\partial t}$, the convective term $\mathrm{div}\ (\rho\phi\mathbf{u})$, the diffusive term $\mathrm{div}\ (\Gamma_d \,\mathrm{grad}\,\phi)$ and the source term S_ϕ.

A preliminary step towards Finite Volume Method is the introduction to the integration problem of the five partial differential equations. These are integrated in a control volume $\check{\mathbb{V}}$. Applying Gauss's divergence theorem (concerning the integration of the convective term), Eq.(3.36) can be rewritten

$$\frac{\partial}{\partial t}\left(\int_{\check{\mathbb{V}}} \rho\phi \mathrm{d}\mathbb{V}\right) + \int_{\check{\mathbb{S}}} \mathbf{n}\cdot(\rho\phi\mathbf{u})\,\mathrm{d}\mathbb{S} = \int_{\check{\mathbb{S}}} \mathbf{n}\cdot(\Gamma_d \mathrm{grad}\,\phi)\,\mathrm{d}\,\mathbb{S} + \int_{\check{\mathbb{V}}} S_\phi \mathrm{d}\mathbb{V} \quad (3.37)$$

where $\check{\mathbb{S}}$ is the boundary surface of the entire control volume $\check{\Omega}$.

Some issues come from the resolution of these equations for transonic and supersonic regimes, mainly because the arising of an inviscid region outside of the thin viscous layer. In this Thesis the treatment of such cases is tackled using `SU2` and for the treatment of the theoretical aspects that interest readers are referred to the specialized literature.

3.5 Turbulent flow and RANS equations

A fundamental parameter in defining the regime of the flow is the Reynolds number

$$Re = \frac{U_\infty l_{ch}}{\nu_v} \quad (3.38)$$

where l_{ch} is a problem characteristic length and ν_v is the kinematic viscosity of the considered fluid.

The Reynolds number is primarily the relation between inertial forces and viscous forces. A critical value of Reynolds number (Re_{crit}) defines the bounds between *laminar* flow and *turbulent* flow. Laminar flow shows ordered parallel fluid trajectories and a general smoothness; turbulent flows introduces chaotic behaviors which change trajectories and strengths, giving to the problem an intrinsic unsteady nature. Moreover, the different possible levels of stability of laminar flows represent a more or less high chance of transition from a laminar to a turbulent regime [117].

The time fluctuation of the fluid property $\phi\,(t)$ in turbulent regime requires the calculation of the time-averaged mean value Φ

$$\Phi = \frac{1}{\Delta t}\int_0^{\Delta t} \phi\,(t)\,\mathrm{d}t \tag{3.39}$$

and the identification of fluctuation term $\bar{\phi}'$, defined through

$$\bar{\phi}' = \frac{1}{\Delta t}\int_0^{\Delta t} \phi'\,(t)\,\mathrm{d}t = 0 \tag{3.40}$$

so that

$$\phi = \Phi + \bar{\phi}' \tag{3.41}$$

Let us consider an incompressible fluid with constant viscosity $\nu_v = \frac{\mu_v}{\rho}$. It is easy to establish that, in the incompressible case, continuity is imposed through $\mathrm{div}\,\mathbf{u} = 0$. Applying the time average to the components of Navier-Stokes equations, keeping into account that being $\mathbf{a}$ a fluctuating vector variable $\mathbf{a} = \mathbf{A} + \mathbf{a}'$, it stands that $\bar{\mathrm{div}}\,\mathbf{a} = \mathrm{div}\,\mathbf{A}$ and that $\mathrm{div}\,(\phi\,\mathbf{a}) = \bar{\mathrm{div}}\,\mathrm{grad}\,\Phi$, Reynolds-averaged Navier Stokes (RANS) equations can be obtained

$$\begin{aligned}\frac{\partial U}{\partial t} + \mathrm{div}\,(U\mathbf{U}) = &-\frac{1}{\rho}\frac{\partial P}{\partial \check{x}_1} + \nu_v\,\mathrm{div}\,(\mathrm{grad}\,(U)) \\ &+ \frac{1}{\rho}\left[\frac{\partial\left(-\rho\,\overline{u'^2}\right)}{\partial \check{x}_1} + \frac{\partial\left(-\rho\,\overline{u'v'}\right)}{\partial \check{x}_2} + \frac{\partial\left(-\rho\,\overline{u'w'}\right)}{\partial \check{x}_3}\right]\end{aligned} \tag{3.42}$$

$$\begin{aligned}\frac{\partial V}{\partial t} + \mathrm{div}\,(V\mathbf{U}) = &-\frac{1}{\rho}\frac{\partial P}{\partial \check{x}_2} + \nu_v\,\mathrm{div}\,(\mathrm{grad}\,(V)) \\ &+ \frac{1}{\rho}\left[\frac{\partial\left(-\rho\,\overline{u'v'}\right)}{\partial \check{x}_1} + \frac{\partial\left(-\rho\,\overline{v'^2}\right)}{\partial \check{x}_2} + \frac{\partial\left(-\rho\,\overline{v'w'}\right)}{\partial \check{x}_3}\right]\end{aligned} \tag{3.43}$$

$$\begin{aligned}\frac{\partial W}{\partial t} + \mathrm{div}\,(W\mathbf{U}) = &-\frac{1}{\rho}\frac{\partial P}{\partial \check{x}_3} + \nu_v\,\mathrm{div}\,(\mathrm{grad}\,(W)) \\ &+ \frac{1}{\rho}\left[\frac{\partial\left(-\rho\overline{u'w'}\right)}{\partial \check{x}_1} + \frac{\partial\left(-\rho\overline{v'w'}\right)}{\partial \check{x}_2} + \frac{\partial\left(-\rho\overline{w'^2}\right)}{\partial \check{x}_3}\right]\end{aligned} \tag{3.44}$$

where (U, V, W, P) are the mean value of the three velocity components and pressure, and (u', v', w', p') are their fluctuation terms.

Similar conclusions are drawn for the RANS version of transport equation (Eq.(3.36))

$$\frac{\partial \Phi}{\partial t} + \operatorname{div}(\Phi \mathbf{U}) = \frac{1}{\rho}\operatorname{div}(\Gamma_{d\Phi}\operatorname{grad}\Phi) + \left[-\frac{\partial \overline{u'\phi'}}{\partial \check{x}_1} - \frac{\partial \overline{v'\phi'}}{\partial \check{x}_2} - \frac{\partial \overline{w'\phi'}}{\partial \check{x}_3}\right] + S_\Phi \quad (3.45)$$

If the compressibility of the flow is kept into account (thus, variation of the mean density $\bar{\rho}$ is considered), continuity is given by

$$\frac{\partial \bar{\rho}}{\partial t} + \operatorname{div}\left(\bar{\rho}\tilde{\mathbf{U}}\right) = 0 \quad (3.46)$$

and RANS momentum equations assume the subsequent density-weighted averaged forms

$$\frac{\partial\left(\bar{\rho}\tilde{U}\right)}{\partial t} + \operatorname{div}\left(\bar{\rho}\tilde{U}\tilde{\mathbf{U}}\right) = -\frac{\partial \bar{P}}{\partial \check{x}_1} + \operatorname{div}\left(\mu_v \operatorname{grad}\tilde{U}\right) + \left[-\frac{\partial \overline{(\bar{\rho}u'^2)}}{\partial \check{x}_1} - \frac{\partial \overline{(\bar{\rho}u'v')}}{\partial \check{x}_2} - \frac{\partial \overline{(\bar{\rho}u'w')}}{\partial \check{x}_3}\right] + S_{M\check{x}_1} \quad (3.47)$$

$$\frac{\partial\left(\bar{\rho}\tilde{V}\right)}{\partial t} + \operatorname{div}\left(\bar{\rho}\tilde{V}\tilde{\mathbf{U}}\right) = -\frac{\partial \bar{P}}{\partial \check{x}_2} + \operatorname{div}\left(\mu_v \operatorname{grad}\tilde{V}\right) + \left[-\frac{\partial \overline{(\bar{\rho}u'v')}}{\partial \check{x}_1} - \frac{\partial \overline{(\bar{\rho}v'^2)}}{\partial \check{x}_2} - \frac{\partial \overline{(\bar{\rho}v'w')}}{\partial \check{x}_3}\right] + S_{M\check{x}_2} \quad (3.48)$$

$$\frac{\partial\left(\bar{\rho}\tilde{W}\right)}{\partial t} + \operatorname{div}\left(\bar{\rho}\tilde{W}\tilde{\mathbf{U}}\right) = -\frac{\partial \bar{P}}{\partial \check{x}_3} + \operatorname{div}\left(\mu_v \operatorname{grad}\tilde{W}\right) + \left[-\frac{\partial \overline{(\bar{\rho}u'w')}}{\partial \check{x}_1} - \frac{\partial \overline{(\bar{\rho}v'w')}}{\partial \check{x}_2} - \frac{\partial \overline{(\bar{\rho}w'^2)}}{\partial \check{x}_3}\right] + S_{M\check{x}_3} \quad (3.49)$$

where $\tilde{\mathbf{U}}$ is defined as the Favre-averaged velocity [118].

The general RANS transport equation becomes

$$\frac{\partial \bar{\rho}\tilde{\Phi}}{\partial t} + \text{div}\left(\bar{\rho}\tilde{\Phi}\tilde{\mathbf{U}}\right) = \text{div}\left(\Gamma_{d\Phi}\text{grad}\,\tilde{\Phi}\right) + \left[-\frac{\partial(\overline{\bar{\rho}u'\phi'})}{\partial \breve{x}_1} - \frac{\partial(\overline{\bar{\rho}v'\phi'})}{\partial \breve{x}_2} - \frac{\partial(\overline{\bar{\rho}w'\phi'})}{\partial \breve{x}_3}\right] + S_\Phi \quad (3.50)$$

The resolution of turbulent flow through RANS equations requires necessarily the introduction of turbulent models, such as Spalart-Allmaras [56], $k-\varepsilon$ [57] and $k-\omega$ [58]. Every turbulent model has its hypothesis, its laws and its number of equations. For example, being k the kinetic energy of the flow and being ε the viscous dissipation of k, in $k-\varepsilon$ model a transport equations of k and ε can be added to RANS equations. Similarly, in $k-\omega$ model, the transport equation of the specific rate of dissipation of kinetic energy $\omega = \frac{\varepsilon}{k}$ (turbulence frequency) is added to the governing system of PDEs. In this Thesis the above models are employed in the aeroelastic analysis and are solved using `SU2`. Further details about specific aspects can be found in Ref.[17]. Spalart-Allmaras is employed in Chapter 5, and it consists of the introduction of a single more transport equation, the transport equation of the kinematic eddy viscosity parameter $\tilde{\nu}$.

3.6 The Finite Volume Method

A brief introduction to the main features Finite Volume Method useful to follow the simulation of the test cases is given in this Chapter 5. Further details can be found in Refs.[119]-[120]-[121]-[122]).

The Finite Volume Method (FVM) is based on the discretization of the problem reference domain with a grid in which the results of the governing laws are node-wisely computed. It is based on the dimension of the problem and on the mechanics of phenomena that need to be modelled. In transport equations Eq.(3.50), as it has been said, four distinctive terms can be identified: the unsteady one, the convective one, the diffusive one and the source one. The diffusive term is the simplest term to be approached. It transports the property ϕ in all the direction of space equally and within a finite element (line, surface, volume) it can be easily addressed through central differencing scheme.

As an introductory example (see Ref.[17]), let us have a 1D diffusive problem on a line $\bar{AB}$ discretised as in Fig.3.7.

The steady state simple diffusion law is

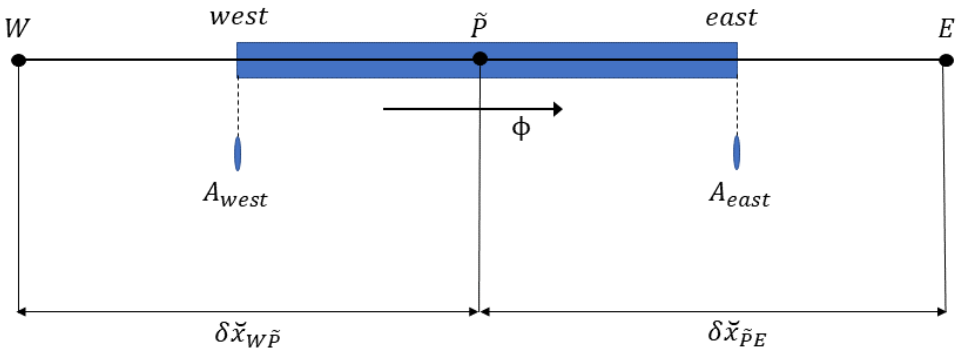

Figure 3.7: FVM 1D: scheme example.

$$\frac{\mathrm{d}}{\mathrm{d}\check{x}_1}\left(\Gamma_d\frac{\mathrm{d}\phi}{\mathrm{d}\check{x}_1}\right)+S=0 \tag{3.51}$$

The intermediate solution at point $\tilde{P}$ is managed considering the evolution of the diffusive term from east to west, so to give a numerical approximation to integral equation as the one reported in Eq.(3.37).

$$\int_{\Delta\check{\mathbb{V}}}\frac{\mathrm{d}}{\mathrm{d}\check{x}_1}\left(\Gamma_d\frac{\mathrm{d}\phi}{\mathrm{d}\check{x}_1}\right)\mathrm{d}\,\mathbb{V}+\int_{\Delta\check{\mathbb{V}}}S\mathrm{d}\,\mathbb{V} = \left(\Gamma_d A_d\frac{\mathrm{d}\phi}{\mathrm{d}\check{x}_1}\right)_{east}-\left(\Gamma_d A_d\frac{\mathrm{d}\phi}{\mathrm{d}\check{x}_1}\right)_{west}+\bar{S}\Delta\check{\mathbb{V}}=0 \tag{3.52}$$

where A_d is the section area in the diffusion phenomenon. The central difference scheme, in this case, establishes that the diffusive coefficients in the west and east point are respectively

$$\Gamma_{dwest}=\frac{\Gamma_{d\tilde{A}}+\Gamma_{d\tilde{P}}}{2} \tag{3.53}$$

$$\Gamma_{deast}=\frac{\Gamma_{d\tilde{P}}+\Gamma_{d\tilde{B}}}{2} \tag{3.54}$$

and that the diffusive terms are calculated as

$$\left(\Gamma_d A_d\frac{\mathrm{d}\phi}{\mathrm{d}\check{x}_1}\right)_{east}=\Gamma_{deast}A_{deast}\left(\frac{\phi_E-\phi_{\tilde{P}}}{\delta\check{x}_{1\tilde{P}E}}\right) \tag{3.55}$$

$$\left(\Gamma_d A_d\frac{\mathrm{d}\phi}{\mathrm{d}\check{x}_1}\right)_{west}=\Gamma_{dwest}A_{dwest}\left(\frac{\phi_{\tilde{P}}-\phi_W}{\delta\check{x}_{1W\tilde{P}}}\right) \tag{3.56}$$

Giving a similar linear approximation to the source term $S=S_u+S_p\phi_p$, it is possible to rearrange Eq.(3.52) as

$$\left(\frac{\Gamma_{deast}}{\delta\check{x}_{1\tilde{P}E}}A_{de}+\frac{\Gamma_{dwest}}{\delta\check{x}_{1W\tilde{P}}}A_{dwest}-S_p\right)\phi_{\tilde{P}}= \left(\frac{\Gamma_{dwest}}{\delta\check{x}_{1W\tilde{P}}}A_{dwest}\right)\phi_A+\left(\frac{\Gamma_{deast}}{\delta\check{x}_{1\tilde{P}E}}A_{deast}\right)\phi_B+S_u \quad (3.57)$$

that becomes

$$a_P\phi_P=a_A\phi_A+a_B\phi_B+S_u \quad (3.58)$$

This is the linear equation that defines the transport equation in correspondence to the point $\tilde{P}$ through FVM coefficients a_{FVM}. A refinement of the linear grid allows the construction of a system of linear equations, that can be solved imposing opportune boundary conditions and through iterative procedure if the system is very large.

In the diffusive case, the passage to 2D or 3D problems is simply managed, adding up to Eq.(3.58) other 4 components ϕ_C, ϕ_D, ϕ_E and ϕ_F that, two by two, define the fluxes along the other two directions of space $\check{x}_2$ and $\check{x}_3$.

The presence of a convective term, which in a steady state configuration updates Eq.(3.51) as it follows

$$\frac{\mathrm{d}}{\mathrm{d}\check{x}_1}\left(\rho u\phi\right)=\frac{\mathrm{d}}{\mathrm{d}\check{x}_1}\left(\Gamma_d\frac{\mathrm{d}\phi}{\mathrm{d}\check{x}_1}\right) \quad (3.59)$$

introduces new problems. Differently from the diffusive behavior, convectivity is strictly directed and makes the flux laws $\phi\left(\check{x}_1\right)$ more complex to be reproduced by discretization techniques. Along with a sufficiently refined mesh, the evaluation of some other grid properties is recommended: *conservativeness*, that warns about the kind of interpolation and representation of the flux along the finite element (that, if badly set, can invalidate the conservation of property ϕ); *boundedness*, which involves a confrontation among FVM coefficients a_{FVM} (that should be positive) to establish if the linear system matrix is diagonally dominant; and *transportiveness*, that employs the confrontation between the diffusive behavior and the convective behavior to evaluate if other schemes from the central differencing one are needed.

Upwind schemes [123], hybrid schemes and other kinds of scheme [124], for example Total Variation Diminishing (TVD) schemes [125], are introduced to face the convective-diffusive coupling, always leading to a FVM matrix linear problem, and changing in opportune ways the FVM coefficients.

3.7 SU2: main features and characteristics

SU2 ([126]-[127]-[128]-[55]) is an open-source suite for multiphysics design and simulation, developed at Stanford University in 2013. It is employed in this Thesis for the resolution of the aerodynamic fields, in an heterogeneous and staggered iterative aeroelastic framework, even though SU2 is able in itself to execute aeroelastic simulations and optimization procedure, combining FVM and FEM; these options are not of interest for this Thesis, and SU2 will be uniquely employed for aerodynamic analysis, because the aim is to combine CFD with the advanced structural framework as presented in Chapter 2. C++ coding language is used for the resolution of RANS equations (Eqs.(3.47)-(3.49)) and turbulent additional transport equations, as well as for mesh deformation. Both of these processes are demanded to two different built-in SU2 modules, respectively SU2_CFD and SU2_DEF, which are the modules employed in this Thesis.

In the configuration file (.cfg) needed by SU2 to perform the tests, the main requirements concern the mesh, the governing equations, the thermodynamic settings and the computational strategies.

The mesh can be received by SU2 in a .su2 format file, that provides the geometry grid, the connectivity and the kind of elements (in 2D triangles and quadrilaterals, in 3D prisms, pyramids, hexaedrals and tetrahedrals). In 3D configurations, 3D elements are separately enlisted by the 2D boundary walls ones, that are also split among the various boundary tags. For example during this research most of the times farfield, symmetry and boundary walls of the wings were given for 3D simulations with a O-type control volume (see Fig. 3.8); for all the simulations, farfield is composed by triangular elements; symmetry bound presents both triangular and quadrilateral elements; the wing walls, with their specific tags (tip wall, upside wall, downside wall, trailing edge wall), are similarly mixed in a general hybrid tria-quad 2D mesh. For farfield and symmetry see Fig. 3.9; for a detail of the wing, see Fig. 3.10.

For the generation of the mesh, the software Pointwise [129] software was employed. In Pointwise wing geometries are imported and used as base for the mesh construction. The quality of the mesh showed to be of fundamental importance for the success of the SU2 modules. Mesh quality depends on a series of factors, and no absolute rules are provided to grant it, thus mainly experience is required. The first influential factor is y^+, which is an non-dimensional number linked to the extension of the boundary layer [87] and to the fluid velocity.

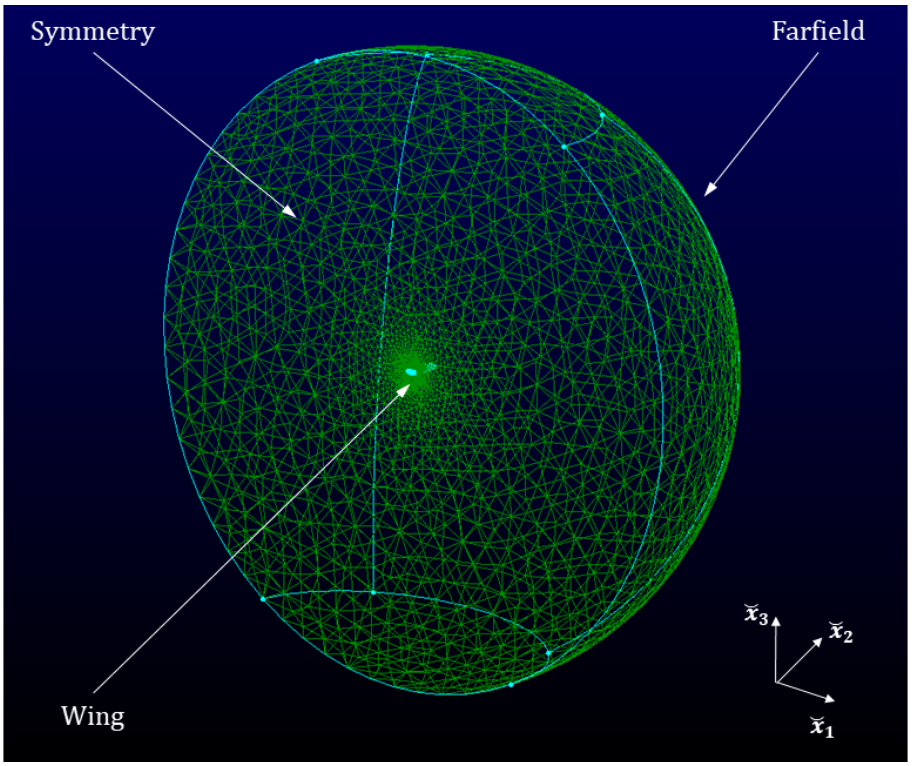

Figure 3.8: 3D view of the fluid control volume.

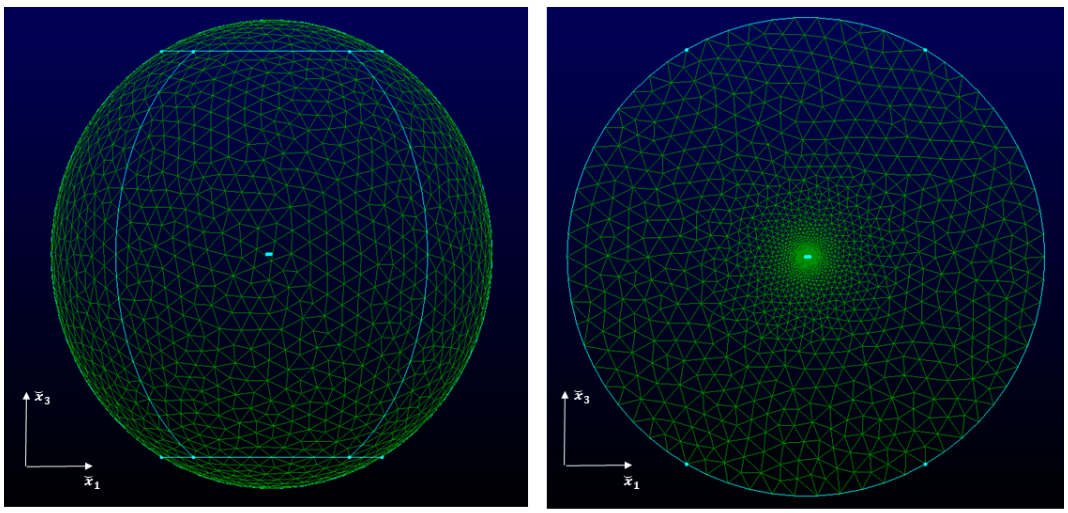

a) b)

Figure 3.9: CFD 3D control volume: $\breve{x}_1$-$\breve{x}_3$ views of farfield (a) and symmetry (b) surfaces.

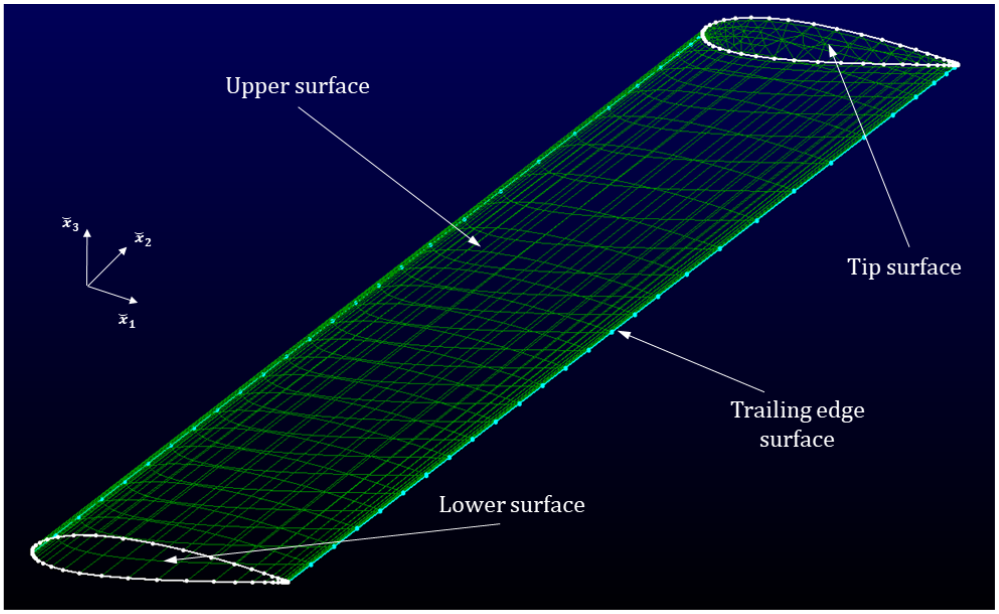

Figure 3.10: Wing walls within 3D control volume.

$$y^+ = \frac{yu_\tau}{\nu_v} \tag{3.60}$$

where y is defined as the distance from the boundary wall (disposed on $\check{x}_3$ direction) and u_τ is the friction velocity. u_τ is obtained through the boundary layer theory as exposed in Ref.[130], thus using the concepts of friction coefficient C_f, shear stress over the wall τ_{wall} and Reynolds number Re (see Eq.(3.38)) specified in $\check{x}_1$ flow direction. y^+ is an hypothesis given as input for CFD mesh generation and it determines the first spatial extension Δs of the 3D elements immediately over the boundary wing walls, in the directions defined by their normals. In practice, an hybrid 3D mesh will be created according to Δs, being specifications like extension of structured cells preliminarily given. An ill development of three-dimensional mesh can be caused by some other mesh quality factors, for example area ratio of boundary wall elements. For some other indicative suggestion for mesh quality control see Ref.[131].

Euler, Navier-Stokes and RANS governing equations are implemented in `SU2`, along with turbulent model equations. Compressible or incompressible hypothesis can be set (for example "INC_RANS"), along with the steady/unsteady option and the boundary conditions. However, in order to be conservative and to mantain generality, all the simulations from Chapter 5 are performed with compressible hypothesis. Ideal gas law is employed within the code, along with Sutherland law for viscosity [132].

A series of aero and thermodynamic inputs can be provided to the configuration options: pressure, temperature, velocity, density, viscosity, Reynolds number, as well as angle of attack (AOA, direction of the flow) and Mach number M_∞. A reference length for Reynolds number is essential; other geometric inputs are automatically calculated by `SU2` through the mesh file.

Many different calculation strategies are possible with the `SU2` suite: first of all, the convective scheme for the fluxes within the finite volumes. Jameson-Schmidt-Turkel method [133], based on the addition of a calculable artificial dissipation in the convective fluxes, and Roe method [134], that exploits variables of the neighbouring nodes in the mesh to reconstruct the convective fluxes, are the main usable methods in the program; but other methods are available as well. Secondly, the linear solver needs to be prepared. The one employed for the simulations of this Thesis is the Flexible Generalized Minimal Residual (FGMRES) method [135]. To facilitate the convergence, a linelet preconditioner is implemented (LU decomposition).

3.8 Conclusions

In this Chapter a description of planar and non-planar Vortex Lattice Method is presented to show advantages and drawbacks of a low-fidelity aerodynamic strategy. Moreover, the principal governing equations for Computational Fluid Dynamics (CFD) are described as a preamble to the use of the open-source suite `SU2`, which is widely employed in Chapter 5 to solve high-fidelity static aeroelastic test cases.

Chapter 4

Fluid-Structure Interaction and Coupling

In this Chapter the fluid-structure interaction (FSI) technique employed for the aeroelastic analysis is presented. For the sake of completion a brief description of another FSI strategy used in literature is recalled. After that, a summary of the framework is proposed, explaining the convergence criteria and the general structure for the staggered iterative strategy (see Fig.4.1).

The development of a staggered iterative aeroelastic analysis implies an heterogeneous coupling of the structural and aerodynamic domains. This kind of coupling can manage a wide range of problems in terms of geometric complexities and non-linear aerodynamic behaviors. There are many examples in literature of different fluid-structure coupling strategies for aeroelastic purposes (see Refs.[136]-[137]); some coupling procedures resort to monolithic formulations, for example employing CUF+FEM+VLM with composite wings (see Refs.[26]-[27]), or using Doublet Lattice Method and CFD to address the non-linear characteristics of the flow [138]; finally there has been a large effort to study EPM strategies for aeroelastic coupling [139]. Nevertheless, to the author's best knowledge, there is no literature about a combination of EPM+CUF+FEM+CFD.

A staggered iterative solution strategy requires a robust implementation of the fluid-structure interface. The definition of "staggered" itself establishes that there is no compact shape that puts structural and aerodynamic governing equations together in a matrix formulation.

The monolithic approach employed in Ref.[45] involves the Infinite Spline Method (IPS). Let us define a surface $\check{\Sigma}$ in a three-dimensional space $O\left(\check{x}_1, \check{x}_2, \check{x}_3\right)$: the IPS method is based on the dependency of the coordinate $\check{x}_3 \in \check{\Sigma}$ from $\check{x}_1$ and $\check{x}_2$ through a logarithmic law to process an interpolation; $\check{x}_1$ and $\check{x}_2$ are the coordinates defined

on an infinite plane, that is made co-planar with a pseudo-structural (PS) plane where a certain N_{PS} number of pseudo-structural points are distributed. Through simple processes of transformation of coordinates, both the group of load points and the group of collocation points of the panelization (as defined for VLM, see Section 3.1) are linked to the pseudo-structural points, and thus flow tangency condition is granted along with the compact implementation of a single matrix equation for FEM problem's resolution. For further details see Ref.[21].

4.1 Moving Least Square patch technique

The Moving Least Square (MLS) patch technique is an interface strategy based on conservation of momentum and energy. It is able to manage the interface between different discretization schemes, showing total independence from the single structural/aerodynamic methods. The development of the technique, extensively described in Ref.[22], starts from the coupling conditions

$$\begin{cases} \hat{\sigma} \cdot \mathbf{n} = -p\mathbf{n} + \check{\sigma} \cdot \mathbf{n} \\ \hat{\mathbf{U}} = \check{\mathbf{U}} \end{cases} \quad \text{on } \check{\Sigma} \tag{4.1}$$

that determine the subsequent definition of fluid virtual work $\check{\mathbb{L}}$

$$\delta\check{\mathbb{L}} = \int_{\check{\Sigma}} (-p\mathbf{n} + \check{\sigma} \cdot \mathbf{n}) \cdot \delta\check{\mathbf{U}} \, \mathrm{d}\, \Sigma \tag{4.2}$$

$\check{\sigma}$ and $\hat{\sigma}$ are respectively the fluid viscous stress tensor and the structural stress tensor; p is the scalar value of the fluid pressure. A classical scheme for non-matching interfaces is based on

$$\hat{\mathbf{f}}_j = \int_{\hat{\Sigma}_e} N_j \, (-p\mathbf{n} + \check{\sigma} \cdot \mathbf{n}) \, \mathrm{d}\, \Sigma \tag{4.3}$$

where N_j are the structural shape functions and $\hat{\mathbf{f}}_j$ are the nodal forces and moments, and are equal to the forces and moments induced by pressure and stresses over the wet surface $\check{\Sigma}$. Apart from the need for the two domains to have matching topologies, the above relations do not ensure conservativeness because it is not sure that the sum of nodal loads (within $\mathbf{f}_j$) are equal to the sum of the fluid loads.

Thus, an alternative relation establishing the equality between the traces of the admissible virtual displacements $\delta\check{\mathbf{U}}$ and $\delta\hat{\mathbf{U}}$ is employed. Naming this trace as $\bar{\Sigma}$ it can be written that

$$\mathrm{Tr}\left(\delta\check{\mathbf{U}}\right)|_{\bar{\Sigma}} = \mathrm{Tr}\left(\delta\hat{\mathbf{U}}\right)|_{\bar{\Sigma}} \tag{4.4}$$

To link the virtual admissible displacements of the two domains, the interpolation term h_{ij} is introduced

$$\left(\delta\check{\mathbf{U}}_i\right) = \sum_{j=1}^{\hat{N}_n} h_{ij}\left(\delta\hat{\mathbf{U}}_j\right) \tag{4.5}$$

where $\hat{N}_n$ is the number of structural grid nodes. Eq.(4.5) is then specified for the entire $\check{\mathbf{U}}$ field

$$\check{\mathbf{U}} = \sum_{i=1}^{\check{N}_n} Z_i \sum_{j=1}^{\hat{N}_n} h_{ij}\left(\hat{\mathbf{U}}_j\right) \tag{4.6}$$

where Z_i is the shape function interpolating within aerodynamic finite elements. $\check{N}_n$ are of course the number of aerodynamic grid nodes. This relation allows rewriting Eq.(4.2) involving interpolation term h_{ij}:

$$\delta\check{\mathbb{L}} = \int_{\check{\Sigma}} \left(-p\,\mathbf{n} + \check{\sigma}\cdot\mathbf{n}\right)\cdot \sum_{i=1}^{\check{N}_n} Z_i \sum_{j=1}^{\hat{N}_n} h_{ij}\left(\delta\hat{\mathbf{U}}_j\right)\mathrm{d}\,\Sigma \tag{4.7}$$

$\delta\check{\mathbb{L}}$ is put equal to the structural virtual work

$$\delta\check{\mathbb{L}} = \delta\hat{\mathbb{L}} = \sum_{j=1}^{\hat{N}_n} \hat{\mathbf{f}}_j \cdot \delta\hat{\mathbf{U}}_j \tag{4.8}$$

thus

$$\hat{\mathbf{f}}_j = \sum_{i=1}^{\check{N}_n} \check{\mathbf{F}}_j h_{ij} \tag{4.9}$$

where

$$\check{\mathbf{F}}_j = \int_{\check{\Sigma}} \left(-p\,\mathbf{n} + \check{\sigma}\cdot\mathbf{n}\right) N_j\,\mathrm{d}\,\Sigma \tag{4.10}$$

Eq.(4.9) grants the conservativeness of the energy but not the one of the velocity components between the two heterogeneous domains. To this aim the introduction of a minimization relation, based on a weight least-squares problem is required

$$\text{Minimize}\int_{\Sigma} \phi_{MLS}\left(\mathrm{Tr}\left(\delta\check{\mathbf{U}}\right)|_{\bar{\Sigma}} - \mathrm{Tr}\left(\delta\hat{\mathbf{U}}|_{\bar{\Sigma}}\right)\right)^2 \mathrm{d}\,\Sigma \tag{4.11}$$

where ϕ_{MLS} are suitable weight functions whose definition is given below. To solve Eq.(4.11) it is necessary to consistently pose the problem and to formalize the involved quantities.

Let us define a compact space $\bar{\Omega} \subseteq \mathrm{R}^{\epsilon}$, in which the function $f_{MLS} \in C^d$ is defined from its scattered values $f_{MLS}(\bar{\mathbf{x}}_A)$, $f_{MLS}(\bar{\mathbf{x}}_B)$, ..., $f_{MLS}\left(\bar{\mathbf{x}}_{N_X^*}\right)$. Being $X = \left\{\bar{\mathbf{x}}_A, \bar{\mathbf{x}}_B, \ldots, \bar{\mathbf{x}}_{N_X^*}\right\}$, the values of f_{MLS} are now researched in the alternative set of staggered points $Y = \left\{\bar{\mathbf{y}}_A, \bar{\mathbf{y}}_B, \ldots, \bar{\mathbf{y}}_{N_Y^*}\right\}$, trying to grant computational efficiency, quality of reproduction and smoothness of the resulting surface. After defining a polynomial local approximation $\bar{f}_{MLS}$ for function f_{MLS} with a m_{BF} number of basis functions (with polynomial $z_{i_{BF}}(\mathbf{x}) \in \mathbb{P}^d \subseteq C^d$), the following relation can be written

$$\bar{f}_{MLS} = \sum_{i_{BF}=1}^{m_{BF}} z_{i_{BF}}(\mathbf{x})\, a_{i_{BF}}(\mathbf{x}) \equiv \mathbf{z}_{BF}(x)^{\mathsf{T}}\, \mathbf{a}_{BF}(x) \tag{4.12}$$

Polynomials $\mathbf{z}_{BF}$ can be linear or quadratic; through a weighted least square fit (which gives the name to the technique) $\mathbf{a}_{BF}$ is determined

$$\text{Minimize } \mathbb{F}(\mathbf{x}) = \int_{\bar{\Omega}} \phi_{MLS}(\mathbf{x} - \bar{\mathbf{x}}) \left(\bar{f}_{MLS} - f_{MLS}(\bar{\mathbf{x}})\right)^2 \mathrm{d}\,\Omega(\bar{x}) \tag{4.13}$$

where

$$\bar{f}_{MLS} = \sum_{i_{BF}=1}^{m_{BF}} z_{i_{BF}}(\bar{\mathbf{x}})\, a_{i_{BF}}(\mathbf{x}) \tag{4.14}$$

Eq.(4.14) is equal to Eq.(4.11) and, through further elaborations, it is obtained that

$$\sum_{j_{BF}}^{m_{BF}} A_{ij,BF} a_{j_{BF}}(\mathbf{x}) = \int_{\bar{\Omega}} \phi_{MLS}(\mathbf{x} - \bar{\mathbf{x}})\, z_{i_{BF}}(\bar{\mathbf{x}})\, f_{MLS}(\bar{\mathbf{x}})\, \mathrm{d}\,\Omega(\bar{\mathbf{x}}) \tag{4.15}$$

where j_{BF} has been introduced to iterate over the points of Y set, and $A_{ij,BF}$ is a grouping obtained through the derivative of $\mathbb{F}(\mathbf{x})$ for minimization

$$A_{ij,BF} = \int_{\bar{\Omega}} \phi_{MLS}(\mathbf{x} - \bar{\mathbf{x}})\, z_{j_{BF}}(\bar{\mathbf{x}})\, z_{i_{BF}}(\bar{\mathbf{x}})\, \mathrm{d}\,\Omega(\bar{\mathbf{x}}) \tag{4.16}$$

A compact matrix formulation is needed to solve the problem over a finite set of staggered points; then, after setting a series of vectors and matrices

$$\mathbf{f}_{MLS} = \left[f_{MLS}\left(\bar{\mathbf{x}}_A\right), f_{MLS}\left(\bar{\mathbf{x}}_B\right), \ldots, f_{MLS}\left(\bar{\mathbf{x}}_{N_X^*}\right) \right]^{\intercal} \tag{4.17}$$

$$\mathbf{Z} = \begin{bmatrix} z_1\left(\bar{\mathbf{x}}_A\right) & z_2\left(\bar{\mathbf{x}}_A\right) & \ldots & z_{m_{BF}}\left(\bar{\mathbf{x}}_A\right) \\ z_1\left(\bar{\mathbf{x}}_B\right) & z_2\left(\bar{\mathbf{x}}_B\right) & \ldots & z_{m_{BF}}\left(\bar{\mathbf{x}}_B\right) \\ \vdots & \vdots & \ddots & \vdots \\ z_1\left(\bar{\mathbf{x}}_{N_X^*}\right) & z_2\left(\bar{\mathbf{x}}_{N_X^*}\right) & \ldots & z_{m_{BF}}\left(\bar{\mathbf{x}}_{N_X^*}\right) \end{bmatrix} \tag{4.18}$$

$$\mathbf{\Phi}_{MLS} = \begin{bmatrix} \phi_{MLS}\left(\mathbf{x} - \bar{\mathbf{x}}_A\right) & 0 & \ldots & 0 \\ 0 & \phi_{MLS}\left(\mathbf{x} - \bar{\mathbf{x}}_B\right) & \ldots & 0 \\ \vdots & \vdots & \ddots & \vdots \\ 0 & 0 & \ldots & \phi_{MLS}\left(\mathbf{x} - \bar{\mathbf{x}}_{x_X^*}\right) \end{bmatrix} \tag{4.19}$$

with $\mathbf{f}_{MLS}$ sized $N_X^* \times 1$, $\mathbf{Z}$ sized $N_X^* \times m_{BF}$ and $\mathbf{\Phi}_{MLS}$ sized $N_X^* \times N_X^*$, then Eq.(4.13) is rewritten in compact form

$$\mathbb{F}\left(\mathbf{x}\right) = \left(\mathbf{Z}\,\mathbf{a}_{MLS}\left(\mathbf{x}\right) - \mathbf{f}_{MLS}\right)^{\intercal} \mathbf{\Phi}_{MLS}\left(\mathbf{x}\right) \left(\mathbf{Z}\,\mathbf{a}_{MLS}\left(\mathbf{x}\right) - \mathbf{f}_{MLS}\right) \tag{4.20}$$

that, after minimization, gives

$$\mathbf{a}_{MLS}\left(\mathbf{x}\right) = \mathbf{A}_{BF}^{-1}\left(\mathbf{x}\right) \mathbf{b}_{MLS}\left(\mathbf{x}\right) \mathbf{f}_{MLS} \tag{4.21}$$

where $\mathbf{A}_{BF} = \mathbf{Z}^{\intercal} \mathbf{\Phi}_{MLS}\left(\mathbf{x}\right) \mathbf{Z}$ and $\mathbf{b}_{MLS}\left(\mathbf{x}\right) = \mathbf{Z}^{\intercal} \mathbf{\Phi}_{MLS}\left(\mathbf{x}\right)$.

The matrix $\mathbf{H}$ is then created from Eq.(4.7) and from Eq.(4.21), because it is composed by shape functions $\psi^d_{MLS_{j_{BF}}}$ that appear within $\bar{f}_{MLS}$

$$\bar{f}_{MLS} = \sum_{i_X^*=1}^{N_X^*} \psi^d_{MLS_{i_X^*}}\left(\mathbf{x}\right) f_{MLS}\left(\bar{\mathbf{x}}_{i_X^*}\right) \tag{4.22}$$

The resolution of $\mathrm{Minimize}\ \mathbb{F}\left(\mathbf{x}\right)$ in compact form arises the issue of the "support", which is a subset $\mathbf{\Upsilon}\left(\mathbf{x}\right)$ of solution that allows to establish a non-zero value of ϕ_{MLS} only if $\mathbf{x}_j$ is within Υ:

$$\mathbf{\Upsilon}\left(\mathbf{x}\right) := \left\{ \bar{\mathbf{x}}_{i_X^*} \in \Upsilon : \phi_{MLS}\left(||\mathbf{x} - \bar{\mathbf{x}}_{i_X^*}||\right) > 0 \right\} \tag{4.23}$$

The support is defined in the proximity of point $\mathbf{x}$. If the weight functions are positive inside the support, if the support includes enough points and if the base function is not trivial and does not vanish on $\mathbf{\Upsilon}\left(\mathbf{x}\right)$, the problem is solvable and

matrix $\mathbf{A}_{BF}$ has full rank.

In the simulations performed in this work in the further Sections, the employed weight function is the Radial Basis Function (RBF) [140]. The function ϕ_{MLS}, in this case, must be monotonically decreasing from the center to the border r_{RBF}, where $\phi_{MLS} = 0$ (as well as in general outside the support, so for $r_d > r_{RBF}$).

From the computational point of view, a routine has been implemented for the construction of $\mathbf{H}$ matrix, which is able - as it could be deduced from the above development - to transfer any quantity of interest from a domain to another, independently from the single process within a single domain. The inputs for the routine are the order of polynomials d (1 or 2), the order of the weight function and the number of points (at least 4 for linear polynomials, at least 10 for quadratic polynomials). See Ref.[22] for further details.

4.2 Coupling framework and workflow

The "staggered iterative" or "partitioned" process that allows the combination of the described tools (CUF2D+FEM+EPM+CFD) for static aeroelastic analysis requires a stable code that must be able to create a flexible link between structural outputs and aerodynamic inputs and viceversa. The aeroelastic iterations for a structure subject to static aerodynamic loads continue until the reach of a convergence, given by a user defined tolerance (in this Thesis, the tolerance $\varepsilon_{\mathbf{t}}$, defined in Eq.(4.24) below, has usually been put to 10^{-5}).

Different aerodynamic and structural conditions provide different convergence trends: as it will be shown in Chapter 5, a subsonic wing with NACA airfoil converges with a low number of iterations (e.g. about 3), while a transonic wing or a subsonic rectangular wing studied in a 3D framework can require higher number of iterations (even 7 or 9). The aeroelastic loop is automatically managed by a Python script developped in this work:

1. Every analysis starts from the calculation of FEM matrices and vectors (i.e. stiffness matrix, load vector, etc). This process is repeated once only at this stage, thus at every new iteration the stiffness matrix is not updated. An update of the stiffness matrix would arise the definition of a structurally "nonlinear" staggered iterative process; in this Thesis, "linear" partitioned static aeroelasticity is addressed.

2. After this step, the aerodynamic field all around the structure is reconstructed calling `SU2` as external solver; however, the Python code itself manages to

create the configuration file (.cfg), to run the SU2 routine (SU2_CFD, as mentioned in Section 3.7) and to read the SU2 outputs (mainly pressure values file, even though SU2, under request, can provide other info like residual trends, .vtu or .szplt files for post-processing, etc).

3. Then, the information transfer involving the interpolation matrix $\mathbf{H}$ is performed, so to have the aerodynamic loads transferred onto the structural grid ($\mathbf{H}$ is computed once and re-usable at every iteration).

4. The structural FEM problem is solved. The first result is called static structural analysis (SSA) response.

5. For any static aeroelastic analysis, SSA response is not enough because it does not fulfill the balance between structure and fluid: due to the updated deformed structural configurations, the aerodynamic loads need to be recomputed and reapplied. Thus, SU2_DEF routine is applied on the new deformed geometry to consequently deform the control volume. It employs elastic equivalence [141] to perform the deformation of the control volume, with some user defined options such as the equivalent Young modulus and the distance from the wall at which the deformation is stopped.

6. Subsequently, SU2_CFD is relaunched to recover the new aerodynamic loads.

7. Finally, the $\mathbf{H}$-converted loads are employed in FEM equation. At this stage, the comparison between the structural field $\hat{\mathbf{U}}$ coming from the present iteration (n_{it}) and the structural field of the previous iteration ($n_{it}-1$) is performed, so to elaborate an error $e\left(\Delta\hat{\mathbf{U}}_{n_{it}}\right)$ which must be compared to $\varepsilon_{\mathbf{t}}$. The convergence is reached when $\varepsilon_{\mathbf{t}} < e\left(\Delta\hat{\mathbf{U}}_{n_{it}}\right)$. The error $e\left(\Delta\hat{\mathbf{U}}_{n_{it}}\right)$ is calculated through mean least square error [142]

$$e\left(\Delta\hat{\mathbf{U}}_{n_{it}}\right) = \left[\frac{\left(\hat{\mathbf{U}}_{n_{it}} - \hat{\mathbf{U}}_{n_{it}-1}\right)^{\intercal}\left(\hat{\mathbf{U}}_{n_{it}} - \hat{\mathbf{U}}_{n_{it}-1}\right)}{\hat{\mathbf{U}}_{n_{it}-1}^{\intercal}\hat{\mathbf{U}}_{n_{it}-1}}\right]^{\frac{1}{2}} \tag{4.24}$$

The solution obtained when convergence is reached is the static aeroelastic analysis (SAA) response, and it corresponds to a balanced condition between fluid and structure. In a static regime (like cruise) this represents the constant working condition, with respect of which subsequent variations of the aeroelastic condition (deflection of high-lifting devices, acceleration or deceleration) must be calculated. The process is reported in Fig. 4.1. In this Thesis, the aeroelastic process is always

stopped when a given tolerance of 0.001% is reached out. If the given tolerance is not reached out, stages from 5 to 7 are repeated until the convergence criterion is met.

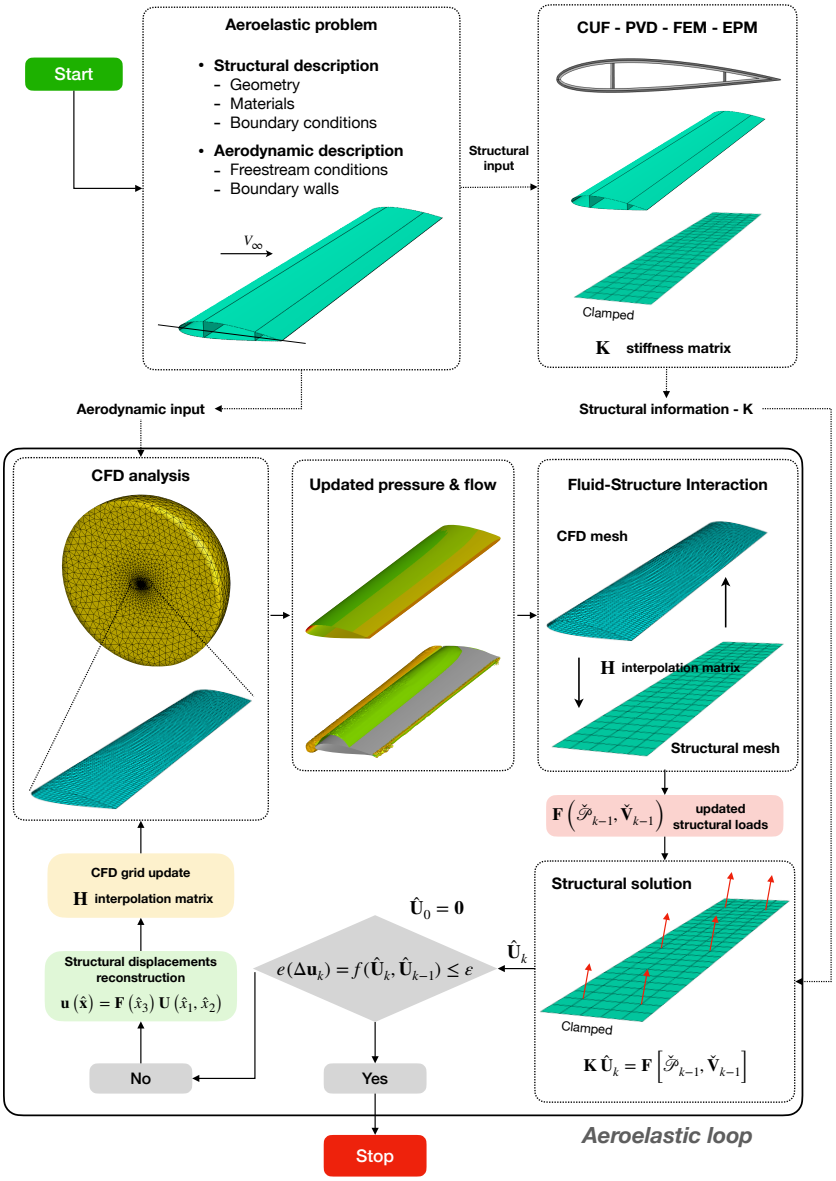

Figure 4.1: Schematic representation of the developed staggered linear static aeroelastic framework.

Chapter 5

Validation and Experiments

The static aeroelastic framework (see Chapter 4) is validated in this Chapter, so to highlight the potential, flexibility and robustness of the framework herein discussed. Several tests are presented: some tests are performed on the CUF+FEM+EPM coupling only, so to confirm the robustness of the method and to grant the efficiency of the coding (see Section 5.1); a few aerodynamic tests are described to ensure the calibration of `SU2` and of its use within the framework (see Section 5.2); a series of subsonic and transonic applications are presented (see Section 5.3); finally, two cases of preliminary aeroelastic tailoring are performed; in these two test cases, a parametric study about the influence of composite's fiber orientation on aeroelastic fundamental outputs (flexural and torsional measurements) is presented (see Section 5.4). The tests from Subsections 5.1.1-5.1.2-5.2.1-5.2.2-5.3.1-5.3.2-5.4.1 have been presented in Ref.[64]. The remaining tests have been presented in Ref.[143].

In the following, if not otherwise specified, AOA denotes the geometrical angle of attack AOA_g, defined between the aerodynamic chord and the velocity direction. If relevant, this angle is different from the zero-lift angle of attack AOA_{ZL}, defined for any NACA airfoil, and the absolute angle of attack $AOA_a = AOA_g - AOA_{ZL}$, defined between the zero-lift line and the velocity direction.

5.1 Structural validation

In this Section the accuracy of the structural model is checked. Validations are elaborated through mesh convergence criteria, considering different CUF orders of expansion N_u and comparing the results to `ABAQUS` outputs. The structural model here presented is managed by a Python script. Mesh topology and material properties are the principal inputs for the script, along with the CUF order of expansion (N_u) and the order of interpolation for FEM (equal to 1 for all the simulations here

presented). In case of a composite laminate material, stacking sequence and thickness are additional inputs. Selective Reduced Integration (see Section 2.5) is set at the beginning of the analysis as well.

5.1.1 Structural analysis of a composite plate

Figure 5.1 reports the convergence analysis, with respect to a reference finite element solution, of two laminated plates of size $a \times a \times th$ with $a = 25\,\mathrm{mm}$ and $th = 1\,\mathrm{mm}$, clamped on the four sides and subject to a uniform load $q = 0.01\,\mathrm{N/mm^2}$. Two different stacking sequences are examined, namely $[0/90]_s$ and $[0/75/90]$, and the individual plies exhibit the material properties of graphite-epoxy T300/N5208, as described in Ref.[144] and summarized in Table 5.1. Three orders of expansion $N_u = N_{u_1} = N_{u_2} = N_{u_3}$ are considered in the CUF kinematic approximation, see Eq.(2.1), for the through-the-thickness variation of the displacements, and four Gauss points are used for the quadrature of the stiffness contributions. The percentage error $e_{\%}$ is evaluated against ABAQUS, considering the maximum plate vertical displacement.

Property	**Value**
E_1	127.56 GPa
E_2, E_3	13.03 GPa
G_{23}, G_{31}, G_{12}	6.41 GPa
ν_{23}, ν_{31}, ν_{12},	0.3
ρ	1.535×10^{-6} kg/mm^3

Table 5.1: Material properties for graphite-epoxy T300/N5208 from Ref.[144].

In this context, a validation of the mass matrix implementation has been performed on the same $[0/90]_s$ laminated plate. Setting $N_u = 1$, which implies a Taylor-like expansion stopped at the first term in the three directions of space, the first four modes of vibrating of the structure are studied according to the number of elements per side in Fig.5.2. In addition to that, a visual comparison between the displacement fields from present framework and ABAQUS is presented in Fig.5.3. This test validates the implementation of composite laminated plates in terms of structural stiffness and mass. Further details about future employment of mass properties in aeroelasticity are described in Chapter 6.

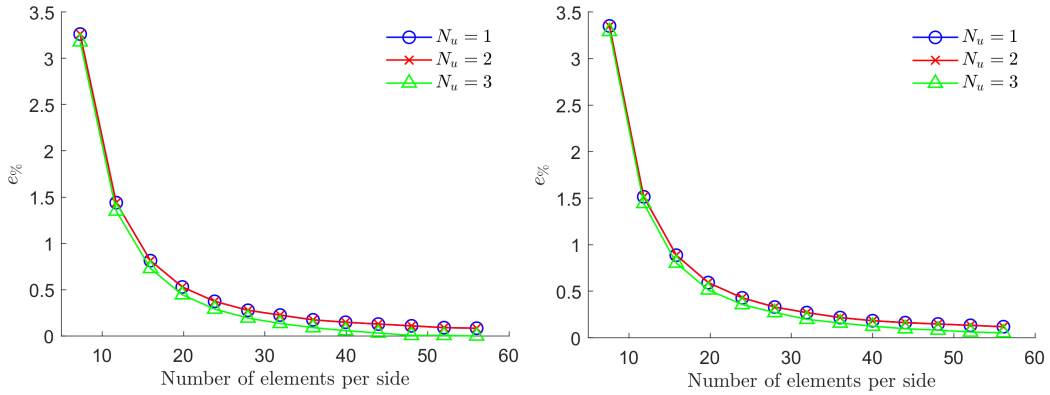

(a) [0/90/90/0] **(b)** [0/75/90]

Figure 5.1: Convergence with respect to reference FE solutions for the linear analysis of composite laminated plates: percentage error $e_{\%}$ *versus* number of elements used in the analysis for the maximum vertical displacement of the plates. Presented results refer to square $a \times a \times th$ plates, with $a = 25\,\mathrm{mm}$ and $th = 1\,\mathrm{mm}$, clamped on the four sides and loaded by a uniform transverse load $q = 0.01\,\mathrm{N/mm^2}$; the lay-ups are *a*) [0/90/90/0] and *b*) [0/75/90] and the individual plies are in graphite-epoxy T300/N5208. The reference solution is computed with ABAQUS using (250×250) linear quadrilateral 3D shell elements.

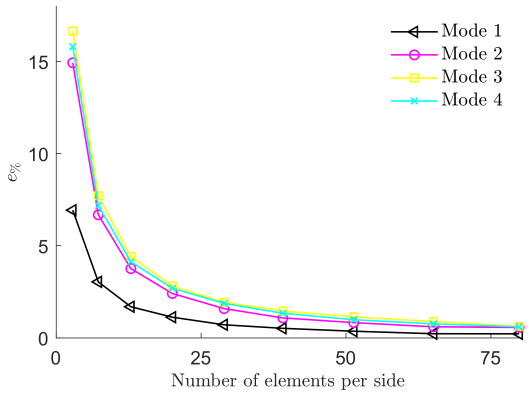

Figure 5.2: Convergence analysis for FEA with linear elements: x-coordinate is the percentage of error $e_{\%}$ and y-coordinate is the number of elements per side. The mapped result is the vibration frequency registered through the resolution of the eigenvalue problem for a composite laminated plate sized $25\,\mathrm{mm} \times 25\,\mathrm{mm} \times 1\,\mathrm{mm}$ and clamped at the four sides. The order of expansion is $N_u = 1$ and the ply sequence is $[0/90]_s$. Results are compared with ABAQUS output.

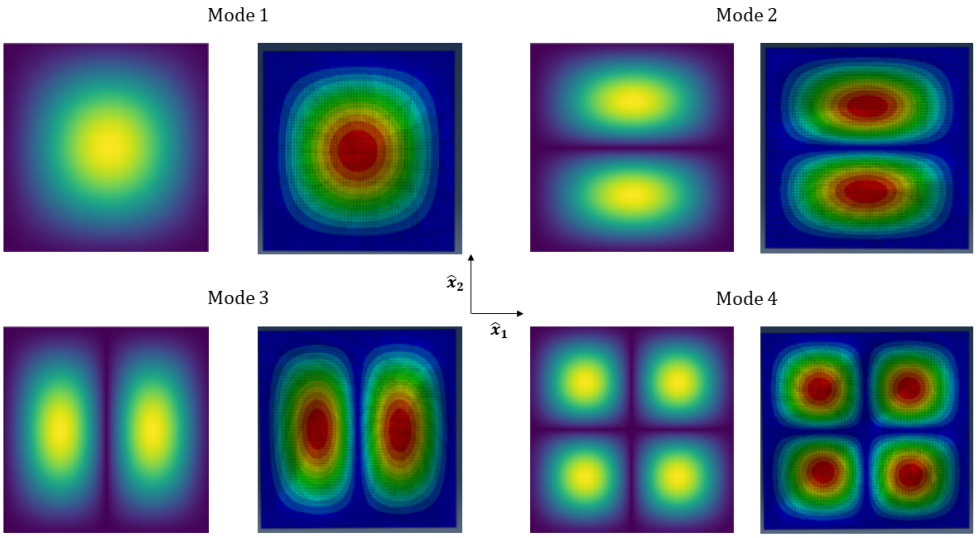

Figure 5.3: Visual comparison of the first four vibrational modes of a square composite laminated plate with $[0/90]_s$ stacking sequence, clamped at the four sides and sized $25\,\mathrm{mm} \times 25\,\mathrm{mm} \times 1\,\mathrm{mm}$. The comparison is performed between present framework and ABAQUS.

5.1.2 Structural analysis of a composite straight wing

The composite straight wing with NACA2415 airfoil studied in this Section is the one analyzed in Ref.[27], and it considers the same material properties from Table 5.1. It presents a span $b = 5\,\mathrm{m}$, a constant chord c of $1\,\mathrm{m}$ and a skin thickness th_{skin} equal to $6\,\mathrm{mm}$. Being $h = 0.15c$ the maximum height of the airfoil, the wing is then composed of two vertical spars located at 25% and 75% of the chord and respectively thick $th_{spar1} = 0.1h$ and $th_{spar2} = 0.07h$. The composite is a bi-laminated $[0/90]$ sequence, stacked as shown in Fig. 5.5. The wing is subject to two different loading configurations: a uniform load $q_{l,bend} = 1\,\mathrm{N/mm^2}$ applied on the downside of the structure upwards, and a distributed load $q_{l,tors}$ distributed on the downside part of the wing ahead of the first spar upwards and on the upside part of the wing after the second spar downwards. In both of these cases, the wing is clamped at its root section. Fig.5.4 shows the general set up reporting the ABAQUS mesh, even if the real number of elements (order of 10^5) is reduced for the sake of visualization.

A parametric study on the mesh is performed, to calibrate the spacing of the 2D FE in critical geometrical features, like the high-curvature of the leading edge. The mesh (elaborated through the software Gmsh, see Ref.[145]) is always adapted to the geometry; the occurrences of different wings with the same general geomet-

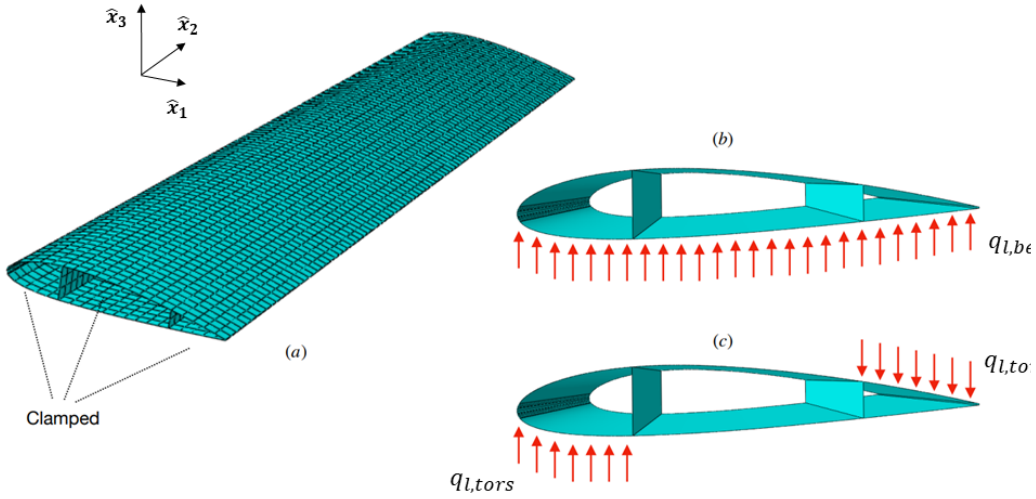

Figure 5.4: Loading condition of the straight composite wing shown through the ABAQUS mesh (a). b) bending-dominated loading $q_{l,bend} = 1\,\mathrm{N/mm^2}$; c) torsion-dominated loading $q_{l,tors} = 100\,\mathrm{N/mm^2}$. The wing is clamped at its root section.

rical configuration (skin, spars, ribs) allow to automatize the process of meshing, distributing the elements as more suitable for the EPM integrals. In particular, elements are generated within the geometrical critical regions (such as the skin in the leading edge, see Fig.2.4). In Fig.5.6 a typical surface mesh for the structural problem is presented: it is a mesh strategy that is applied to all the wings studied in this Thesis.

The results are presented in terms of mesh convergence. For the bending-dominated case the error over the bending parameter $u_{\hat{x}_3}$ is mapped, considering two different number of nodes along the chord (see Fig.5.7). Note that the maximum displacement is located at the trailing edge of the tip section. In Figs.5.8a-5.8b, the convergence of the error with respect to the bending parameter $u_{\hat{x}_3}$ and $\Delta u_{\hat{x}_3} = u_{\hat{x}_3}(0, b, 0) - u_{\hat{x}_3}(c, b, 0)$ is presented, and the maximum displacement is observed at the leading edge of the tip section.

The convergence trends show that there is a slight dependancy on the number of elements along the chord; on the other hand, the increase of N_u represents an important improvement in the accuracy of the result, especially for the torsion-dominated case.

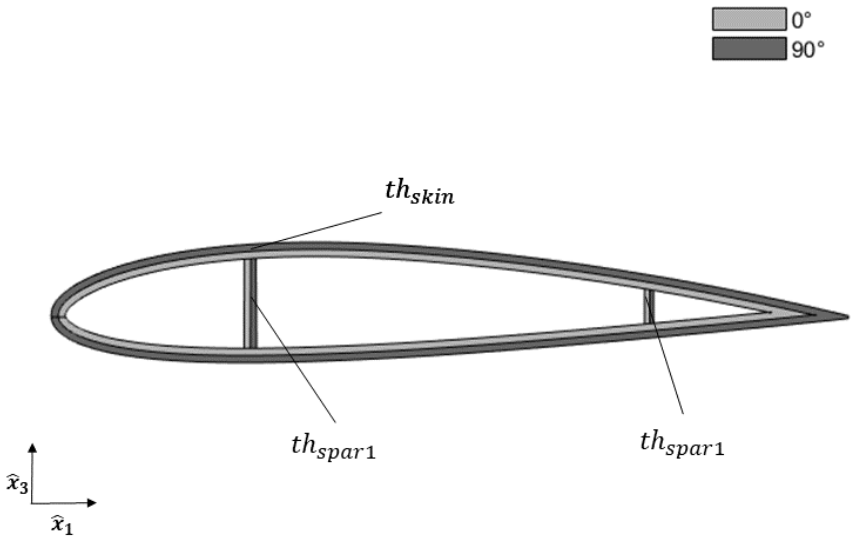

Figure 5.5: NACA2415 airfoil with a $[0/90]$ composite laminate.

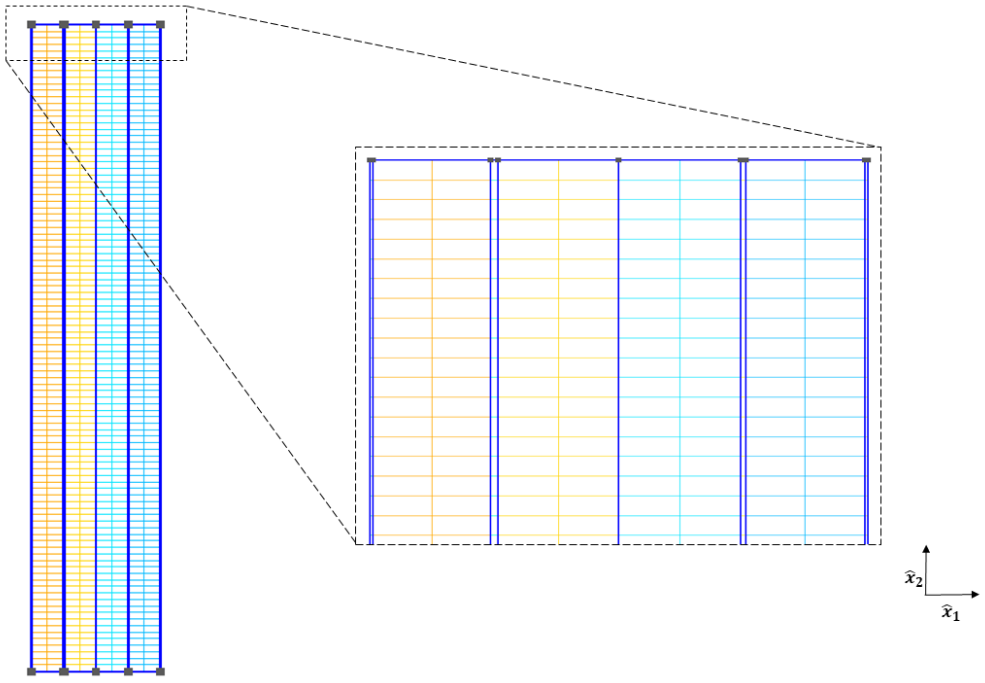

Figure 5.6: Structural mesh of the 2D model for the straight wing. The number of elements refers to the first acceptable result in Fig.5.7, i.e. 100 nodes along the chord. The different colors are the default of `Gmsh` for the discretization of different geometrical regions.

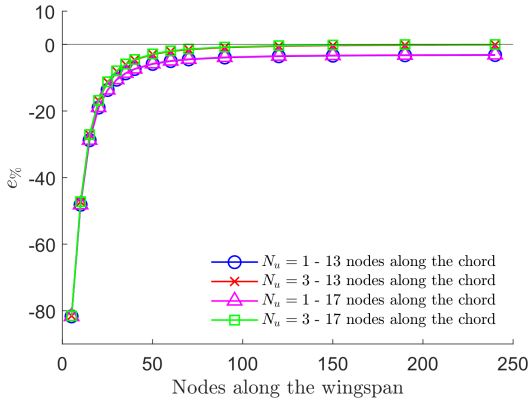

Figure 5.7: EPM validation: NACA2415 wing with two spars in composite laminate $[0/90]$ subject to a bending-dominant loading: convergece of the error for the bending parameter $u_{\hat{x}_3}$ calculated at the tip section, difference between 13 and 17 nodes along the chord, and comparison with ABAQUS benchmark.

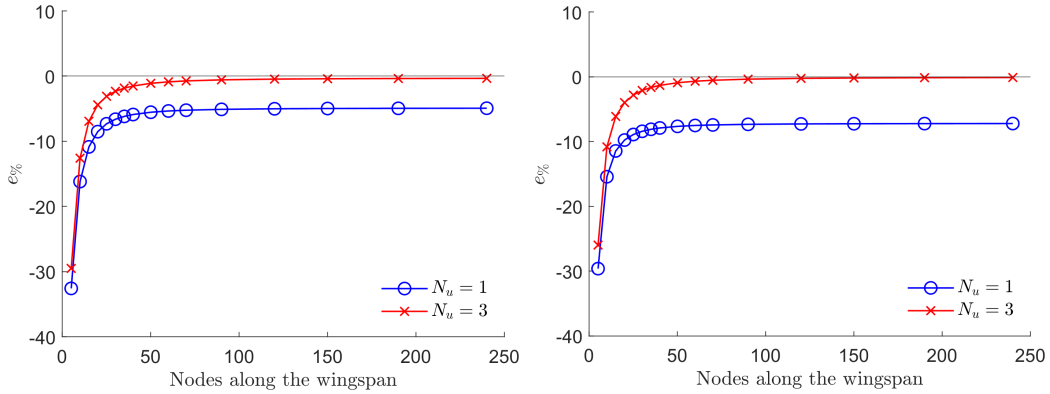

(a) $u_{\hat{x}_3}$ **(b)** $\Delta u_{\hat{x}_3}$

Figure 5.8: EPM validation: evaluation of the error for the bending parameter $u_{\hat{x}_3}$ and the torsion parameter $\Delta u_{\hat{x}_3}$ in a torsion-dominated case for a NACA2415 straight composite wing.

5.1.3 Structural analysis of a A320-like forward swept wing subject to a freestream

A swept–forward wing derived from an approximated representation of an A320-type wing is considered [146]. The forward sweep angle is $\Lambda_{c/4} = 20.55°$; there is no dihedral angle and a taper ratio $\lambda = 0.326$. The chord at the root is $c_{root} = 5.221\,\mathrm{m}$ and the root–to–tip span is $b = 17.89\,\mathrm{m}$. Throughout the wing span, the airfoil is a NACA 0112, with similar maximum thickness and camber as typical supercritical airfoils used at the mid–span of the B737 [147]. For the wing structural box, properties are uniform along the span, with the front spar placed at 15% and the rear spar at 60% of the chord. The spar thickness is taken to be $th_{spars} = 0.0175\,\mathrm{m}$, averaging the values available in the literature between $0.015\,\mathrm{m}$ and $0.020\,\mathrm{m}$. For the wing skin, the thickness of $th_{skin} = 0.015\,\mathrm{m}$ is chosen from the available range between $0.005\,\mathrm{m}$ and $0.025\,\mathrm{m}$. The wing box counts 25 ribs, including the two ribs at the root and tip sections, uniformly distributed along the span. The rib thickness is $th_{rib} = 0.008\,\mathrm{m}$. The stacking sequence for the composite material is $[0/45/90]$, as in Ref. [146]. The material properties are given in Table 5.2 and a schematic of this test case is depicted in Fig. 5.9.

The structure is loaded with a load distribution calculated from CFD. The aerodynamic loads are generated at a freestream Mach number $M_\infty = 0.78$, angle of attack $AOA = 2.0°$, and dynamic pressure $q_d = 9700\,\mathrm{Pa}$. Navier–Stokes equations are solved with the laminar flow hypothesis. A preliminary study has been carried out to guarantee grid independent results. It was found that a grid of about 1.3 million elements (pyramids, tetrahedrals, prisms and hexahedrals), with a farfield placed at 50 chords from the wing and a $y^+ = 1$ was suitable for the loads prediction needed herein. Reference load coefficients are for $C_L = 0.247$ and $C_D = 0.00724$. The aerodynamic loads at these freestream conditions are applied once onto the structure. The resulting structural response features coupled bending and torsion deformation.

Property	Value
E_1	$90\,\mathrm{GPa}$
E_2, E_3	$7.05\,\mathrm{GPa}$
G_{23}, G_{31}, G_{12}	$3.03\,\mathrm{GPa}$
ν_{23}, ν_{31}, ν_{12},	0.35

Table 5.2: Material properties for carbon fibre composite from Ref.[146].

Fig.5.1 reports the percent error in the vertical displacement of the leading edge

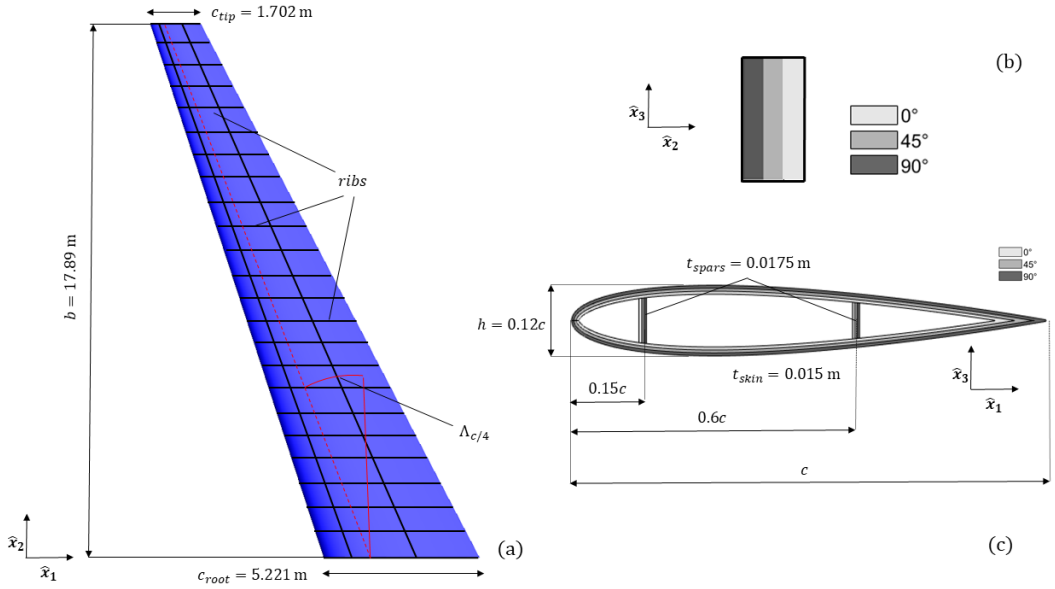

Figure 5.9: Scheme for the A320-like wing: in a) the planform of the wing is illustrated; in b) the layup for the rib section is presented; in c) there is the third view that defines the layup for the airfoil section.

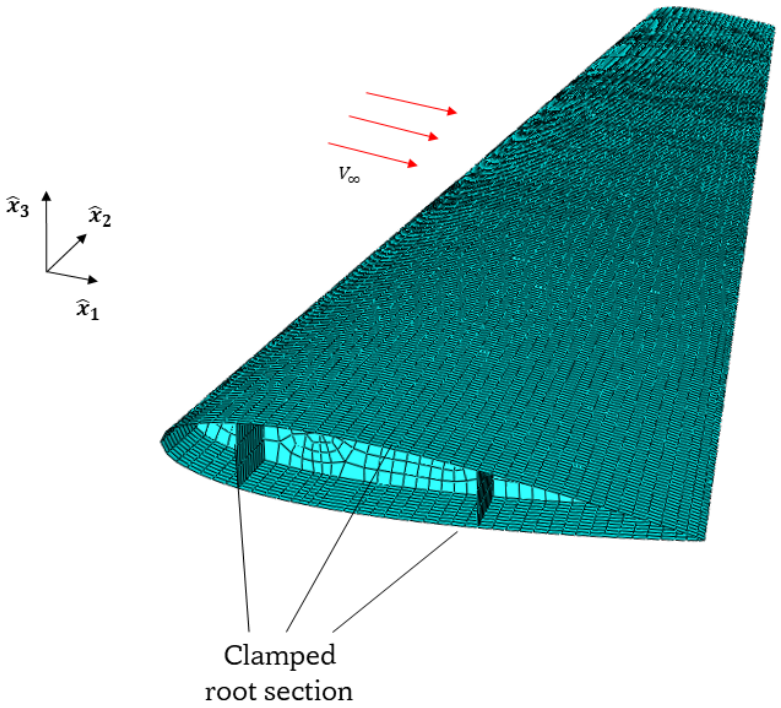

Figure 5.10: Loading and boundary conditions for an A320-like forward swept wing.

at the tip section, $\bar{u}_{\hat{x}_3}$ (see Eq.(5.1)), and the counterpart for the elastic twist at the same tip section, $\Delta\bar{\varepsilon}$ (see Eq.(5.2)).

$$\bar{u}_{\hat{x}_3} = \frac{u_{\hat{x}_3,LE,tip} + u_{\hat{x}_3,TE,tip}}{2} \tag{5.1}$$

$$\Delta\bar{\varepsilon} = \arctan \frac{u_{\hat{x}_3,LE,tip} - u_{\hat{x}_3,TE,tip}}{c_{tip}} \tag{5.2}$$

The reference solution is obtained here from ABAQUS on the pre–computed air loads distribution. From the present results for $N_u = 1$ and $N_u = 3$, a monotonic trend is observed for increasing number of nodes along the wing span. In all cases, the number of nodes along the chord was set to 15. A characteristic *knee point* is found where a trade–off between improving the prediction accuracy and limiting the computing cost exists. The trend for $N_u = 1$ shows a residual error, which is eliminated when $N_u = 3$ is considered. The low order structural theory, $N_u = 1$, is suited for predicting the torsional behaviour of a relatively simple structural cross section, such as a flat plate or a wing with few components. Predictions become more inaccurate for complex structural cross sections, as the current test case, calling for higher order kinematics. At the tip, the wing flexes up of $0.266\,\mathrm{m}$, measured at the leading–edge, with a nose–up torsion of $0.664°$. This type of structural response is common for a swept–forward wing, which tends to self–loading.

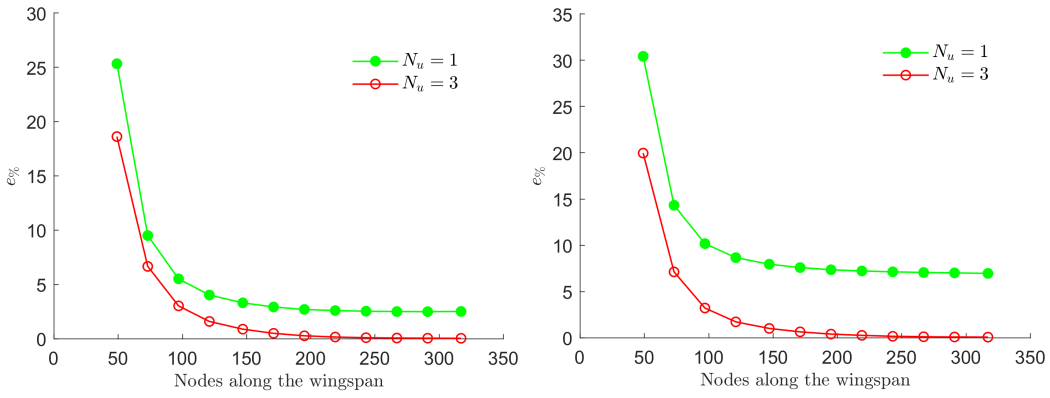

(a) $\bar{u}_{\hat{x}_3}$ **(b)** $\Delta\bar{\varepsilon}$

Figure 5.11: EPM validation: mesh convergence for bending-torsion coupling on an A320-like wing with respect to aeroelastic parameter $\bar{u}_{\hat{x}_3}$ (a) and $\Delta\bar{\varepsilon}$ (b), considering an aerodynamic loading ($M_\infty = 0.78$, $AOA = 2°$). 15 nodes along the chord.

5.2 Aerodynamic calibration

The open-source suite SU2 has been employed in literature for a wide range of different engineering applications (for example Ref.[60]); however, the correct use of SU2 outputs and their link to the present structural script are essential for the automatization of aeroelastic simulations. Preliminary studies were carried out to set the best practice to obtain good CFD predictions, with attention to mesh generation and grid convergence, as the quality of the initial CFD grid is critical to maintain a good grid quality during the iterative process of mesh deformation and warping, see Fig.4.1. The influence of two terms of the CFD grid is evaluated for this purpose: dimension of farfield and y^+. The match between the results obtained by the performed computations and some benchmark experimental and computational results was assessed at this stage.

5.2.1 Aerodynamic CFD calibration for a NACA 4415 airfoil

The first aerodynamic analysis for SU2 calibration is a 2D CFD analysis of an asymmetrical airfoil NACA 4415 studied with RANS equations with two different turbulence models: SA (one additional governing equation) and with $k-\omega$ (two additional governing equations). For the mesh convergence, more 2D O-type farfield configurations have been elaborated and tested (from an extension of $30c$ to one of $100c$) and three y^+ values (0.75, 0.9, 1) have been adopted. $d_f = 200c$ and $y^+ = 0.9$ are selected; thus a standard simulation (with $Re = 10^6$ $U_\infty = 29.22\mathrm{m/s}$ and sea level conditions) is elaborated, changing angle of attack AOA in an interval of values (0°-12°) proposed in Ref.[148], which is the benchmark to validate the calibration. In Fig.5.12 the 2D computational domain (48400 2D elements) and a zoomed detail of the surroundings of the airfoil are presented; the results are shown in Fig.5.13. The refinemenent of the grid near leading edge and trailing edge in Fig.5.12 is due to the need to recover accurate results from higher curvature regions.

Note that the differences registered for high values of AOA can be explained because of the difference control volume and discretization employed in the present research (structured mesh, $y^+ = 0.9$, O-type grid) and in literature (unstructured mesh, $y^+ = 15:40$, C-type domain), as well as to the different computational aerodynamic software (ANSYS FLUENT [149] in the reference, against SU2). These different settings are elaborated here in compatibility with the subsequent aerodynamic and aeroelastic simulations, and to underline the use of conservative hypothesis (advanced high-fidelity aerodynamics governing equations and a finer mesh

grid), that ensures an even higher accuracy. These differences are also preparatory for the mismatches registered in Section 5.3 when rectangular wing aeroelastic analysis is observed.

The reference denotes the over-prediction of its CFD $k-\omega$ C_L results with respect to the experimental results, coming from Ohio State University (OSU) [150] and XFOIL software (XFOIL) [151]. It is worth noting that both OSU and XFOIL give different results; in C_L the under-prediction of present `SU2` results (still in critical AOA region) has a lower error compared to the reference results of OSU values – the main benchmark to consider; in C_D comparison, present SA results show a more accurate output than the reference SA one, and OSU reference is well reproduced by present results (both SA and $k-\omega$) at least until the critical AOA value.

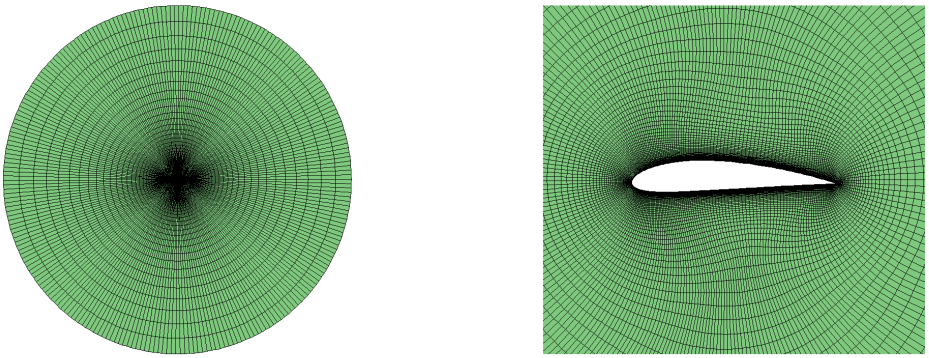

(a) Control Volume 2D **(b)** Detail of the airfoil

Figure 5.12: NACA 4415 - CFD 2D domain.

5.2.2 Aerodynamic CFD calibration for a subsonic straight wing

A further analysis is performed on a 3D NACA0012 straight wing ($c = 0.48\text{m}$, $b = 1.738c$), compared with results from Ref.[152], with computational data (SAAB FP) and with IRPHE experimental results. The mid-semi-span C_p profile is reconstructed for $Re = 10^6$, $M_\infty = 0.18$ and $AOA = 12°$; the CFD grid is composed by nearly 2 millions (1854555) 3D elements ($c \times b = 80 \times 150$ on the wing wet surface), generated by `Pointwise` with $y^+ = 0.25$, $d_f = 100c$; the aerodynamic problem is solved through RANS-SA governing equations and an O-type domain. The level of refinement of the present mesh configuration is higher than the one from IRPHE reference (50000 3D elements, C-type domain). `SU2` outputs show to be in good agreement with the results coming from the reference, in particular

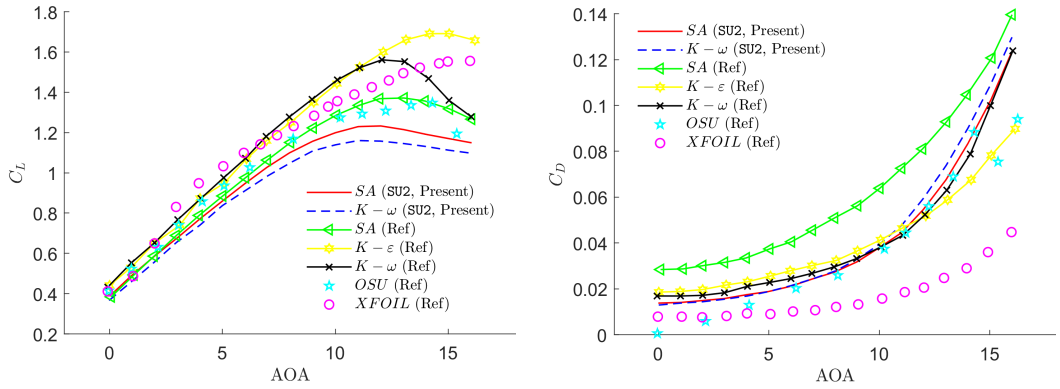

Figure 5.13: Computational results for a NACA4415 airfoil ($Re = 10^6$, $U_\infty = 29.22\,\mathrm{m/s}$, $d_f = 200c$, $y^+ = 0.9$, 200 linear nodes on the airfoil and 48400 2D elements in the domain) against computational and experimental results (Ref.[148]) - C_L and C_D vs. AOA [°].

with SAAB FP computational results that are used in the reference as benchmark of IRPHE experiments results and employs a full potential solver for the flow (see Fig.5.14).

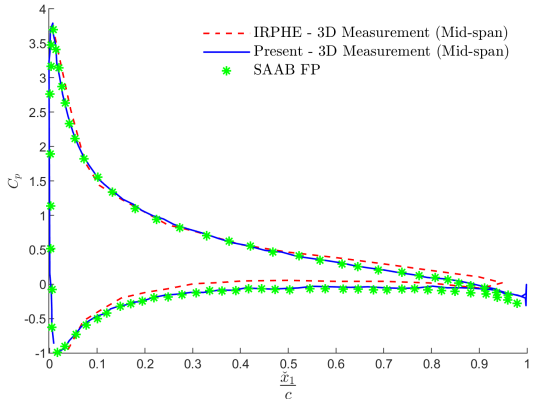

Figure 5.14: Pressure coefficient C_p distribution around NACA 0012 airfoil (mid-span) at $M_\infty = 0.18$ and $AOA = 12°$; "IRPHE - 3D Measurement (mid-span)": CFD data from Ref. [152], "SAAB FP" computational data coming from Ref. [152], "Present": `SU2` data using Spalart-Allmaras equations with laminar flow ($Re = 10^6$, $y^+ = 0.25$, $d_f = 100c$, 80 nodes on the chord direction, 150 nodes on the span direction, 1854555 3D elements in the domain).

5.3 Aeroelastic validation

The tests described in this Section introduce the employment of the staggered iterative linear static aeroelastic analysis as presented in Section 4.2 and in Fig.4.1. All the practical strategies, from the employment of `SU2` routines to convergence

criteria for aeroelastic loops, are the ones exposed in Sections 3.7 and 4.2. The test cases here presented span from subsonic applications to transonic simulations, with an observation of post-processing CFD data and variable mapping. In aeroelastic results, the difference between static structural analysis (SSA) response and static aeroelastic analysis (SAA) response is stressed, similarly to what done by Carrera et al. in Ref.[65]. SSA response is the simple displacement field caused by the straight application of aerodynamic loads onto the structure, without ensuring the balance between fluid and structure; SAA is the final step of the aeroelastic process, when balance is reached out. More details can be found in Section 4.2. Even though SSA does not represent a physical result, and it is only a numerical step in the computation, it represents an useful information about the staggered iterative process: an higher number of iterations corresponds to an higher difference between SSA and SAA.

5.3.1 Aeroelastic analysis of an isotropic subsonic rectangular wing

The first validation test case of a static aeroelastic analysis is performed for a clamped, rectangular aluminium plate. The plate has a span $b = 5\,\mathrm{m}$, chord $c = 1\,\mathrm{m}$ and thickness $th = 20\,\mathrm{mm}$. The freestream angle of attack is $AOA = 1°$, and three flow velocities, $V_\infty = 10$, 30, and $50\,\mathrm{m/s}$, are considered. In Ref.[27], this configuration was studied employing the VLM [54], the Infinite Spline Method [21] and 20 B4 structural mesh elements. The maximum vertical displacement at the leading edge of the tip section was chosen to assess convergence and accuracy of the results. In that work, results were compared to the response provided by `NASTRAN` sol 144 (thus, FSDT theory is employed).

Herein, the structural equivalent plate model is combined with the CFD solver [17] through the MLS patch technique. Since the mesh spacing near the wall $\Delta s\,(y^+)$ depends from U_∞, the CFD 3D meshes (generated by `Pointwise`) for the three velocities are different: for $U_\infty = 10\,\mathrm{m/s}$ 1023729 3D elements are generated; for $U_\infty = 30\,\mathrm{m/s}$ 1098721 3D elements; finally for $U_\infty = 50\,\mathrm{m/s}$ 1054935 3D elements.

After some preliminary evaluations, a structural 2D mesh comprised of 1036 in-plane linear elements is selected. The chosen distribution of elements follow the consideration given in Chapter 2. Navier-Stokes equations with a laminar hypothesis have been employed for the fluid analysis in `SU2`.

This test is a first demonstration of the flexibility and accuracy of the proposed strategy, and it considers a 3D control volume, which evaluates the rectangular wing

Property	Value
E_1, E_2, E_3	$69\,\mathrm{GPa}$
ν_{23}, ν_{31}, ν_{12},	0.33

Table 5.3: Material properties for aluminium.

not as a 2D plate but as a volume bulk with sharp edges.

The three different U_∞ regimes show differences in the iteration trends, as shown in Figs.5.15a-5.15c-5.15e, with respect to the leading edge tip displacement, according to the phenomena activated in the flow when it meets the physical wing boundary. An increase in the results is obtained by increasing the CUF order of expansion N_u, which allows a relevant improvement in the accuracy. Figs.5.15b-5.15d-5.15f present the trends of mean square errors measured on the structural displacement field, stopped when the convergence criterion (0.001%) is met. Fig.5.16 shows the comparison between the undeformed configuration, the SSA-deformed configuration and the SAA-deformed configuration. The various residual evolutions from the entire aeroelastic coupling are mapped in Fig.5.17: every iteration showed to converge in nearly 600 inner CFD iterations setting in `SU2` a CFD convergence tolerance on the lift value of 10^{-5} and a CFL number equal to 5, preferring accuracy over time optimization.

With $N_u = 3$ and $U_\infty = 30, 50\mathrm{m/s}$, the present framework accurately reproduces the result from the literature benchmark, showing the comparable accuracy of low-fidelity 2D VLM and high-fidelity 3D CFD for simple subsonic applications; on the other hand, $U_\infty = 10\,\mathrm{m/s}$ results present a huge error with respect to the benchmark (see Table 5.4). That is likely due to the viscous effects increasing with the decrease of Reynolds number, determining influential non-linear effects in the resulting flow. These effects are not detectable by VLM, which is not equipped of the necessary background theory to return the mechanics of the flow as shown in Fig.5.18 for $U_\infty = 50\,\mathrm{m/s}$. In Fig.5.19 the velocity streamlines for $U_\infty = 10\,\mathrm{m/s}$ are considered to show the formation of vortexes in the proximity of the leading edge. Finally, in Fig.5.20 the low pressure region for the three speeds are visualized for a further observation of the three-dimensional behavior of the fluid. The computational cost required for the analyses is approximately 134 node CPU hours for $V_\infty = 10$ m/s, 318 node CPU hours for $V_\infty = 30$ m/s, and 180 node CPU hours for $V_\infty = 50$ m/s.

This example demonstrates how, even for such simple configuration, low-velocity freestream regimes may give rise to non-linear fluid phenomena that may become influential in applications such as energy harvesting through highly-flexible micro

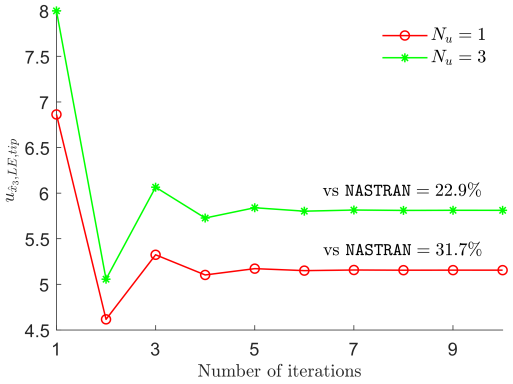

(a) LE tip displacement (mm) for 10 m/s

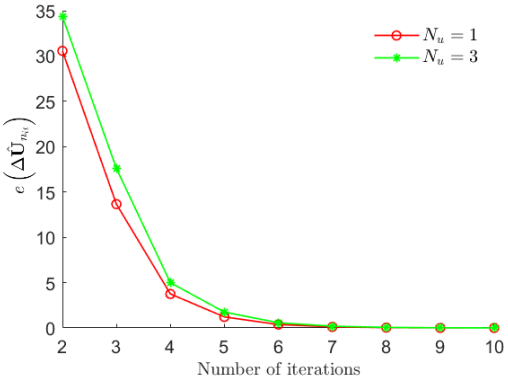

(b) Error for 10 m/s

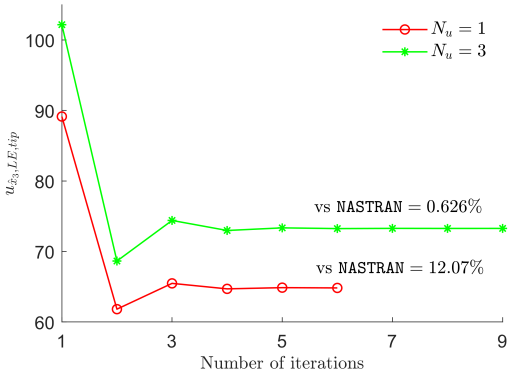

(c) LE tip displacement (mm) for 30 m/s

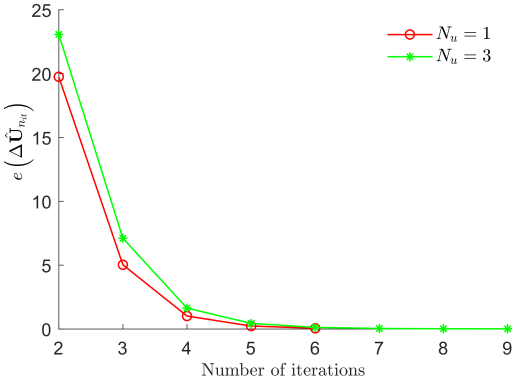

(d) Error for 30 m/s

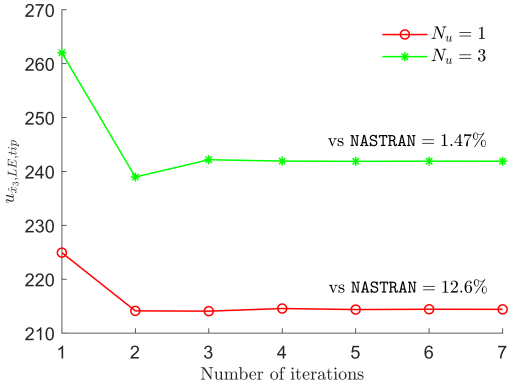

(e) LE tip displacement (mm) for 50 m/s

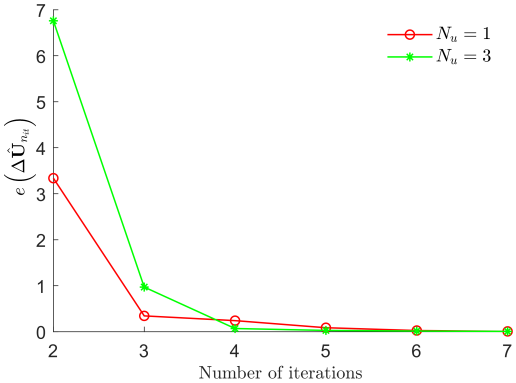

(f) Error for 50 m/s

Figure 5.15: Convergence for displacement (mm) and error $e\left(\Delta\hat{\mathbf{U}}_{n_{it}}\right)$ in staggered iterative method (Navier-Stokes equations, $AOA = 1°$) for isotropic rectangular wing; percentage comparisons against NASTRAN results from Ref.[27] are presented.

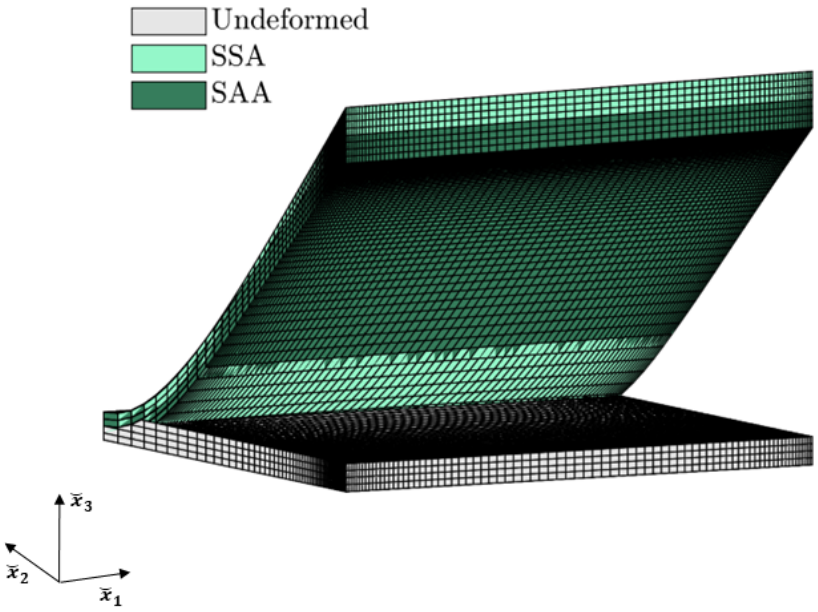

Figure 5.16: Rectangular wing. Deformed configurations at different staggered steps: the difference between SSA and SAA (7th step) is highlighted with respect to the undeformed configuration. The displacements and the axes proportions are altered for visualization purposes, but it is observed that the difference of maximum displacement between SSA and SAA is of the order of the plate thickness. Data: $b = 5\,\mathrm{m}$, $c = 1\,\mathrm{m}$, $U_\infty = 50\,\mathrm{m/s}$, $N_u = 3$.

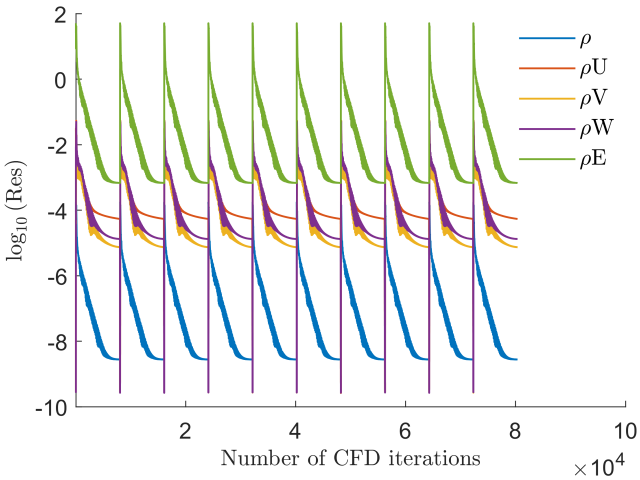

Figure 5.17: Residuals for the test case $U_\infty = 10\,\mathrm{m/s}$, $N_u = 3$: ρ is the residual on the mass equation; ρU, ρV and ρW are referred to the three directions momentum equations; ρE indicates the residual on the energy equation.

Model N_u	$V = 10\,\mathrm{m/s}$	$V = 30\,\mathrm{m/s}$	$V = 50\,\mathrm{m/s}$
0 - Beam	7.6272	68.611	190.40
1 - Beam	7.6275	68.622	190.48
2 - Beam	7.0244	68.236	190.48
3 - Beam	7.4966	73.241	224.45
4 - Beam	7.5126	73.797	243.94
NASTRAN	7.5446	73.731	245.49
1 - Plate	5.1555	64.828	214.44
3 - Plate	5.8113	73.268	241.90

Table 5.4: Rectangular wing. Vertical displacements (SAA) at the tip section LE [mm] with $AOA = 1°$. The figure 0 stands for the Euler-Bernoulli beam model; the other figures indicate the used order of expansion N_u; the beam model reference values are taken from Ref.[27], while the plate solutions (in bold character) are those provided by the present framework.

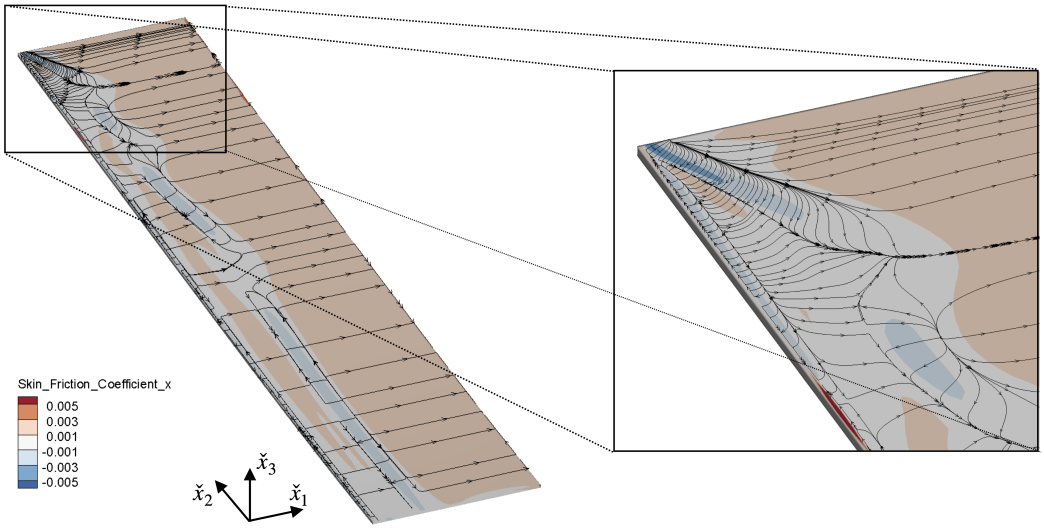

Figure 5.18: Rectangular wing, SSA response, $U_\infty = 50\,\mathrm{m/s}$, $AOA = 1°$. Skin friction coefficient distribution and streamlines on the wing surface including a detail from the tip section, showing relevant non-linear phenomena near leading edge.

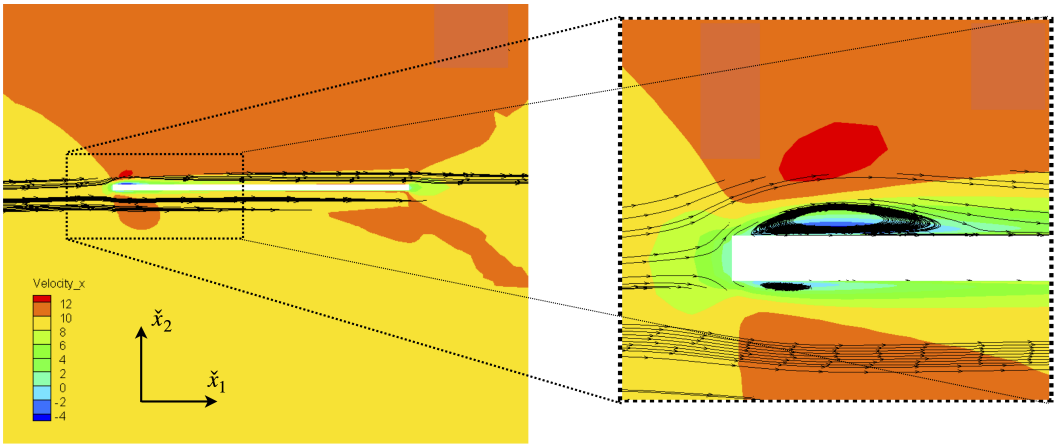

Figure 5.19: Velocity streamlines for $U_\infty = 10\,\mathrm{m/s}$ at $\frac{\check{x}_2}{b} = 0.5$, for the SSA response: although the flow remains attached over most of the upper surface, at low velocities a separation region is established. Such behaviours are not captured by potential-based aerodynamic formulations.

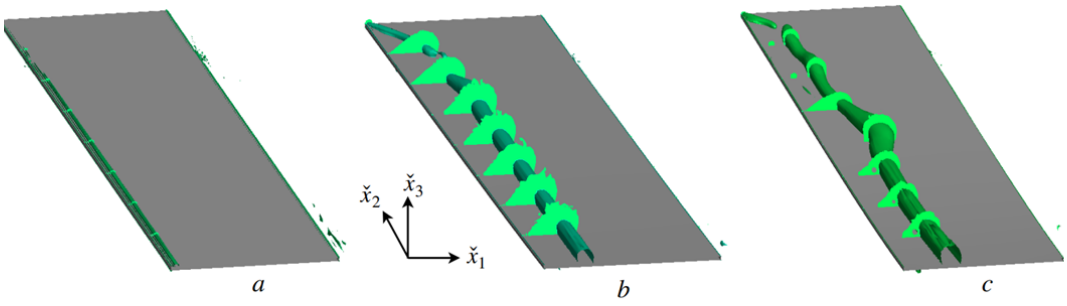

Figure 5.20: Rectangular wing, iso-surfaces for a pressure value for three different speeds at SAA deformed balance configuration. a) $U_\infty = 10\,\mathrm{m/s}$, $p = 101\,294\,\mathrm{Pa}$ b) $U_\infty = 30\,\mathrm{m/s}$, $p = 100\,997\,\mathrm{Pa}$ c) $U_\infty = 50\,\mathrm{m/s}$, $p = 100\,553\,\mathrm{Pa}$.

wind devices [153], for which the developed framework, suitably extended, could provide a valuable virtual testing tool.

5.3.2 Aeroelastic analysis of an isotropic subsonic straight wing

An unswept, untapered and isotropic wing with a NACA 2415 airfoil section is analysed in this Section. The wing has the same planform as that of the rectangular wing previously examined, i.e. wingspan $b = 5\,\mathrm{m}$ and chord $c = 1\,\mathrm{m}$, and its transverse section has the same dimensions as those given in Fig.5.5, although in the first application it is studied as isotropic and not laminated. The same configuration has also been analysed in Ref.[27], which is used as benchmark. The wing is subject to a freestream velocity with $V_\infty = 50\,\mathrm{m/s}$ with an absolute angle of attack $AOA_a = 3°$, corresponding to a geometric angle of attack $AOA_g = 0.98°$ (CFD zero-lift angle $AOA_{ZL} = -2.02°$). The CFD analysis is performed adopting SA turbulence model. The fluid-structure coupling strategies are the same as those previously discussed.

VLM is employed in the benchmark, while with the presented framework RANS-SA equations are used within a control volume discretized in 1859818 3D elements; the results are mapped in Fig. 5.21, where (a) the iterative trends for the maximum displacement (tip trailing edge, due to the combination of bending and twist) and (b) the error $e\left(\Delta\hat{\mathbf{U}}_{n_{it}}\right)$ over the entire displacement field are shown for $N_u = 1$ and $N_u = 3$. Fig. 5.22 presents the CFD residuals trends with the entire staggered process for the $N_u = 3$ case.

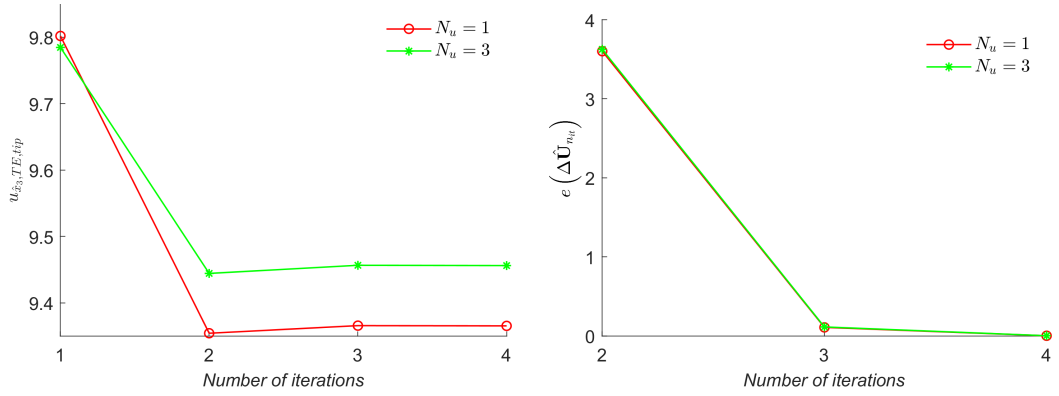

Figure 5.21: Subsonic NACA2415 wing. Convergence for maximum displacement [mm] and error in staggered iterative method ($U_\infty = 50\,\mathrm{m/s}$, $N_u = 1, 3$, $AOA = AOA_g = 0.98°$).

The presence of the airfoil and the preventing of the flow separation allows to the partitioned aeroelastic process to end earlier than what happened with the rect-

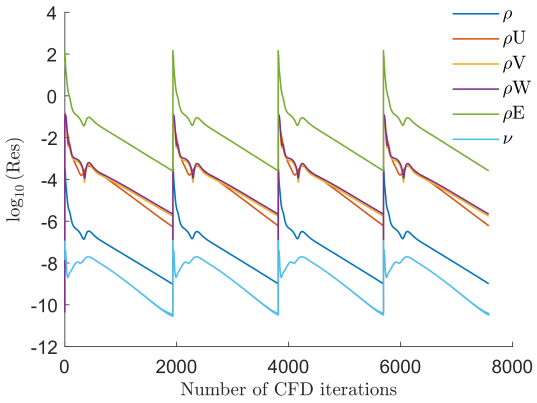

Figure 5.22: Residuals for the wing NACA 2415 test case $V_\infty = 50\,\mathrm{m/s}$ $N_u = 3$; ρ is the residual on the mass equation; ρU, ρV and ρW are referred to the three directions momentum equations; ρE indicates the residual on the energy equation; ν indicates the residual on the viscosity term.

angular wing in Section 5.3.1. Even though the increase of N_u leads to a more accurate value of maximum vertical displacement ($9.46\,\mathrm{mm}$), the resulting error with respect to the literature result ($8.84\,\mathrm{mm}$) is 7%: this is mainly due to the above-mentioned difference between CFD value for AOA_{ZL} and VLM value for AOA_{ZL}. The three-dimensional mechanics of the flow recovered by CFD present framework is observable in Fig. 5.23, where (a) higher and lower pressure regions are underlined by iso-pressure-coefficient (C_p) surfaces and (b) the linearity of the flow is demonstrated by the distribution of the $\check{x}_1$-velocity streamlines. About 280 node CPU hours were needed for computing a converged solution.

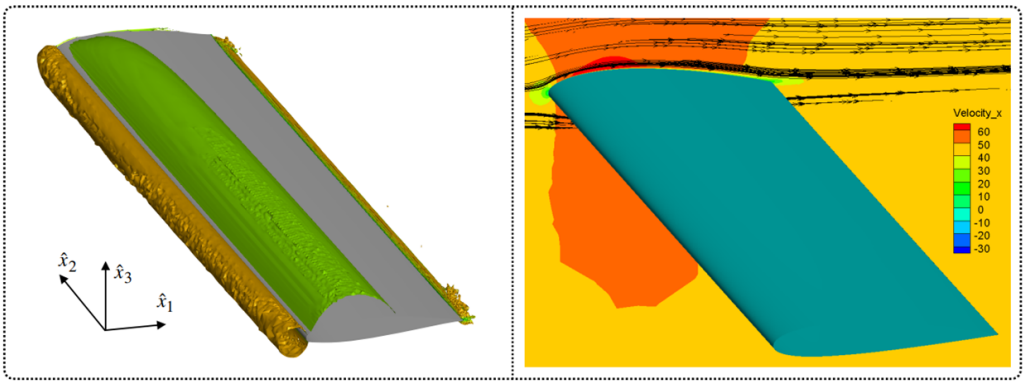

Figure 5.23: Rectangular wing with NACA 2415 airfoil, $b = 5\,\mathrm{m}$, $c = 1\,\mathrm{m}$, $V_\infty = 50\,\mathrm{m/s}$, $N_u = 3$, $AOA = 0.98°$: (*a*) Isosurfaces for pressure coefficient values $C_p = 0.19$ and $C_p = -0.38$ in the SAA CFD simulation; (*b*) Visualization of $\check{x}_1$-velocity streamlines for the SAA CFD simulation.

5.3.3 Aeroelastic analysis of the transonic AGARD 445.6 wing

High-fidelity aerodynamics allow to perform an aeroelastic analysis of a transonic wing within the same framework that has been presented earlier: the behavior of the fluid, even when characterised by the presence of shock waves and regions at Mach > 1, are easily translated by `SU2` in pressure values that, through matrix $\mathbf{H}$, can be applied on the structure in any case. This is the fundamental advantage of an heterogeneous framework.

A root-clamped AGARD 445.6 transonic wing (see Fig.5.24, material properties in Table 5.5) is subject to a $M_\infty = 0.8$ freestream. The details of the configuration are in Ref.[154], which is also the benchmark as it can be seen from Table 5.6: taper ratio $\lambda = 0.658$, quarter-chord sweep angle $\Lambda_{c/4} = 45°$ and NACA65A004 airfoil. The dynamic pressure $q_d = 2867\,\mathrm{Pa}$, the angle-of-attack $AOA = 1°$, CFL$= 10$. Euler governing equations are employed for the inviscid flow; JST scheme is used to manage the convective fluxes through the edges of the 1391975 3D elements collected in the FVM discretization of the O-type control volume; $y^+ = 0.75$ and $d_f = 100\,\mathrm{m}$. The surface CFD mesh is presented as well in Fig.5.24.

Property	**Value**
E_1	$3.15\,\mathrm{GPa}$
E_2, E_3	$0.42\,\mathrm{GPa}$
G_{23}, G_{31}, G_{12}	$0.44\,\mathrm{GPa}$
ν_{23}, ν_{31}, ν_{12}	0.31

Table 5.5: Material properties for carbon fibre composite from Ref.[146].

Model	$\bar{u}_{\hat{x}_3}$ (mm)	$\Delta\bar{\varepsilon}(°)$
Crovato (2020)	11.3	-0.2
Thomas (2017)	12.35	-0.2337
Goura (2001)	11.95	-0.2337
Melville (1997)	11.7	-0.1558
Present	11.1	-0.2339

Table 5.6: Comparison with literature of main static aeroelastic analysis parameters.

Table 5.6 shows a comparison between previous results coming from literature (Refs.[155]-[156]-[157]) and the results from the present framework. The difference in terms of $\bar{u}_{\hat{x}_3}$ is due to the different 3D mesh; however, it is more than acceptable if seen along with the $\Delta\bar{\varepsilon}$ result. The positive out–of–plane bending is

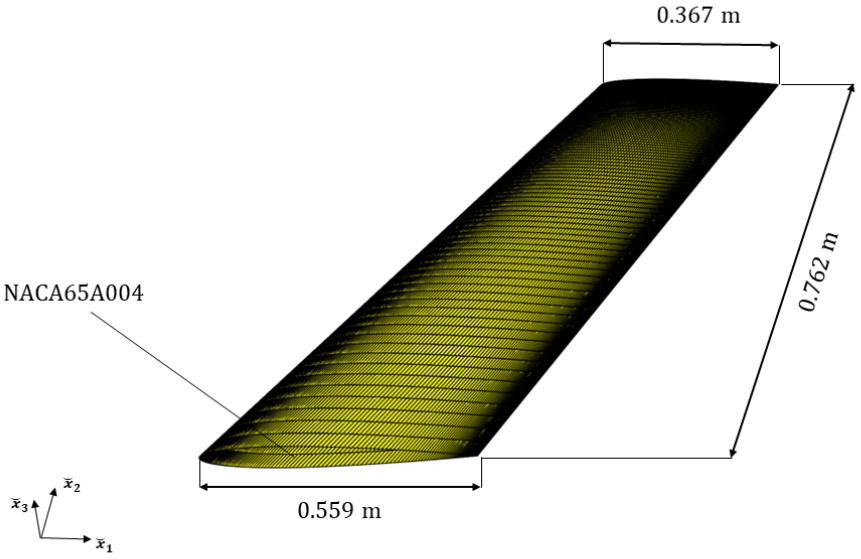

Figure 5.24: AGARD planform dimension with CFD undeformed boundary walls mesh.

coupled with a nose–down torsion at the wing tip. This is not unexpected because the swept–backward wing tends to relieve itself of load in the outboard regions. The convergence history and the final, static aeroelastic response reveals no dependence on the CUF expansion order (see Figs.5.26-5.27). The reason is attributed to the wing configuration, being it very thin for the transonic regime.

However, the number of iterations (higher than the one for the subsonic wing in Section 5.3.2) proves the non-linear behavior of the flow: the macroscopic difference between undeformed configuration and deformed configuration is shown in Fig.5.25.

The transonic nature of the flow is confirmed by the little Mach > 1 region shown in Fig.5.28. It is worth observing that the scheme is also applicable to cases with more developed sonic regions; the present test case has been selected as benchmark results were available in the open literature.

As stated in Chapter 1, the monitoring of drag evolution between undeformed and deformed wing configurations is useful to update the position of the aircraft within the flight envelope. Fig.5.25 figure shows the difference between the undeformed and deformed configurations. The effect of the aeroelastic deformation on loading is to reduce the lift coefficient, from 0.0644 for the rigid wing to 0.0566 for the flexible wing, with a consequent reduction in drag coefficient, from 619 for the rigid to 467 for the flexible wing.

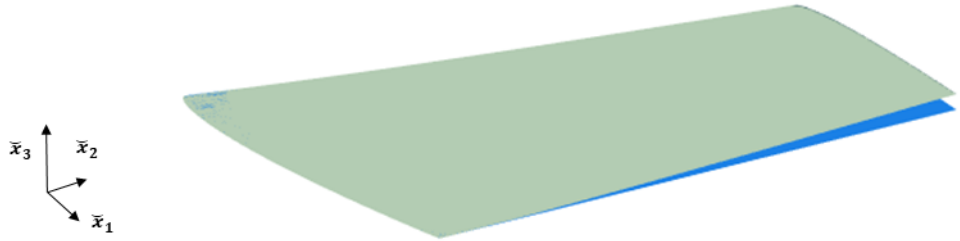

Figure 5.25: Comparison between undeformed and balanced deformed configuration for the AGARD445.6 wing.

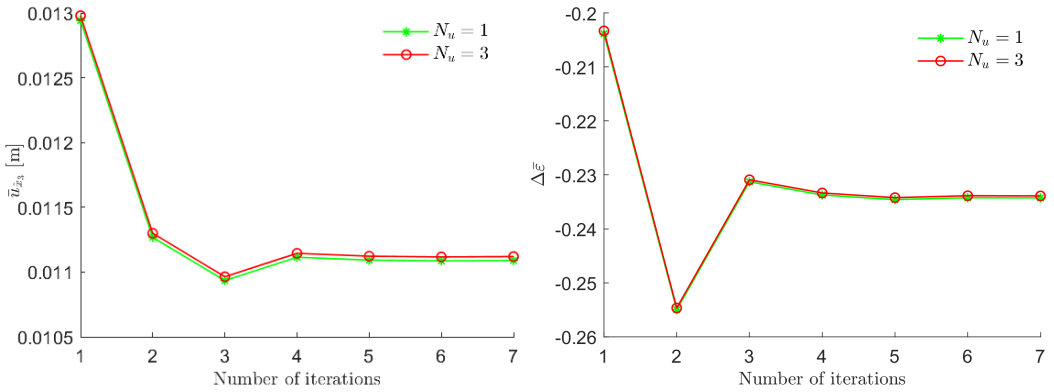

(a) Δz **(b)** $\Delta\varepsilon$

Figure 5.26: Transonic AGARD 445.6 wing. Convergence for mean tip displacement (Δz [m]) and tip twist ($\Delta\varepsilon$ [°]) in staggered iterative method ($M_\infty = 0.8$, $AOA = 1°$). A comparison between $N_u = 1$ and $N_u = 3$ is provided.

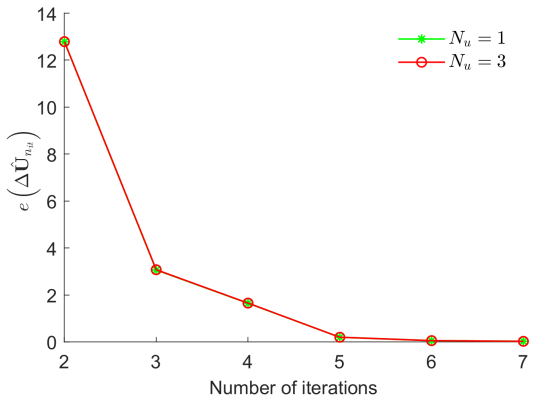

Figure 5.27: Transonic AGARD 445.6 wing. Error in staggered iterative method with $N_u = 1, 3$, with reference to the process described in Fig. 5.26 ($M_\infty = 0.8$, $AOA = 1°$).

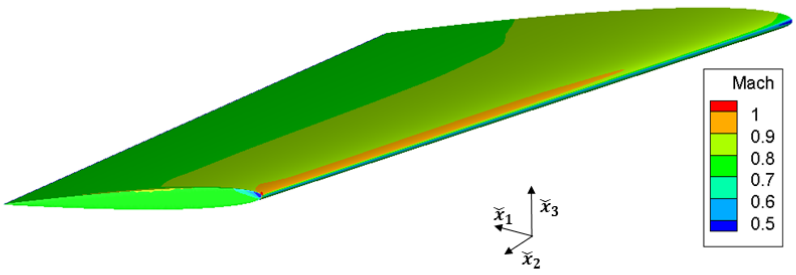

Figure 5.28: Mach contours over AGARD 445.6 wing. The sonic region is located at the leading edge of the tip section. This figure is in perfect agreement with the same Mach contour of Fig.7 of Ref.[154].

5.4 Preliminary aeroelastic tailoring

Aeroelastic tailoring provides the optimized configuration for an aerodynamic component according to a certain parameter. In this Thesis two parametric tailoring analysis are elaborated, both in a subsonic and in a transonic regime, considering only the change of the fiber orientation and thus deriving the variation of the main aeroelastic parameters, $\bar{u}_{\hat{x}_3}$ and $\Delta\bar{\varepsilon}$. The code is not suited for the automatization of this process; nevertheless, considering some desirable improvement in the framework as expressed in Chapter 6, this could represent a future development.

5.4.1 Subsonic preliminary aeroelastic tailoring of a straight composite wing

The effect of the fibers orientation on the aeroelastic response of the NACA 2415 wing is analysed. The wing geometry is identical to that used in Subsection 5.3.2. The skin and spars consist of a single composite layer. For each analysis, the fiber orientation is varied. The properties of the composite material are reported in Table 5.7. This is the same material employed in Ref.[27] to elaborate its parametric study of a composite rectangular wing over the variation of fiber direction.

The fiber orientation is defined with respect to the freestream direction. For example, a $\pm 90°$ orientation identifies fibers directed along the wingspan, see Fig.5.29. To note that the fiber orientation is defined, independently, for the upper and lower wing surfaces. Hence, the wing skin is not obtained by wrapping a single compos-

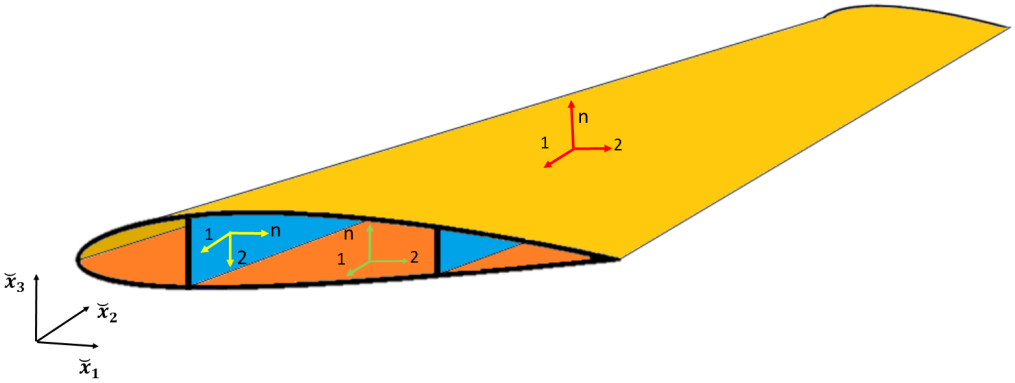

Figure 5.29: Structural layout for the composite wing used in the prototype aeroelastic tailoring. The reference systems for the definition of the fiber orientation in the composite shells are shown: the red triad is referred to the upside of the wing; the green triad is referred to the downside of the wing; the yellow triad is referred to spars surfaces. The angle ϑ is obtained between direction 1 of the triads and $\check{x}_1$. The orientation shown in the figure corresponds to fibers oriented of $-90°$.

ite sheet, but by two sheets with the same fiber orientation. In this manner, a $45°$ orientation in the geometry from Fig.5.29 describes fibers that run from the leading edge to the trailing edge, towards the wing tip. On the contrary, if the skin were obtained by folding a single composite sheet, the upper surface would have fibers at $45°$, and the lower surface fibers at $-45°$. The fiber orientation over the spars is described considering them as an upper surface region with the normal directed along the freestream direction.

Property	**Value**
E_1	$20.5\,\mathrm{GPa}$
E_2, E_3	$10\,\mathrm{GPa}$
G_{23}, G_{31}, G_{12}	$5\,\mathrm{GPa}$
ν_{23}, ν_{31}, ν_{12}	0.25

Table 5.7: Material properties for the single-layer composite material as from Ref.[27].

Results for the maximum vertical displacement at the tip wing section and tip section twist are computed. In Fig.5.30, results are plotted against the fibers orientation angle, and in Fig.5.31 against the freestream velocity. The description adopted for the fiber orientation explains the π-periodic distribution of the results observed in Fig.5.30. It is worth noting that the 3D CFD mesh employed for the flow solution under varying freestream conditions is adapted according to the velocity in

Fig.5.31.

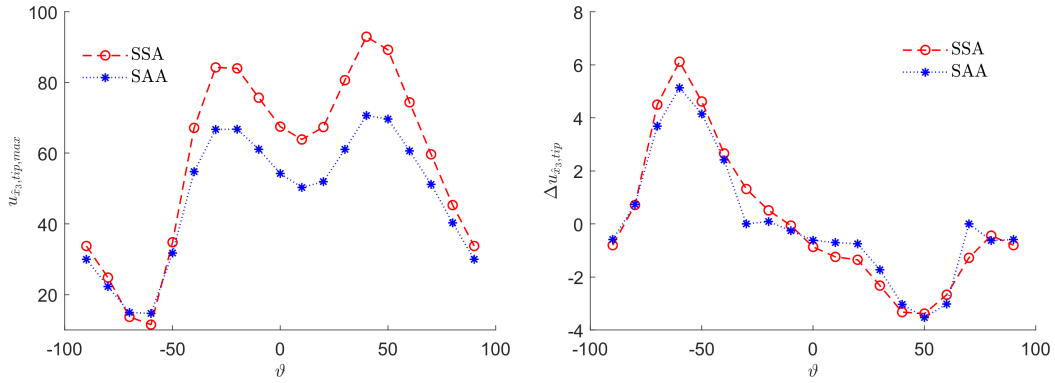

Figure 5.30: Dependence of vertical tip displacement ($u_{\hat{x}_3,tip,max}$, [mm]) (left) and tip section twist ($\Delta u_{\hat{x}_3,tip}$, [mm]) (right) for the NACA 2415 wing on the angle ply orientation [°]; $V_\infty = 50\,\mathrm{m/s}$, $N_u = 3$, $AOA = 0.98°$, RANS SA equations.

The aeroelastic tailoring analysis indicates that a trade-off exists between the configuration that minimises the tip displacement, $-40°$, and that minimising the wing twist, $-10°$, if the twist magnitude is considered. Without solving an optimization problem, the study investigates the impact that the fiber orientation has on the aeroelastic response. The range of the fiber orientation was explored by running several analyses at uniformly distributed values. It is found that the wing twist is one order of magnitude lower than the displacement. This motivated our selection of the $\pm 90°$ fiber orientation for the analysis reported in Fig.5.31, where the differences between SSA and SAA solutions for increasing values of freestream velocity are shown.

The proposed CFD-based method does not allow a direct calculation of the divergence velocity, which is a drawback; however, this is counterbalanced by the possibility of assessing higher velocity regimes, as shown in Fig.5.31, where the wing response is shown for Mach numbers in the range $M_\infty = 0.03$ to $M_\infty = 0.67$. The developed tool can be used also to investigate the transonic regime.

5.4.2 Transonic preliminary aeroelastic tailoring of a swept composite wing

The same single layer material as in Table 5.7 is used for a transonic prototype tailoring of a swept composite ribbed wing. In fact, the wing here considered shares with AGARD 445.6 from Section 5.3.3 the planform, but it presents a NACA2415 airfoil, two spars (located at a quarter and at a three quarter of the chord, with respective thicknesses $0.1h$ and $0.07h$ being h the maximum thickness of the airfoil)

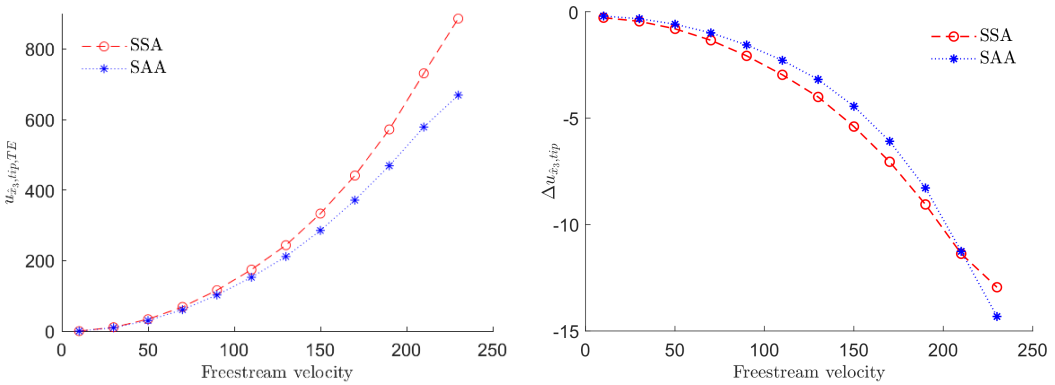

Figure 5.31: Vertical tip displacement (mm) and tip section twist (mm) for the NACA 2415 wing vs. the freestream velocity $(\mathrm{m/s})$. $\pm 90°$ single ply angle. a) $u_{\hat{x}_3,tip,max}$; b) $\Delta u_{\hat{x}_3,tip}$ ($N_u = 3$, $AOA = 0.98°$, RANS SA equations).

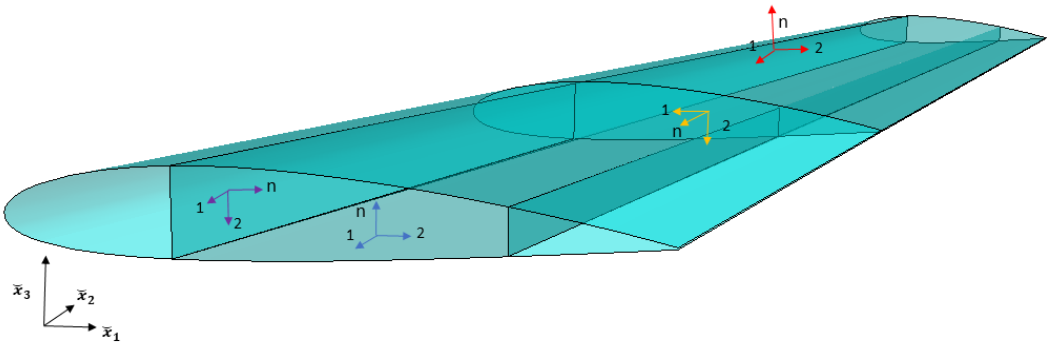

Figure 5.32: Structural layout for the composite wing used in the prototype aeroelastic tailoring. The reference systems for the definition of the fiber orientation in the composite shells are shown: the red triad is referred to the upside of the wing; the blue triad is referred to the downside of the wing; the violet triad is referred to spars surfaces; the yellow triad is referred to the mid-span rib surface. The angle ϑ is obtained between direction 1 of the triads and $\breve{x}_1$. The orientation shown in the figure corresponds to fibers oriented of $-90°$.

and a rib (at the mid-wing-span and thick $0.07h$). See Fig.5.32 as a reference for the fiber orientation.

Considering $AOA = 1°$, $M_\infty = 0.8$, CFL $= 10$, CFD convergence tolerance 10^{-4} and partitioned aeroelastic coupling tolerance set to 10^{-5}, a comparison between $N_u = 1$ and $N_u = 3$ over aeroelastic parameters $\bar{u}_{\hat{x}_3}$ and $\Delta\bar{\varepsilon}$ is performed in Fig. 5.33. The visualization of the difference between SSA and SAA responses is registered as well.

An optimisation trade-off between the two results would be a fiber angle value between $40°$ and $60°$. The most interesting information coming from these results is that the need to increase the CUF order N_u changes according to the fiber ori-

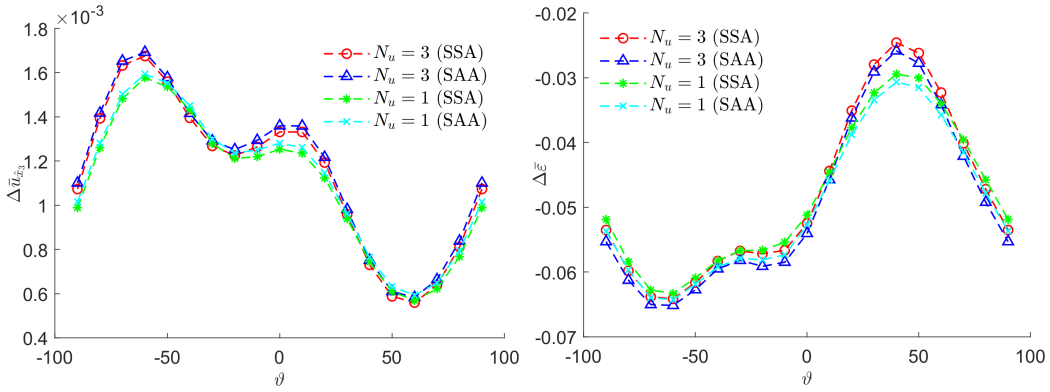

(a) $\Delta\bar{u}_{\hat{x}_3}$ **(b)** $\Delta\bar{\varepsilon}$

Figure 5.33: Static aeroelastic tailoring: mean tip displacement ($\Delta\bar{u}_{\hat{x}_3}$ [m]) and twist ($\Delta\bar{\varepsilon}$) for the wing with AGARD 445.6 planform and NACA2415 airfoil (with $N_u = 3$ and $N_u = 1$) vs. the angle ply orientation [°] ($V_\infty = 243.79\,\mathrm{m/s}$ ($M_\infty = 0.8$), material from Tab. 5.7 (single lamina), $AOA = 1°$, Euler Equations.

entation, making it impossible to foresee with security if an higher or lower order structural analysis is required. Note the relief effect of the negative sweep angle generating less lift for a given angle of attack and causing an inboard shift of the lateral centre of pressure.

Chapter 6

Conclusions and Further Developments

In this Thesis a computational framework combining CUF, FEM, EPM and CFD for general aeroelastic analysis has been developed, implemented, tested and validated against available literature data. Both subsonic and transonic conditions have been considered.

The main benefits/novelties of the presented method are:

1. Its ability to handle structural, geometric and materials complexities (spars, ribs, wing internal elements, combination of different materials) through the flexibility of CUF combined with EPM and FEM; in particular, thanks to the adoption of CUF plate modelling, it is possible to perform exact integration along the thickness of the structure with appreciable generality;

2. The straightforward consideration of more complex non-linear aerodynamic regimes (by changing the configuration inputs and without modifying the general scheme as presented in Fig.4.1), made possible by the modular implementation of the scheme, which delegates the solution of the fluid field to the open-source software suite `SU2`;

3. Its general flexibility with respect to different fluid-structure coupling configurations, as discussed in Chapter 5 and thanks to the heterogeneous interface approach provided by Moving Least Squares patch technique (see Section 4.1). This is due to the possibility of translating any kind of aerodynamic loading condition in a set of pressure values over the structural grid (and thus, into a force vector field for subsequent structural FEM analysis).

The framework presented in this Thesis is promising in terms of future developments:

1. The extension to dynamic and transient regimes, which requires the introduction of mass matrix computation and inertial effects, to analyse dynamic phenomena like flutter or *buffeting* [158]; this could represent a natural evolution from the staggered formulation proposed in this Thesis, considering that in literature dynamic staggered aeroelastic approaches have been shown as suitable for a certain set of problems, see e.g. Ref.[31];

2. The consideration of computational improvements such as Reduced Order Modelling (ROM), see e.g. Ref.[59], aimed at decreasing the burden originating from the need of time integration;

3. The consideration of large strains and displacements in highly flexible aircraft, with the consideration of non-linear structural updates of the structural stiffness matrix $\mathbf{K}$;

4. The consideration of more complex configurations, e.g. including dihedral angle, non-conventional airfoils, or truss-braced wings as those appearing in the SUGAR Volt design of Boeing [159], as well as high-lifting devices and moving parts that could be added considering EPM requirement to project any 3D geometric configuration on a 2D reference plane;

5. The extension to adjoint sensitive analysis [102], overcoming the relevant mathematical issues coming from the calculation of the mutual derivatives of the involved variables and introducing the chance of a compact formulation and a strongly-coupled aeroelastic analysis; this would also increase the rapidity of the parametric tailoring cases shown in Sections 5.4.1-5.4.2

Most of the proposed future developments allow to overcome the principal limitations of the presented framework, such as:

- The high CPU-time required for aeroelastic convergence (increasing with the increase of the difference between SSA and SAA responses), even though part of the computational burden is relieved by parallel computing in the tests from Chapter 5;

- The absence of a compact formulation for the aeroelastic problem, whose presence would allow the computation of critical conditions, e.g. divergence, from the solution of a straightforward eigenvalue problem. Even though a trial-and-error staggered analysis can be performed to detect the occurence of divergence as a lack of convergence in the iterative procedure, such an

approach is not advisable or reliable as critically linked to uncertainties in the definition of the convergence criterion.

Acknowledgements

The Authors acknowledge the support of IRIDIS HPC computational aid from University of Southampton, Uk.

A special thank to professor Andrea Da Ronch for the activity of supervision during the period abroad at the University of Southampton from January to June 2022.

Bibliography

[1] J. Čečrdle. *Whirl Flutter of Turboprop Aircraft Structures*. Ed. by Jiří Čečrdle. Oxford: Woodhead Publishing, 2015. ISBN: 978-1-78242-185-6. DOI: 10.1533/9781782421863.1.

[2] Organisation du traité de l'Atlantique nord, R. Mazet, T. von Karman, F.R. Thurston, Advisory group for aerospace research, and development NATO. *Manual on Aeroelasticity*. v. 3. Harford House, 1968.

[3] D.H. Hodges and G.A. Pierce. *Introduction to Structural Dynamics and Aeroelasticity*. 2nd ed. 32 Avenue of the Americas, New York NY 10013-2473, USA: Springer, 2002. ISBN: 9781107617094.

[4] E.H. Dowell. *A Modern Course in Aeroelasticity - Fifth Edition*. Springer, 2015. ISBN: 9783319094526.

[5] W.P. Rodden, E.F. Farkas, H.A. Malcom, and A.M. Kliszewski. *Aerodynamic Influence Coefficients from Supersonic Strip Theory: Analytical Development and Computational Procedure*. Technical documentary report. Space Systems Division, Air Force Systems Command, United States Air Force, 1962.

[6] D-K. Kim, J-S. Lee, J-Y. Lee, and J-H. Han. An aeroelastic analysis of a flexible flapping wing using modified strip theory - art. no. 69281O. *Proceedings of SPIE - The International Society for Optical Engineering* (2008). DOI: 10.1117/12.776137.

[7] J-W. Lee, J-S. Lee, J-H. Han, and H-K. Shin. Aeroelastic analysis of wind turbine blades based on modified strip theory. *Journal of Wind Engineering and Industrial Aerodynamics* 110 (2012), pp. 62–69. ISSN: 0167-6105. DOI: 10.1016/j.jweia.2012.07.007.

[8] W. Ritz. Uber eine neue methode zur losung gewisser variationsprobleme der mathematischen physik. *Journal fur die reine und angewandte Mathematik* 135 (1909), pp. 1–61.

[9] L. Demasi and E. Livne. Structural Ritz-Based Simple-Polynomial Nonlinear Equivalent Plate Approach: An Assessment. *Journal of Aircraft* 43.6 (2005), pp. 1685–1697. DOI: 10.2514/1.17466.

[10] M. Lesoinne and V. Kaila. Meshless Aeroelastic Simulations of Aircraft with Large Control Surface Deflections. *43rd AIAA Aerospace Sciences Meeting and Exhibit*. 2005. DOI: 10.2514/6.2005-1089.

[11] A. Varello, A. Lamberti, and E. Carrera. Static Aeroelastic Response of Wing-Structures Accounting for In-Plane Cross-Section Deformation. *International Journal of Aeronautical and Space Science* 14.4 (2013), pp. 310–323. DOI: 10.5139/IJASS.2013.14.4.310.

[12] M. Petrolo. Flutter analysis of composite lifting surfaces by the 1D Carrera Unified Formulation and the doublet lattice method. *Composite Structures* 95 (2013), pp. 539–546. DOI: 10.1016/j.compstruct.2012.06.021.

[13] M. Mokhtari, M.R. Permoon, and H. Haddadpour. Aeroelastic analysis of sandwich cylinder with fractional viscoelastic core described by Zener model. *Journal of Fluids and Structures* 85 (2019), pp. 1–16. ISSN: 0889-9746. DOI: 10.1016/j.jfluidstructs.2018.11.013.

[14] J. Jasa, S. Chauhan, J. Gray, and J. Martins. How Certain Physical Considerations Impact Aerostructural Wing Optimization. *AIAA Aviation 2019 Forum*. 2019. DOI: 10.2514/6.2019-3242.

[15] D. Schuster, D. Liu, and L. Huttsell. Computational Aeroelasticity: Success, Progress, Challenge. *Journal of Aircraft* 40.5 (2003), pp. 843–856. DOI: 10.2514/2.6875.

[16] J.D. Anderson and J. Wendt. *Computational fluid dynamics*. Vol. 206. Springer, 1995. ISBN: 9780070016859.

[17] H.K. Versteeg and W. Malalasekera. *An Introduction to Computational Fluid Dynamics: The Finite Volume Method*. Pearson Education Limited, 2007. ISBN: 9780131274983.

[18] R.E. Bertels. Development of Advanced Computational Aeroelasticity Tools at NASA Langley Research Center. *NASA Langley Research Center* (2008).

[19] C. Farhat and D. Amsallem. Recent Advances in Reduced-Order Modeling and Application to Nonlinear Computational Aeroelasticity. *46th Aerospace Science Meeting and Exhibit*. 2008. DOI: 10.2514/6.2008-562.

[20] G. Chen, D. Li, Q. Zhou, A. Da Ronch, and Y. Li. Efficient aeroelastic reduced order model with global structural modifications. *Aerospace Science and Technology* 76 (2018), pp. 1–13. ISSN: 1270-9638. DOI: 10.1016/j.ast.2018.01.023.

[21] R.N. Desmarais R. Harder. Interpolation using surface splined. *Journal Aircraft* 9(2) (1972), pp. 189–191. DOI: 10.2514/3.44330.

[22] G. Quaranta, P. Masarati, and P. Mantegazza. A conservative mesh-free approach for fluid-structure interface problems. *Int. Conf. on Computational Methods for Coupled Problems in Science and Engineering Coupled Problems 2005*. 2005.

[23] G. Hou, J. Wang, and A. Layton. Numerical Methods for Fluid-Structure Interaction — A Review. *Communications in Computational Physics* 12.2 (2012), pp. 337–377. DOI: 10.4208/cicp.291210.290411s.

[24] M.J. Smith, D.H. Hodges, and C.E.S. Cesnik. Evaluation of Some Data Transfer Algorithms for Noncontiguous Meshes. *Journal of Aerospace Engineering* 13.2 (2000), pp. 52–58. DOI: 10.1061/(ASCE)0893-1321(2000)13:2(52).

[25] W. Yen Tey, N.A.C. Sidik, Y. Asako, M.W. Muhieldeen, and O. Afshar. Moving Least Square Methods and its Improvement: A Concise Review. *Journal of Applied and Computational Mechanics* 7(2) (2021), pp. 883–889. DOI: 10.22055/jacm.2021.35435.2652.

[26] A. Varello, E. Carrera, and L. Demasi. Vortex Lattice Method Coupled with Advanced One-Dimensional Structural Models. *ASD Journal* 2.2 (2011), pp. 53–78. DOI: 10.3293/asdj.2011.10.

[27] E. Carrera, A. Varello, and L. Demasi. A refined structural model for static aeroelastic response and divergence of metallic and composite wings. *CEAS Aeronaut J* 4.1 (2013). DOI: 10.1007/s13272-013-0063-2.

[28] R. Kamakoti and W. Shyy. Fluid–structure interaction for aeroelastic applications. *Progress in Aerospace Sciences* 40.8 (2004), pp. 535–558. ISSN: 0376-0421. DOI: 10.1016/j.paerosci.2005.01.001.

[29] W. Whitlow Jr and R.M. Bennett. Application of a transonic potential flow code to the static aeroelastic analysis of three-dimensional wings. *23rd Structures, Structural Dynamics, and Materials Conference*. Vol. 2. 1982, pp. 267–276. DOI: 10.2514/6.1982-689.

[30] M. Love, T. De La Garza, E. F. Charlton, D. Egle, and Lockheed Martin Aeronautics Company. Computational Aeroelasticity in High Performance Aicraft Flight Loads. *ICAAS Congress*. 2000.

[31] S.J. Yong, O.Y. Dong, and J.K. Oh. Aeroelastic Analysis of High-Aspect-Ratio Wings Using a Coupled CFD-CSD Method. *Trans. Japan Soc. Aero. Space Sci.* 59 (2016), pp. 123–133. DOI: 10.2322/tjsass.59.123.

[32] A. Bakica, Š. Malenica, and N. Vladimir. Hydro-structure coupling of CFD and FEM - Quasi-static approach. *Ocean Engineering* 217 (2020), pp. 108–118. ISSN: 0029-8018. DOI: 10.1016/j.oceaneng.2020.108118.

[33] N.V. Nayak. Composite Materials in Aerospace Applications. *International Journal of Scientific and Research Publications*. Vol. 4. 2014.

[34] R.M. Jones. *Mechanics of Composite Materials*. 1st ed. Taylor and Francis, 1999. DOI: 978-1560327127.

[35] H. Ahmad, A. Tariq, A. Shahzad, and M.S. Faheem. Methods and composite materials - A Review. *Polymer Composites* (2019), pp. 1–16. DOI: 10.1002/pc.25311.

[36] S. Abrate and M. Di Sciuva. Equivalent single layer theories for composite and sandwich structures: A review. *Composite Structures* 179 (2017), pp. 482–494. ISSN: 0263-8223. DOI: 10.1016/j.compstruct.2017.07.090.

[37] K.M. Liew, Z.Z. Pan, and L.W. Zhang. An overview of layerwise theories for composite laminates and structures: Development, numerical implementation and application. *Composite Structures* 216 (2019), pp. 240–259. ISSN: 0263-8223. DOI: 10.1016/j.compstruct.2019.02.074.

[38] E. Barbero. *Finite Element Analysis of Composite Materials*. CRC Press, 2008. ISBN: 978-0-429-185-250. DOI: 10.1201/b16295.

[39] A. Varello, L. Demasi, E. Carrera, and G. Giunta. An Improved Beam Formulation for Aeroelastic Applications. *Collection of Technical Papers - 51st AIAA/ASCE/AHS/ASC Structures, Structural Dynamics and Materials Conference*. 2010. DOI: 10.2514/6.2010-3032.

[40] R. Vepa. Aeroelastic Analysis of Wing Structures Using Equivalent Plate Models. *AIAA Journal* 46.5 (2008), pp. 1216–1223. DOI: 10.2514/1.34928.

[41] O.C. Zienkiewicz, R.L. Taylor, and J.Z. Zhu. *The Finite Element Method - Its Basis and Fundamentals*. 7th ed. Butterworth-Heinemann, 2013. ISBN: 9781856176330.

[42] R.K. Kapania and Y. Liu. Static and Vibration Analysis of general wing structures using Equivalent Plate Models. *AIAA Journal* 38.7 (2000), pp. 1269–1277. DOI: 10.2514/2.1098.

[43] E. Carrera, M. Cinefra, M. Petrolo, and E. Zappino. *Finite Element Analysis of Structures through Unified Formulation*. Wiley, 2014. ISBN: 978111994-1217.

[44] E. Carrera and E. Zappino. Aeroelastic analysis of pinched panels in supersonic flow changing with altitude. *Journal of Spacecraft and Rockets* 51.1 (2014), pp. 187–199. DOI: 10.2514/1.A32363.

[45] A. Varello, M. Petrolo, and E. Carrera. A refined 1D FE model for the application to aeroelasticity of composite wings. *Proceedings of 4th International Conference on Computational Methods for Coupled Problems in Science and Engineering: Coupled Problems 2011*. International Center for Numerical Methods in Engineering (CIMNE), 2011. ISBN: 978848992-5786.

[46] F. Nicassio, M. Cinefra, G. Scarselli, M. Filippi, A. Pagani, and E. Carrera. Carrera unified formulation (CUF) for the analysis of disbonds in single lap joints (SLJ). *Nondestructive Characterization and Monitoring of Advanced Materials, Aerospace, Civil Infrastructure, and Transportation XVI*. Ed. by H. Felix Wu, Andrew L. Gyekenyesi, Peter J. Shull, and Tzuyang Yu. Vol. 12047. International Society for Optics and Photonics. SPIE, 2022, p. 1204702. DOI: 10.1117/12.2616542.

[47] A. Milazzo. Unified formulation for a family of advanced finite elements for smart multilayered plates. *Mechanics of Advanced Materials and Structures* 23.9 (2016), pp. 971–980. DOI: 10.1080/15376494.2015.1121523.

[48] N. Young-Hoa and S. Sang Joon. Equivalent-Plate Analysis for a Composite Wing with a Control Surface. *Journal of Aircraft* 50.3 (2013), pp. 853–862. DOI: 10.2514/1.C032020.

[49] L. Riccobene and S. Ricci. Coupling equivalent plate and beam models at conceptual design level. *Aircraft engineering and aerospace technology* 87.1 (2015), pp. 2–10. DOI: 10.1108/AEAT-03-2013-0055.

[50] G. Giles. Further generalization of an equivalent plate representation for aircraft structural analysis. *28th Structures, Structural Dynamics and Materials Conference*. Vol. 26. 1. DOI: 10.2514/6.1987-721.

[51] F.H. Gern, D.J. Inman, and R.K. Kapania. Structural and Aeroelastic Modeling of General Planform Wings with Morphing Airfoils. *AIAA Journal* 40.4 (2002), pp. 628–637. DOI: 10.2514/2.1719.

[52] E. Kim, J. Roh, S. Yoo, and I. Lee. Equivalent Plate Modeling of the Wing-Box Structure with Control Surface. *KSAS International Journal* 7.2 (2006), pp. 104–109. DOI: 10.5139/IJASS.2006.7.2.104.

[53] A. Pagani, A. Garcia de Miguel, M. Petrolo, and E. Carrera. Analysis of laminated beams via Unified Formulation and Legendre polynomial expansions. *Composite Structures* 150 (2016), pp. 78–92. DOI: 10.1016/j.compstruct.2016.01.095.

[54] J. Katz and A. Plotkin. *Low-Speed Aerodynamics*. 2nd ed. Cambridge University Press, 2010. ISBN: 9780521665520.

[55] T.D. Economon, F. Palacios, S.R. Copeland, T.W. Lukaczuk, and J.J. Alonso. SU2: An Open-Source Suite for Multiphysics Simulation and Design. *AIAA Journal* 54.3 (2015), pp. 828–846. DOI: 10.2514/1.J053813.

[56] P. Spalart and S. Allmaras. A one-equation turbulence model for aerodynamic flows. *La Récherce Aerospatiale* 1 (1992), pp. 5–21. DOI: 10.2514/6.1992-439.

[57] D. Wilcox. A half century historical review of the k-omega model. *AIAA, Aerospace Sciences Meeting, 29th, Reno, NV*. 1991. DOI: 10.2514/6.1991-615.

[58] B.E. Launder and D.B. Spalding. The numerical computation of turbulent flows. *Computer Methods in Applied Mechanics and Engineering* 3.2 (1974), pp. 269–289. ISSN: 0045-7825. DOI: 10.1016/0045-7825(74)90029-2.

[59] R. Halder, M. Damodaran, and B.C. Khoo. Implementation of a Modal Analysis Platform for Aeroelastic Computation in an Open-Source Solver SU2 and Application in Reduced Order Modelling. *SU2 Conference 2020*. 2020.

[60] H.C. Patel, D.J. Neiferd, J.J. Alonso, J.D. Deaton, J. Akkala, and J.W. Gallman. Aeroelastic Wing Design Sensitivity Analysis with SU2-Nastran Coupling in OpenMDAO. *AIAA SCITECH 2022 Forum*. DOI: 10.2514/6.2022-2241.

[61] A. Koodly Ravishankara, H. Ozdemir, and E. van der Weide. Implementation of a pressure based incompressible flow solver in SU2 for wind turbine applications. *AIAA Scitech 2020 Forum*. DOI: 10.2514/6.2020-0992.

[62] M.H. Shirk, T.J. Hertz, and T.A. Weisshaar. Aeroelastic tailoring - Theory, Practice and Promise. *J. Aircraft* 23.1 (1986), pp. 6–18. DOI: 10.2514/3.45260.

[63] M.T. Bordogna, P. Lancelot, D. Bettebghor, and R. De Breuker. Static and dynamic aeroelastic tailoring with composite blending and manoeuvre load alleviation. *Structural and Multidisciplinary Optimization* 61 (2020), pp. 2193–2216. DOI: 10.1007/s00158-019-02446-w.

[64] M. Grifò, A. Da Ronch, and I. Benedetti. A computational aeroelastic framework based on high-order structural models and high-fidelity aerodynamics. *Aerospace Science and Technology* 132 (2022), p. 108069. ISSN: 1270-9638. DOI: 10.1016/j.ast.2022.108069.

[65] E. Carrera, A. Varello, and L. Demasi. A refined structural model for static aeroelastic response and divergence of metallic and composite wings. *CEAS Aeronautical Journal* 4 (2014), pp. 175–189. DOI: 10.1007/s13272-013-0063-2.

[66] K. Koo and I. Lee. Aeroelastic behavior of a composite plate wing with structural damping. *Computers and Structures* 50.2 (1994), pp. 167–176. DOI: 10.1016/0045-7949(94)90293-3.

[67] M. Filippi and E. Carrera. Aerodynamic and Mechanical Hierarchical Aeroelastic Analysis of Composite Wings. *Mechanics of Advanced Materials and Structures* 23.9 (2015), pp. 1–31. DOI: 10.1080/15376494.2015.1121561.

[68] V. Gulizzi, I. Benedetti, and A. Milazzo. An implicit mesh discontinuous Galerkin formulation for higher-order plate theories. *Mechanics of Advanced Materials and Structures* 27.17 (2020), pp. 1494–1508. DOI: 10.1080/15376494.2018.1516258.

[69] V. Gulizzi, I. Benedetti, and A. Milazzo. A high-resolution layer-wise discontinuous Galerkin formulation for multilayered composite plates. *Composite Structures* 242 (2020), pp. 112–137. ISSN: 0263-8223. DOI: 10.1016/j.compstruct.2020.112137.

[70] I.H. Abbott and A.E. von Doenhoff. *Theory of Wing Sections*. 2nd ed. Dover, 1959. ISBN: 9780486605869.

[71] A. Pope. *Basic Wing and Airfoil Theory*. McGraw-Hill, 1951. ISBN: 978048-6471884.

[72] S.P. Venkateshan and P. Swaminathan. Chapter 9 - Numerical Integration. *Computational Methods in Engineering*. Ed. by S.P. Venkateshan and P. Swaminathan. Boston: Academic Press, 2014, pp. 317–373. ISBN: 978-0-12-416702-5. DOI: 10.1016/B978-0-12-416702-5.50009-0.

[73] M. Petrolo. *Advanced aeroelastic models for the analysis of lifting surfaces made of composite materials - PhD Dissertation*. Politecnico di Torino, 2011.

[74] A. E. H. Love. The Small Free Vibrations and Deformation of a Thin Elastic Shell. *Philosophical Transactions of the Royal Society of London. A* 179 (1888), pp. 491–546. ISSN: 02643820.

[75] R.D. Mindlin. Influence of Rotatory Inertia and Shear on Flexural Motions of Isotropic, Elastic Plates. *ASME J. Appl. Mech.* 38.1 (1951), pp. 31–38. DOI: 10.1115/1.4010217.

[76] S. Timoshenko and S. Woinowsky-Krieger. *Theory of Plates and Shells*. Engineering mechanics series. McGraw-Hill, 1959. ISBN: 9780070858206.

[77] N. D. Phan and J. N. Reddy. Analysis of laminated composite plates using a higher-order shear deformation theory. *International Journal for Numerical Methods in Engineering* 21.12 (1985), pp. 2201–2219. DOI: 10.1002/nme.1620211207.

[78] L. Demasi. XXX6 Mixed plate theories based on the Generalized Unified Formulation. Part I: Governing equations. *Composite Structures* 87.1 (2009), pp. 1–11. ISSN: 0263-8223. DOI: 10.1016/j.compstruct.2008.07.013.

[79] E. Reissner. On a mixed variational theorem and on shear deformable plate theory. *International Journal for Numerical Methods in Engineering* 23.2 (1986), pp. 193–198. DOI: 10.1002/nme.1620230203.

[80] E. Carrera and S. Brischetto. Analysis of thickness locking in classical, refined and mixed multilayered plate theories. *Composite Structures* 82.4 (2008), pp. 549–562. DOI: 10.1016/j.compstruct.2007.02.002 .

[81] G. Li and E. Carrera. On the Mitigation of Shear Locking in Laminated Plates through P-Version Refinement. *Comput. Struct.* 225.C (2019), pp. 106–121. ISSN: 0045-7949. DOI: 10.1016/j.compstruc.2019.106121.

[82] T.J.R. Hughes. *The Finite Element Method: Linear Static and Dynamic Finite Element Analysis*. Dover Civil and Mechanical Engineering. Dover Publications, 2012. ISBN: 9780486135021.

[83] V. Buljak and G. Ranzi. Chapter 6 - Numerical implementation of constitutive models with large deformation. *Constitutive Modeling of Engineering Materials*. Ed. by V. Buljak and G. Ranzi. Academic Press, 2021, pp. 181–237. ISBN: 978-0-12-814696-5. DOI: 10.1016/B978-0-12-814696-5.00011-3.

[84] J.C. Schulz. Finite element hourglassing control. *International Journal for Numerical Methods in Engineering* 21 (1985), pp. 1039–1048.

[85] E. Carrera, M. Cinefra, and P. Nali. MITC technique extended to variable kinematic multilayered plate elements. *Composite Structures* 92.8 (2010), pp. 1888–1895. ISSN: 0263-8223. DOI: 10.1016/j.compstruct.2010.01.009.

[86] M. Cinefra, M. D'Ottavio, O. Polit, and E. Carrera. Assessment of MITC plate elements based on CUF with respect to distorted meshes. *Composite Structures* 238 (2020), p. 111962. ISSN: 0263-8223. DOI: 10.1016/j.compstruct.2020.111962.

[87] T. Von Karman. Nachrichten von der Gesellschaft der Wissenschaften zu Gottingen, Fachgruppe 1 (Mathematik). *Mechanische Ahnlichkeit und Turbulenz* 5 (1930), pp. 58–76.

[88] L. Leifsson, S. Koziel, and A. Bekasiewicz. Fast Low-fidelity Wing Aerodynamics Model for Surrogate-based Shape Optimization. *Procedia Computer Science* 29 (2014). 2014 International Conference on Computational Science, pp. 811–820. ISSN: 1877-0509. DOI: 10.1016/j.procs.2014.05.073.

[89] A. Kafkas and G. Lampeas. Static Aeroelasticity Using High Fidelity Aerodynamics in a Staggered Coupled ROM Scheme. *Aerospace* 7.11 (2020), p. 164. DOI: 10.3390/aerospace7110164.

[90] P. Negi and M. Subhash. Method to control flow separation over wind turbine blade: A CFD study. *Materials Today: Proceedings* 46 (2021). International Conference on Technological Advancements in Materials Science and Manufacturing, pp. 10960–10963. ISSN: 2214-7853. DOI: 10.1016/j.matpr.2021.02.040.

[91] C. Zhang, C. Bounds, L. Foster, and M. Uddin. Turbulence Modeling Effects on the CFD Predictions of Flow over a Detailed Full-Scale Sedan Vehicle. *Fluids* 4.3 (2019), p. 148. DOI: 10.3390/fluids4030148.

[92] J.D. Taylor and D.F. Hunsaker. Low-fidelity method for rapid aerostructural optimisation and design-space exploration of planar wings. *The Aeronautical Journal* 125.1289 (2021), pp. 1209–1230. DOI: 10.1017/aer.2021.14.

[93] H. Lee and D-J. Lee. Numerical investigation of the aerodynamics and wake structures of horizontal axis wind turbines by using nonlinear vortex lattice method. *Renewable Energy* 132.C (2019), pp. 1121–1133. ISSN: 0960-1481. DOI: 10.1016/j.renene.2018.08.087.

[94] C. Valente, C. Wales, D. Jones, A. Gaitonde, J. Cooper, and Y. Lemmens. A Doublet-Lattice Method Correction Approach for High Fidelity Gust Loads Analysis. *58th AIAA/ASCE/AHS/ASC Structures, Structural Dynamics, and Materials Conference*. 2017. DOI: 10.2514/6.2017-0632.

[95] J. Tu, G.H. Yeoh, and C. Liu. *Computational Fluid Dynamics: A Practical Approach*. Elsevier Science, 2018. ISBN: 9780081012444.

[96] C. Y. Wang. Exact Solutions of the Steady-State Navier-Stokes Equations. *Annual Review of Fluid Mechanics* 23.1 (1991), pp. 159–177. DOI: 10.1146/annurev.fl.23.010191.001111.

[97] O. Reynolds. IV. On the dynamical theory of incompressible viscous fluids and the determination of the criterion. *Philosophical Transactions of the Royal Society of London. (A.)* 186 (1895), pp. 123–164. DOI: 10.1098/rsta.1895.0004.

[98] F. R. Menter. Two-equation eddy-viscosity turbulence models for engineering applications. *AIAA Journal* 32.8 (1994), pp. 1598–1605. DOI: 10.2514/3.12149.

[99] B. Haddadi, C. Jordan, and M. Harasek. Cost efficient CFD simulations: Proper selection of domain partitioning strategies. *Computer Physics Communications* 219 (2017), pp. 121–134. ISSN: 0010-4655. DOI: 10.1016/j.cpc.2017.05.014.

[100] G. Gori, M. Zocca, G. Cammi, A. Spinelli, and A. Guardone. Experimental assessment of the open-source SU2 CFD suite for ORC applications. *Energy Procedia* 129 (2017). 4th International Seminar on ORC Power Systems September 13-15th 2017 Politecnico di Milano Bovisa Campus Milano, Italy, pp. 256–263. ISSN: 1876-6102. DOI: 10.1016/j.egypro.2017.09.151.

[101] M. Morelli, T. Bellosta, and A. Guardone. Development and preliminary assessment of the open-source CFD toolkit SU2 for rotorcraft flows. *Journal of Computational and Applied Mathematics* 389 (2021), p. 113340. ISSN: 0377-0427. DOI: 10.1016/j.cam.2020.113340.

[102] I. Ghazlane, G. Carrier, A. Dumont, M. Marcelet, and J-A. Désidéri. Aerostructural optimization with the adjoint method. *EUROGEN 2011*. 2011.

[103] O.D. Kellogg. *Foundations of Potential Theory*. Die Grundlehren der mathematischen Wissenschaften in Einzeldarstellungen. Dover Publications, 1953. ISBN: 9780486601441.

[104] C.K. Batchelor, G.K. Batchelor, and Cambridge University Press. *An Introduction to Fluid Dynamics*. Cambridge Mathematical Library. Cambridge University Press, 1967. ISBN: 9780521663960.

[105] A.M. Kuethe and C.Y. Chow. *Foundations of Aerodynamics: Bases of Aerodynamic Design*. Wiley, 1997. ISBN: 9780471129196.

[106] C. Xie, L. Yi, C. Yang, and J. Cooper. Geometrically Nonlinear Aeroelastic Stability Analysis and Wind Tunnel Test Validation of a Very Flexible Wing. *Shock and Vibration* 2016.3 (2016), pp. 1–17. DOI: 10.1155/2016/5090719.

[107] C. Xie, C. An, L. Yi, and C. Yang. Static aeroelastic analysis including geometric nonlinearities based on reduced order model. *Chinese Journal of Aeronautics* 30.2 (2017), pp. 638–650. DOI: 10.1016/j.cja.2016.12.031.

[108] H. Hesse. "Consistent Aeroelastic Linearisation and Reduced-Order Modelling in the Dynamics of Manoeuvring Flexible Aircraft". PhD thesis. Imperial College London, 2013.

[109] O. Şugar Gabor, A. Koreanschi, and R. M. Botez. A new non-linear vortex lattice method: Applications to wing aerodynamic optimizations. *Chinese Journal of Aeronautics* 29.5 (2016), pp. 1178–1195. ISSN: 1000-9361. DOI: 10.1016/j.cja.2016.08.001.

[110] M. Yahyaoui. Generalized Vortex Lattice Method for Predicting Characteristics of Wings with Flap and Aileron Deflection. *World Academy of Science, Engineering and Technology, International Journal of Mechanical, Aerospace, Industrial, Mechatronic and Manufacturing Engineering* 8.10 (2014), pp. 1690–1698. DOI: 10.5281/zenodo.1096425.

[111] V.T. Nguyen and F. Nestmann†. Applications of CFD in Hydraulics and River Engineering. *International Journal of Computational Fluid Dynamics* 18.2 (2004), pp. 165–174. DOI: 10.1080/10618560310001634186.

[112] F.J. Zajaczkowski, S.E. Haupt, and K.J. Schmehl. A preliminary study of assimilating numerical weather prediction data into computational fluid dynamics models for wind prediction. *Journal of Wind Engineering and Industrial Aerodynamics* 99.4 (2011). The Fifth International Symposium on Computational Wind Engineering, pp. 320–329. ISSN: 0167-6105. DOI: 10.1016/j.jweia.2011.01.023.

[113] T. Kaufmann, R. Graefe, M. Hormes, T. Schmitz-Rode, and U. Steinseifer. Computational fluid dynamics in biomedical engineering. *Computational Fluid Dynamics: Theory, Analysis and Applications* (2013), pp. 109–136.

[114] D.S-K. Ting. *Basics of Engineering Turbulence*. Ed. by David S-K. Ting. Academic Press, 2016. ISBN: 978-0-12-803970-0. DOI: 10.1016/B978-0-12-803970-0.00002-7.

[115] H. Schlichting and J. Kestin. *Boundary-layer Theory*. McGraw-Hill classic textbook reissue series. McGraw-Hill, 1979. ISBN: 9780070553347.

[116] George B. Arfken, David F. Griffing, Donald C. Kelly, and Joseph Priest. *International Edition University Physics*. Ed. by George B. Arfken, David F. Griffing, Donald C. Kelly, and Joseph Priest. Academic Press, 1984. ISBN: 978-0-12-059858-8. DOI: 10.1016/B978-0-12-059858-8.50028-5.

[117] Jean Cousteix. *Encyclopedia of Physical Science and Technology (Third Edition)*. Ed. by R.A. Meyers. Third Edition. New York: Academic Press, 2003. ISBN: 9780122274107. DOI: 10.1016/B0-12-227410-5/00906-6.

[118] A.J. Favre and Aix-Marseille Univ (France) inst de mécanique statistique de la turbulence. *The equations of compressible turbulent gases*. Defense Technical Information Center, 1965.

[119] R. Eymard, T. Gallouët, and R. Herbin. *Solution of Equation in Rn (Part 3), Techniques of Scientific Computing (Part 3)*. Vol. 7. Handbook of Numerical Analysis. Elsevier, 2000. DOI: 10.1016/S1570-8659(00)07005-8.

[120] F. Moukalled, L. Mangani, and M. Darwish. *The Finite Volume Method in Computational Fluid Dynamics: An Advanced Introduction with OpenFOAM and Matlab*. Fluid Mechanics and Its Applications. Springer International Publishing, 2015. ISBN: 9783319168746.

[121] Amir Sharif Ahmadian. *Numerical Models for Submerged Breakwaters*. Ed. by S.A. Amir. Boston: Butterworth-Heinemann, 2016. ISBN: 978-0-12-802413-3. DOI: 10.1016/B978-0-12-802413-3.00006-7.

[122] T. Barth, R. Herbin, and M. Ohlberger. *Finite Volume Methods: Foundation and Analysis*. John Wiley and Sons, Ltd, 2017, pp. 1–60. ISBN: 9781119176817. DOI: 10.1002/9781119176817.ecm2010.

[123] E. Shima and T. Jonouchi et al. Role of CFD in aeronautical engineering. No. 14: AUSM type upwind schemes. 1997. DOI: 10.2322/jjsass.54.10.

[124] T. Han, J.A.C. Humphrey, and B.E. Launder. A comparison of hybrid and quadratic-upstream differencing in high Reynolds number elliptic flows. *Computer Methods in Applied Mechanics and Engineering* 29.1 (1981), pp. 81–95. ISSN: 0045-7825. DOI: 10.1016/0045-7825(81)90016-5.

[125] A. Harten. High resolution schemes for hyperbolic conservation laws. *Journal of Computational Physics* 49.3 (1983), pp. 357–393. ISSN: 0021-9991. DOI: 10.1016/0021-9991(83)90136-5.

[126] T. Economon, F. Palacios, and J. Alonso. A Coupled-Adjoint Method for Aerodynamic and Aeroacoustic Optimization. *12th AIAA Aviation Technology, Integration, and Operations (ATIO) Conference and 14th AIAA/ISSMO Multidisciplinary Analysis and Optimization Conference*. American Institute of Aeronautics and Astronautics, 2012. DOI: 10.2514/6.2012-5598.

[127] F. Palacios, J. Alonso, K. Duraisamy, M. Colonno, J. Hicken, A. Aranake, A. Campos, S. Copeland, T. Economon, A. Lonkar, T. Lukaczyk, and T. Taylor. Stanford University Unstructured (SU2): An open-source integrated computational environment for multi-physics simulation and design. *51st AIAA Aerospace Sciences Meeting including the New Horizons Forum and Aerospace Exposition*. American Institute of Aeronautics and Astronautics, 2013. DOI: 10.2514/6.2013-287.

[128] F. Palacios, T. Economon, A. Aranake, S. Copeland, A. Lonkar, T. Lukaczyk, D. Manosalvas-Kjono, K. Naik, A. Padrón, B. Tracey, A. Variyar, and J. Alonso. Stanford University Unstructured (SU2): Analysis and Design Technology for Turbulent Flows. 2014. DOI: 10.2514/6.2014-0243.

[129] S. Karman and N. Wyman. Automatic Unstructured Mesh Generation with Geometry Attribution. *AIAA Scitech 2019 Forum*. 2019. DOI: 10.2514/6.2019-1721.

[130] F.M. White. *Fluid Mechanics*. McGraw-Hill International Editions. WCB/McGraw-Hill, 1999. ISBN: 9780070697164.

[131] F. Goetten, D.F. Finger, M. Marino, and C. Bil. A review of guidelines and best practices for subsonic aerodynamic simulations using RANS CFD. *Asia Pacific International Symposium on Aerospace Technology*. 2019.

[132] F.M. White. *Viscous Fluid Flow*. McGraw-Hill, New York, pp. 28–29. ISBN: 978-0-071-009-959.

[133] A. Jameson, W. Schmidt, and E. Turkel. Numerical Solution of the Euler Equations by Finite Volume Methods Using Runge-Kutta Time Stepping Schemes. *AIAA Journal* 81 (1981). DOI: 10.2514/6.1981-1259.

[134] P.L. Roe. Approximate Riemann solvers, parameter vectors, and difference schemes. *Journal of Computational Physics* 43.2 (1981), pp. 357–372. ISSN: 0021-9991. DOI: 10.1016/0021-9991(81)90128-5.

[135] Y. Saad and M.H. Schultz. GMRES: a generalized minimal residual algorithm for solving nonsymmetric linear systems. *Siam Journal on Scientific and Statistical Computing* 7.3 (1986), pp. 856–869. DOI: 10.1137/0907058.

[136] C. Farhat, K.G. van der Zee, and P. Geuzaine. Provably second-order time-accurate loosely-coupled solution algorithms for transient nonlinear computational aeroelasticity. *Computer Methods in Applied Mechanics and En-*

gineering 195.17 (2006). Fluid-Structure Interaction, pp. 1973–2001. ISSN: 0045-7825. DOI: 10.1016/j.cma.2004.11.031.

[137] H. Dang, Z. Yang, and Y. Li. Accelerated loosely-coupled CFD/CSD method for nonlinear static aeroelasticity analysis. *Aerospace Science and Technology* 14.4 (2010), pp. 250–258. ISSN: 1270-9638. DOI: 10.1016/j.ast.2010.01.004.

[138] J. Dillinger, M. Abdalla, Y. Meddaikar, and T. Klimmek. Static aeroelastic stiffness optimization of a forward swept composite wing with CFD-corrected aero loads. *CEAS Aeronautical Journal* 10.2 (2019). DOI: 10.1007/s13272-019-00397-y.

[139] E. Livne and I. Navarro. Nonlinear Equivalent Plate Modeling of Wing-Box Structures. *Journal of Aircraft* 36.5 (1999), pp. 851–865. DOI: 10.2514/2.2519.

[140] R. Schaback and H. Wendland. Characterization and construction of radial basis functions. *Multivariate Approximation and Applications*. Ed. by N. Dyn, D. Leviatan, D. Levin, and A. Pinkus. 2000. ISBN: 9780521800235. DOI: 10.1017/CBO9780511569616.002.

[141] R.P. Dwight. Robust Mesh Deformation using the Linear Elasticity Equations. *Computational Fluid Dynamics 2006*. Ed. by Herman Deconinck and E. Dick. Berlin, Heidelberg: Springer Berlin Heidelberg, 2009, pp. 401–406. ISBN: 9783540927792.

[142] P.J. Bickel and K.A. Doksum. *Mathematical Statistics: Basic Ideas and Selected Topics*. Mathematical Statistics: Basic Ideas and Selected Topics v. 1. Prentice Hall, 2001. ISBN: 9780138503635.

[143] M. Grifò, V. Gulizzi, A. Milazzo, A. Da Ronch, and I. Benedetti. High-fidelity aeroelastic transonic analysis using higher-order structural models (Submitted under Review). *Composite Structures* (2023).

[144] D. Liu, V.V. Toropov, D.C. Barton, and O.M. Querin. Weight and mechanical performance optimization of blended composite wing panels using lamination parameters. *Struc Multidisc Optim* 52 (2015), pp. 549–562. DOI: 10.1007/s00158-015-1244-x.

[145] C. Geuzaine and J-F. Remacle. Gmsh: a three-dimensional finite element mesh generator with built-in pre-and post-processing facilities. *International Journal for Numerical Methods in Engineering* 0 (2009), pp. 1–19. DOI: 10.1002/nme.2579.

[146] J. Dillinger, M. Abdalla, T. Klimmek, and Z. Gürdal. Static Aeroelastic Stiffness Optimization and Investigation of Forward Swept Composite Wings. *10th World Congress on Structural and Multidisciplinary Optimization*. 2013. URL: https://elib.dlr.de/84218/.

[147] M.S. Selig. *UIUC airfoil data site*. English (US). Department of Aeronautical and Astronautical Engineering University of Illinois at Urbana-Champaign, 1996. URL: https://m-selig.ae.illinois.edu/ads/coord_database.html.

[148] Z.F. Siddiqi. A computational fluid dynamics investigation of subsonic wing designs for unmanned aerial vehicle application. *Proceedings of the Institution of Mechanical Engineerings Part G Journal of Aerospace Engineering*. 2019. DOI: 10.1177/0954410019852553.

[149] *ANSYS Fluent Theory Guide (Release 15.0)*. ANSYS Inc., 2013.

[150] M. Drela. XFOIL: An Analysis and Design System for Low Reynolds Number Airfoils. *Low Reynolds Number*. Vol. 54. 1989, pp. 1–12. ISBN: 978354-0518846. DOI: 10.1007/978-3-642-84010-4_1.

[151] M.J. Hoffmann, R. Reuss Ramsey, and G.M. Gregorek. Effects of grit roughness and pitch oscillations on the NACA 4415 airfoil. *Golden, CO: National Renewable Energy Laboratory* (1996). DOI: 10.2172/266691.

[152] W. Haase, V. Selmin, and B. Winzell. *Progress in Computational Flow-Structure Interaction: Results of the Project UNSI, supported by the European Union 1998 – 2000*. Notes on Numerical Fluid Mechanics and Multidisciplinary Design. Springer Berlin Heidelberg, 2013. ISBN: 9783540454-892.

[153] Q. Wen, X. He, Z. Lu, R. Streiter, and T. Otto. A comprehensive review of miniatured wind energy harvesters. *Nano Materials Science* 3.2 (2021), pp. 170–185. ISSN: 2589-9651. DOI: 10.1016/j.nanoms.2021.04.001.

[154] A. Crovato. “Steady Transonic Aerodynamic and Aeroelastic Modeling for Preliminary Aircraft Design”. PhD thesis. ULiège - Université de Liège, 2020.

[155] R. Melville, S. Morton, D. Rizzetta, R. Melville, S. Morton, and D. Rizzetta. Implementation of a fully-implicit, aeroelastic Navier-Stokes solver. *13th Computational Fluid Dynamics Conference*. 1997. DOI: 10.2514/6.1997-2039.

[156] G. Goura. “Time marching analysis of flutter using computational fluid dynamics”. PhD thesis. University of Glasgow, 2001.

[157] D. Thomas, A. Variyar, R. Boman, T.D. Economon, J.J. Alonso, G. Dimitriadis, and V.E. Terrapon. Staggered strong coupling between existing fluid and solid solvers through a python interface for fluid-structure interaction problems. *VII International Conference on Computational Methods for Coupled Problems in Science and Engineering - Coupled Problems 2017*. 2017. ISBN: 9788494690921.

[158] J. Stegmüller, L. Katzenmeier, and C. Breitsamter. Horizontal tail buffeting characteristics at wing vortex flow impact. *CEAS Aeronautical Journal* 13 (2022), pp. 1–18. DOI: 10.1007/s13272-022-00593-3.

[159] B.J. Brelje and J.R.R.A. Martins. Electric, hybrid, and turboelectric fixed-wing aircraft: A review of concepts, models, and design approaches. *Progress in Aerospace Sciences* 104 (2019), pp. 1–19. ISSN: 0376-0421. DOI: 10.1016/j.paerosci.2018.06.004.